Yb^{3+}-, Nd^{3+}-, Ho^{3+}-, and Tm^{3+} - doped materials for optoelectronic applications

Andrea Arcangeli
Dipartimento di Fisica
Universitá di Pisa

A thesis submitted for the degree of
PhilosophiæDoctor (PhD), Physics

2013

---

1. Reviewer: Prof. Mauro Tonelli

2. Reviewer: Prof. Alberto Di Lieto

Day of the defense: 03/05/2013

Signature from head of PhD committee:

To my family

Acknowledgements

First of all I want to thank my family that supported me so much during these years. Without their help, patience and support this work wouldn’t be possible.

Many thanks go to all the NMLA group in Pisa of Prof. Mauro Tonelli. It’s difficult to express all my gratitude to Prof. Alberto Di Lieto, Stefano Veronesi, Daniela Parisi, Alessandra Toncelli, Francesco Cornacchia, Stefano Bigotta, Xia Zhitai, Lucia Bonelli for their help and fruitful collaboration during these years of work in Pisa.

It was a great experience to share this time with all of them, and also with Ilaria, Raffaele, Renzo, Elena, Katia and all the others that ’appeared’ in the group, even for a short period.

Then I want to send my deep thanks to the group of prof. Huber in Hamburg, where I had the opportunity to work in a stimulating environment and where I met people that became not just colleagues but real friends.

So I wish to thank dott. Petermann for interesting discussions, Sebastian Heinrich for his patience in telling me everything about the PLD setup, Fabian Reichert and Joerg Siebenmorgen for their kindness and help to show me what could be done in Hamburg also after work (!) and then all the others (way too many to be all mentioned....).

Many thanks also to the group of prof. Agnesi in Pavia for their invaluable collaboration, in particular to dott. Federico Pirzio for the private lectures on mode-locked lasers....

A special thank goes to Francesca Moglia, that seems to be involved in every step of my Physics studies (wherever I go, somehow she’s there).

I can’t thank all the people that I had around during these years and that helped me a lot for everything because they are simply too many, but at least the Ghezzano guys (Matteo, Damiano, Guglielmo and Claire), my

wonderful flatmates in Pisa, really need to be mentioned.
Finally, I also thank my new group at Chimie Paristech for their patience in tolerating my sleepy moods during the days following the nights I spent writing this manuscript.....

Contents

List of Figures

List of Tables

Chapter 1

Introduction

This work has been performed mainly at the Physics Department of Pisa University, in the group of New Materials for Laser Application (prof. Mauro Tonelli) and in part at the Insitut for Laser Physics of Hamburg University, Solid-State Laser group (prof. Guenter Huber).

The oxide crystals studied in Pisa were provided by the group of Xutang Tao at the State Key Laboratory of Crystal Materials of Shandong University in China and their laser properties were investigated at the Department of Electronics of Pavia University by the group of Giancarlo Reali.

1.1 Motivations

Solid state lasers based on rare earth doped materials are a well estabilished research field that led in recent years to important goals, giving an impulse both to basic science and commercial applications.

The importance of an incessant study on the luminescence properties of materials is due to the need of new light sources to cover the electromagnetic spectrum from the near UV to the mid IR; also the need for higher efficiencies in the electrical-to-optical energy conversion is becoming an issue that has to be solved with both novel device architectures and novel materials. Moreover, the development of new techniques based on pulsed laser sources (for example picosecond-laser scalpels in surgery) require the developement of materials with large gain bandwidth and high power capabilities, and

these characteristics have to be combined with low production costs and reliability of the developed devices.
With this aim, a part of my PhD work has been devoted to the investigation of a class of materials, the so-called 'mixed garnets', which present broad gain bandwidths combined with good thermo-mechanical properties. These were studied as possible bulk crystals for the implementation of laser sources in the near infrared region, and their luminescence properties are deeply investigated in order to understand the mechanisms that make them good candidates for many kinds of possible applications.

Another area that is undergoing a deep change in these years is the field of lighting and screen technology, where visible light sources play a fundamental role: from one side, the old light bulbs have been replaced by energy-saving halogen lamps and LED sources, from the other the old CRT screens have been definitely put apart due to the developement of TFT and LED screens, and the advent of laser TV's will change in a few years the whole TV market. Also in this very applicative and commercial area, fundamental research on luminescent materials is pushing towards the establishment of a 'killer techonolgy', and many companies and research groups are working to find the best solutions combining compactness and brightness of the sources, as well as to reduce the costs that are of course a crucial issue for mass production.
Among the materials that might be used for such kinds of applications rare-earth doped fluoride crystals, with their low phononic energies, seem to be able to satisfy many requirements thanks to their low non-radiative losses. In fact, one of the major problems for the realization of solid state emitters in the visible spectral range with rare-earth doped materials is the fast decay of the higher energy levels responsible for the visible transitions. This reduces the possibility to store energy in those levels and so the overall conversion process turns out to be unefficient.
A part of my work is dedicated to the investigation of one of the best known fluoride materials in combination with Holmium doping, in order to determine if this would be a good candidate for such kind of application.

Finally, lasers are not only used for illumination and cutting, of course. The field of optical communications is also undergoing a deep revolution due to the advent of more efficient optical multiplexers and demultiplexers, modulators, amplifiers and so on. Especially in this field the possibility to develop compact devices capable to perform more operations on a single chip is attracting the information technology developers. The possibility to integrate such devices on semiconductor-based substrates is being studied deeply, because this leads to a perfect integration of well known silicon-based and novel technologies. One of the possibilities to obtain this result is to be able to build up multi-layer optically-active structures, where the optical signal is produced, processed, guided and transmitted. There are many techniques which are suitable for this task and one of them, the Pulsed Laser Deposition (PLD), will be investigated in a specific chapter of this thesis.

1.2 Structure of the thesis

One of the main problems during the writing of this thesis has been to organize the amount of material that has been investigated in these years in an organic plot. In fact, this work presents different aspects and involves different techniques, all of them being related to the research on new luminescent materials. So my final decision has been to divide the different topics in self-consistent chapters, giving at first a theoretical introduction (extrapolated from textbooks cited in the Bibliography) as a guideline for the reader, and the description of the experimental setups used for the different experiments.

In this way each chapter can be read indipendently from the others and the final work is organized more or less as a collection of indipendent reviews.

Anyway, three different areas can be distinguished clearly in the overall thesis:

- Chapters 2 and 3 are introductory chapters, where the main aspects of the theory and the experimental setups are presented.
- Chapters from 4 to 8 are all related to the study of different combinations of Garnet materials as possible laser sources in the near infrared. Their spectroscopical properties are deeply investigated and finally the laser experiments are shown because they underline some aspects that were pointed out during the spectroscopic studies.

- Chapter 9 delas with the study of Ho^{3+}- doped YLF, a system that has already been deeply investigated for its potentials in the near infrared, but not yet as visible emitter.
- Chapter 10 presents the results obtained during my working period at ILP laboratories in Hamburg: here the deposition of Tm^{3+}- doped sesquioxides thin films is reported and their spectroscopical characteristics are presented.

Chapter 2

Preliminary theoretical background

In this chapter a brief overview of the main properties of rare-earth ions in crystal lattices is given, including their electronic structures, energy levels and energy transfer processes. The methods used for the determination of absorption and emission cross sections are also described.
For more detailed tractations references on textbooks and articles are indicated in the text (45) (46).

2.1 Rare earth elements

Rare earths are elements with atomical number Z between 58 (Cerium) and 71 (Lutetium), with similar properties, due to their electronic configurations.
The interest for triple ionized ions of these elements comes from their narrow emission and absorption bands, dramaticaly different from what happens for the large bands of the transition metals.
Rare earth - based lasers usually consist of an insulating host with a large bandgap (>5 eV), substitutionally doped with one or more kinds of ions.
A triple ionizes lanthanide has the electronic configuration of Xenon:

$$(1s^2 2s^2 2p^6 3s^2 3p^6 3d^{10} 4s^2 4p^6 4d^{10} 5s^2 5p^6),$$

plus two electrons in the 6s shell and a partially filled 4f shell. An other electron is occasionally found in the 5d state.

The most common ionization state is the triple ionization, even though also double ionized states (especially for Eu, Sm, Yb) and four-times ionized states (Ce, Tb) are quite common.
Triply ionized states occur when the 6s electrons and one from the 5d or 4f shells form bonds with the neighboring atoms of the crystalline host (tipically oxigen or fluorine). The other 4f electrons are the shielded from the crystal field by the filled 5s and 5p shells, having a larger spatial extention and spherical symmetry, and this shielding can be considered as their only effect. According to this picture, the energy levels of the ions are calculated taking into account only the interactions among the electrons in the 4f shell.

2.2 Rare earth energy levels

In order to calculate the energy levels of rare earth ions, starting from the free-ion case one should solve the Hamiltonian that can be written as follows:

$$H = T + V_{en} + V_{ee} + V_{so} = -\frac{\hbar^2}{2m}\sum_{i=1}^{N}\nabla_i^2 - \sum_{i=1}^{N}\frac{Ze^2}{r_i} + \sum_{i<j}^{N}\frac{e^2}{r_{ij}} + \sum_{i=1}^{N}\zeta(r_i)\mathbf{s}_i \cdot \mathbf{l}_i$$

where e and m are the electrical charge and electron mass, respectively, N is the number of electrons in the fully occupied shell, r_i is the spatial coordinate of the i-th electron , r_{ij} is the relative position of the electron i with respect to the electron j, $\mathbf{s}_i$ and $\mathbf{l}_i$ are the spin and angular momentum of the i-th electron, and $\zeta(r_i)$ is the spin-orbit interaction constant. The first term (T) represent the cinetic energy, the second (V_{en}) the electron-nucleus elctrostatic interaction, the third (V_{ee}) the electron-electron electrostatic interaction, the fourth (V_{so})the spin-orbit interaction.
The problem can be simplified, introducing the *central field Hamiltonian*, as follows:

$$H_{cf} = \sum_{i=1}^{N}[-\frac{\hbar^2}{2m}\nabla_i^2 + U(r_i)]$$

where U is the central potential, that includes V_{en} and the spherical part of V_{ee}.

In this approximation is assumed that each electron is moving *indipendently* from the others in a field of the form: $\frac{U_i}{e}$.

The corresponding Schrödinger equation, $H\psi = E\psi$, has solutions such as:

$$\psi = \prod_{i=1}^{N} \psi^i \qquad con \qquad E = \sum_{i=1}^{N} E^i$$

where ψ^i and E^i are eigenfunctions and eigenvalues of the single-electron operator.

Since all the terms of H_{cf} have spherical symmetry, the degeneracy of the $4f$ electrons is not removed and the solutions of the equation have the same structure as for the hydrogen atom.

Due to the Pauli exclusion principle, the total eigenfunction must be antisymmetric; in this way we obtain the N-particles wavefunction in the Slater-form:

$$\psi(x_1 x_2 \ldots x_n) = \frac{1}{\sqrt{N!}} \sum_{i=1}^{N!} (-1)^{p_i} P_i \psi(x_1)\psi(x_2)\ldots\psi(x_N)$$

where the sum is over the $N!$ permutations P_i of the electronic coordinates, and $(-1)^{p_i}$ equals ± 1 for even or odd permutations.

Up to this point of the theory, n, l e m_l are still good quantum numbers.

Obviously, this model based on the assumption of indipendent electrons can not describe the structure of the rare earth energy levels, and the perturbating potential $V = H - H_{cf}$ has to be introduced.

This removes the degeneracy and splits the energy levels, that can be calculated numerically.

Anyway, this approach is very complex from a numerical point of view and doesn't give a direct indication for the labelling of the energy levels.

If we assume that $V_{ee} \gg V_{so}$, the Russell-Saunders scheme (also called the *L-S scheme*) can be used: in this scheme V_{ee} assumes a diagonal form, $L = \sum_i l_i$ e $S = \sum_i s_i$ are good quantum numbers and can be used for the labelling of the energy levels.

Now it's necessary to consider the splitting of the energy levels due to the interaction with the crystal field of the host material: the crystal field can be considered as a perturbation for the rare earth ions (see fig.2.1 for the evaluation of the order of magnitude of the strength of the interaction). This removes also the degeneracy on the component of $J = L + S$ along the quantization axis, thus generating a set of sublevels (*Stark sublevels*).

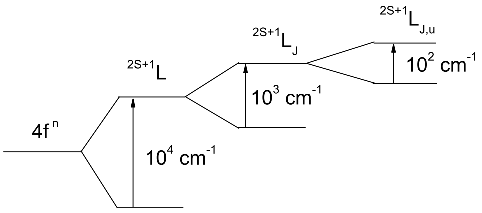

Figure 2.1: Rare earths energy splitting in crystals. - Typical values of the splitting energies in rare earth ions in crystalline hosts.

A correct labelling also for these sublevels can be given according to group theory, but this will not be discussed here.
As a conclusion to this section, in fig 2.2 the energy levels of all the triply ionized rare earth ions are reported, according to (23).

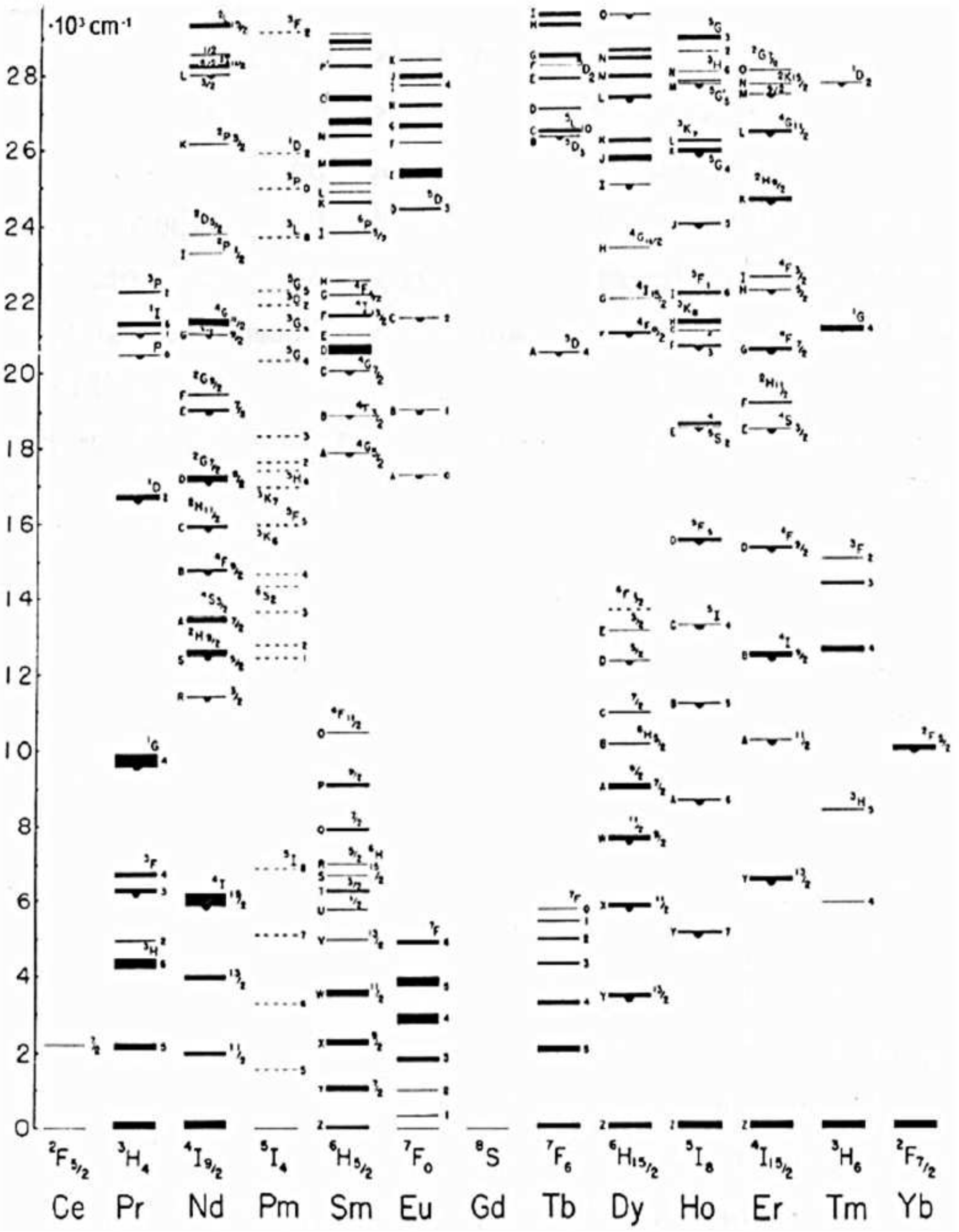

Figure 2.2: Rare earths energy levels - Energy levels of rare earth ions in crystals

2.3 The stimulated emission cross section

2.3.1 The β - τ method

The stimulated emission cross section is defined as the intensity gain of a laser beam per unity of population inversion when no saturation effects are present or no Excited State Absorption processes occur.

The $\beta-\tau$ method is based on the following assumptions: the energy differences between the J manifolds should not be too large, and the Boltzmann statistics holds for the population of each sublevel in case of steady pumping.

From the definition of σ it follows that the stimulated emission cross section is proportional to the B Einstein's coefficient, and this can be determined studying the absorption and spontaneous emission processes.

Named σ_{ji} e σ_{ij} respectively the spontaneous emission and absorption cross sections for the $j \to i$ transition, we have:

$$\sigma_{ji}(\nu) = \frac{g_i}{g_j}\sigma_{ij}(\nu) \tag{2.1}$$

$$\sigma_{ji}(\nu) = \frac{\lambda^2}{8\pi n^2}A_{ji}g_{ji}(\nu) \tag{2.2}$$

where g_i and g_j are the degeneracies of the $i-th$ and $j-th$ levels, A_{ji} is the spontaneous emission rate per time unit for the $i \to j$ transition, $g_{ji}(\nu)$ is the normalized line shape factor and n is the refractive index of the crystalline matrix.

In the low pumping regime, the fluorescence signal is given by:

$$I_{ji}(\nu)d\nu = GA_{ji}g_{ji}(\nu)h\nu d\nu N_j \tag{2.3}$$

where N_j is the population density of j level, and G is a calibration factor that represents the detected fluorescence, corrected for the optical response of the system.

The previous equations lead to:

$$I_{ji}(\nu)d\nu = G\frac{8\pi n^2}{c^2}h\nu^3 N_j\sigma_{ji}(\nu)d\nu \tag{2.4}$$

The $\beta-\tau$ method is used to calculate the emission cross section starting from fluorescence measurements, if the radiative lifetime of the interested manifold is known.

In case of a pulsed pump source, the temporal behaviour of the fluorescence is exponential with time constant τ_f:

$$\frac{1}{\tau_f} = W^R + W^{NR} = \frac{1}{\tau_R} + W^{NR} \tag{2.5}$$

where τ_R is the radiative lifetime, W^R and W^{NR} are the radiative and non-radiative relaxation rates, respectively.

One can define the radiative quantum efficiency of the manifold a, η_a, as follows:

$$\eta_a = \frac{\sum_b W^R_{ab}}{\sum_b W^R_{ab} + \sum_b W^{NR}_{ab}} = \tau_a \sum_b W^R_{ab} \tag{2.6}$$

that is the ratio between emitted photons and excited ions. According to this, one can write:

$$\frac{1}{\tau_R} = \sum_j f_j \sum_i A_{ji} = \frac{\eta}{\tau_f} \tag{2.7}$$

where f_j is the fraction of the population pumped into level j according to the Boltzmann statistics.

Once that τ_R is known, A_{ji} can be written as:

$$A_{ji} = \frac{\beta_{ji}}{f_j} \frac{1}{\tau_R} \tag{2.8}$$

where β_{ji} is the *branching ratio* for the $j \to i$ transition, i.e. the fraction of the total flux of photons emitted from the upper level. This value can be easily calculated from the measured fluorescence spectrum:

$$\beta_{ji} = \frac{\int \frac{I_{ji}(\nu)}{h\nu} d\nu}{\sum_{k,l} \int \frac{I_{kl}(\nu)}{h\nu} d\nu} = \frac{\int \lambda I_{ji}(\lambda) d\lambda}{\sum_{k,l} \int \lambda I_{kl}(\lambda) d\lambda} \tag{2.9}$$

In the steady-pump approximation, the total number of excited ions in the emitted multiplet N_{tot} is related to the population of the j-th level by means of the relation: $N_j = f_j N_{tot}$. If we sum over all the possible levels and frequencies on both sides of equation 2.3 and dividing by $h\nu$, we can use equation 2.9 obtaining:

$$\int \sum_{i,j} \frac{I_{ij}(\nu)}{h\nu} d\nu = \frac{G \eta N_{tot}}{\tau_f} \tag{2.10}$$

Solving eq. 2.10 for GN_{tot} and substituting into eq. 2.4 we get:

$$\sigma_{ji}(\nu) = \frac{\eta c^2}{\tau_f f_j(\int \frac{I(\nu)}{h\nu} d\nu) 8\pi n^2 h\nu^3} I_{ij}(\nu) \tag{2.11}$$

where $I(\nu) = \sum_{ij} I_{ij}(\nu)$ is the total fluorescence, and the integral is extended over the whole fluorescence spectrum.

Considering the superposition of the other $k \to l$ transitions, we have to correct the stimolated emission cross section as follows:

$$\sigma(\nu) = \sigma_{ij}(\nu) + \sum_{k,l} \frac{f_k}{f_l} \sigma_{kl}(\nu) \tag{2.12}$$

Substituting eq. 2.11 in eq. 2.12 and converting frequencies into wavelengths, we obtain:

$$\sigma(\lambda) = \frac{\eta \lambda^5}{\tau_f f_j(\int \lambda I(\lambda) d\lambda) 8\pi n^2 c} I(\lambda) \tag{2.13}$$

In eq. 2.13 all the terms are known or can be calculated but f_j, and it has become common practice to define an *Effective Stimulated Emission Cross Section* smply neglecting this factor.

Moreover, if the crystal presents different optical axis, eq. 2.13 has to be corrected as follows:

$$\sigma(\lambda) = \frac{\eta \lambda^5}{\tau_f \frac{1}{3} \sum_s (\int \lambda I_s(\lambda) d\lambda) 8\pi n^2 c} I_p(\lambda) \tag{2.14}$$

where the sum is extended over the three different polarizations and the index p labels the orientations.

2.3.2 The reciprocity method

When the overlapping of the absorption and emission does not allow reliable experimental determination of the emission cross section, as is often the case for example in Yb^{3+}-doped materials, another way to determine the emission probability is necessary. One can use the relations between the Einstein coefficients that connect the absorption and the stimulated emission in an energy system at thermal equilibrium, as pointed out by McCumber in (69). This method is often used in spectroscopy to obtain the emission cross section from the measured absorption spectra. Knowing the absorption coefficient and the doping concentration, in fact, the absorption cross sections can be calculated simply by:

$$\sigma_{abs}(\lambda) = \frac{\alpha(\lambda)}{d} \tag{2.15}$$

where d is the density of the dopant ion.

Once σ_{abs} is known, one can use the McCumber equation to obtain σ_{em}:

$$\sigma_{em}(\lambda) = \sigma_{abs}(\lambda)\frac{Z_l}{Z_u} \exp\left[\left(-\frac{E_{zl} - h\nu}{k_B T})\right)\right] \tag{2.16}$$

Here Z_l and Z_u are the partition functions of the lower and upper levels, k_B is the Boltzmann constant, T the temperature and E_{zl} is the energy separating the lowest Stark level of the lower manifold and the lower Stark level of the upper manifold (zero phonon line). This relation shows that the absorption and emission are closely related and that a large absorption cross section is then usually associated with a large emission cross section in Ytterbium-doped materials.

2.4 The Judd - Ofelt parameters

The works of Judd (43) and Ofelt (71), published indipendently in 1962, show a method for the calculation of the radiative transition rates between any two levels in rare earth-doped materials from absorption measurements: these are crucial parameters to determine the potentials of a rare-earth doped matrix towards a laser application. Quantum efficiencies can then be deduced, once the fluorescence lifetimes of the level are known. Here only the basics assumptions and conclusions of the theory are given, for the complete tractation the reader can refer to the original papers (43) (71).

Electric dipole transitions between 4f states are parity forbidden in a free ion Hamiltonan. However, when the rare earth ion is inserted in a host material the crystal field mixes 5d states with different parity with the 4f wavefunctions. That's the reason why 4f-4f transitions can occur. Judd and Ofelt introduced some assumption to obtain a relatively simple expression for the eletric dipole transition strength.

The assumptions are that the 5d states are degenerate, the energy differences between the 5d levels and the 5d levels are equal and all the Stark levels of the manifold are equally populated.

Under these conditions the strength of an electric dipole transition is given by (36):

$$S_{el}(a,b) = e^2 \sum \Omega_t \left| \langle a| U^t |b\rangle \right|^2 \tag{2.17}$$

where Ω_t are the Judd-Ofelt intensity parameters and U^t is the electric dipole tensor operator. The values of the matrix elements of U^t are host-independent and have been tabulated for transitions in rare earth ions in LaF_3 by Carnall (10).

The aim of the Judd-Ofelt analysis is to determine the Ω_t parameters, which describe the influence of the host on the ion. The following steps are the ones that are required to obtain the radiative transition rates from absorption spectra:

1) Calculate the oscillator strengths from integrated absorption measurements

2) Determine the transition strength by means of:

$$S(a,b) = \frac{3 g_a h \epsilon_0 c}{2\pi^2 \nu \chi} \int \sigma(\nu) d\nu \tag{2.18}$$

3) Calculate the magnetic dipole contribution to the transition strengths if present and substract from the measured one. This gives the electric dipole contribution, neglecting

the multipolar interactions.
4) Determine Ω_t by least-squares fitting the electric dipole transition strengths to eq 2.17.
5) Now the Ω_t parameters can be used in eq 2.17 to calculate the electric dipole contribution to the transition strength.
Combining this with the magnetic dipole allows for the calculation of transition rates between any two levels of the system. The sum of the transition rates to all lower states then gives the total radiative rate.

2.5 Energy transfer

In this work with the expression energy transfer one indicates all those processes that bring dopant ions to exchange excitation energy among each other.
It’s evident that a deep understanding of these processes brings to the possibility to predict and explain some characteristics of a laser material, since the energy that is stored via optical pumping in laser-active media is redistributed among the energy levels of the doping ion(s) in different ways before being re-emitted.
The main interaction mechanism is usually the dipole-dipole resonant interaction (Förster energy transfer) between ions. Also emission and reabsorption of photons can be significant over longer distances. As the strength of the dipole?dipole interaction rapidly vanishes with increasing distance between the ions (with the inverse sixth power of distance), its overall importance depends strongly on the doping concentration. Moreover, the effect of ion clustering in some matrices has to be considered. A detailed tractation of these processes can be found in (22). The main energy transfer processes in rare-earth doped materials are:

- Energy migration (fig 2.3). This process can occur among ions of the same or different species. The latter case is the most interesting since one can take advantage from pumping an efficiently absorbing ion (ion 1 in fig 2.3) and then obtain emission after energy transfer to the acceptor ion (ion 2 in fig 2.3). This is for example the case for Yb^{3+} - Er^{3+} doped samples, where one can pump efficiently Yb^{3+} ions (that have high absorption cross sections and allow for a high doping concentration) and obtain emission from Er^{3+} ions after $Yb^{3+} \to Er^{3+}$ energy transfer.

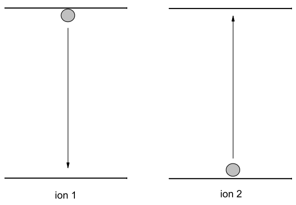

Figure 2.3: Energy migration. -

- Cross relaxation (fig 2.4). An ion in an excited state can transfer part of the energy to another ion in the ground state: as a result of this process, both ions end up in the same excited state. This process is used for example in Tm^{3+}-doped media, leading to quantum efficiencies above unity.

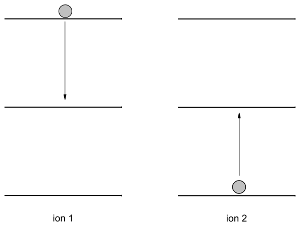

Figure 2.4: Cross relaxation. -

- Cooperative upconversion (fig 2.5). In this process an ion lying in an excited state gains energy from another ion that relaxes to a lower energy level. As a result, the first ion is promoted to a state with higher energy (fig 2.5). This process is used in many systems to convert light from the infrared to the visible range, as in the case of Er^{3+}.

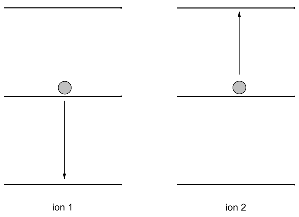

Figure 2.5: Cooperative upconversion. -

Chapter 3

Experimental setup

3.1 Experimental setup at Pisa laboratories

The main part of my work during this PhD period was carried out in the laboratories of the Physics Department in Pisa. Here a brief description of the experimental setups is given.

3.1.1 Crystal growth

The majority of the samples studied in this work were single crystals obtained by the Czochralski growth method.

The Czochralski (CZ) growth apparatus basically consists on a crucible which contains the raw materials, a heater capable of melting the charge, and a pulling rod positioned axially above the charge. Once the material in the crucible is melted, a small seed crystal attached to the end of the pulling rod is dipped into it and pulled upwards. Because of the surface tension between the seed and the melt, a small amount of liquid rises with the seed and crystallizes with the same orientation. During the pulling process the seed is rotated with a rotation speed of about 10 rpm to reduce the thermal inhomogeneities and to constantly mix the melt.

The CZ furnace apparatus in Pisa laboratory is shown in fig 3.1 and is equipped with a conventional resistive heater capable to reach temperatures of about 1400 C. The growth takes place in controlled atmosphere and high vacuum level down to 10^{-7} mbar can be achieved.

The crystal diameter is controlled by means of a reflectometer and the whole growth process is monitored via software.

Figure 3.1: Czochralski furnace. - Czochralski growth apparatus at Pisa laboratory.

3.1.2 X-Ray diffrattometer

In order to have informations about the single-crystal structure and the lattice orientation of the crystalline samples studied in this thesis, it's necessary to perform an X-Ray diffraction analysis. This was performed using a *HT Generator PW1830/40* and a Copper tube *PW2273/30 (Philips)* as X-Ray source. The source is broadband and not filtered in wavelength (the output is through a Berillium exit window).

The incidend rays are scattered by the sample, which is mounted on a goniometer, which resolution is ± 0.1° in the x and y directions and along z. The diffraction pattern is then acquired in back reflection by a photographic film, using a Laue chamber (*Flat Chamber 801* by *Huber*). The obtained image is then digitalized by an image scanner and then analysed using a specific software (*Orientexpress*).

3.1.3 Crystal processing

The crystal processing concerns cutting and polishing the samples with the desired orientation angles.

A precision cutter with a diamond wire was used to cut the crystals, mounted on a precision goniometer to obtain the desired orientation.

The polishing of the samples consisted in the use of alumina and diamond powders of decreasing dimensions, to obtain smooth surfaces. Particular care is of course taken for the laser crystals, where one has to reduce as much as possible the surface roughness, that has detrimental effects on the behaviour of the active medium. Also the orientation (plane, parallel surfaces or Brewster-angle orientation) is a critical parameter for the realization of a good laser crystal.

3.1.4 Laser sources

During this thesis, the doping ions that have been studied cover nearly the entire spectrum of the visible and near infrared region, and different laser sources have been used to excite this ions.

Here is a (non complete) list of the lasers that were present in Pisa laboratory at the time of this work:

CW Titanium Sapphire

A *Coherent Innova 300* Ar^{3+} laser is used to pump a home-made X-folded cavity Titanium Sapphire laser. This is tunable between 745 and 840 nm continuously by means of a quartz plate inserted in one arm of the cavity. The maximum power that was possible to obtain is about 250 mW, mainly limited by the pump power (about 2 W in multi-line operation mode).

Pulsed Titanium Sapphire

The pulsed Titanium Sapphire laser is pumped by the second harmonic of the 1.06 μm radiation of a Q-switched Nd:YAG laser (*Surelite I-10* by Continuum). The pulse duration is about 30 ns and the repetition rate is 10 Hz. The laser is tunable between 760 nm and 980 nm by means of a Sapphire prism, and the output energy per pulse is around 9 mJ.

DPSS lasers

These are compact Diode-Pumped all-Solid-State lasers by *CNI*. During this work I used two DPSS emitting at 532 nm (200 mW) and 473 (100 mW). Despite the quite low output power, these sources are particularly suitable for those applications in which a good TEM_{00} beam quality is required.

Laser diodes

Several laser diodes (both fiber coupled and free running) have been used during this work, ranging from the blue pectral region to the mid infrared. The advantages of using these laser sources, despite their generally poor beam quality, is that they are compact and cheap devices, and the power they can supply is enough for the spectroscopic applications that have been performed during my work.

3.2 Steady state fluorescence measurements

In this section the experimental setup used for the measurements of the steady state fluorescence spectra is described (fig 3.2).

The sample is excited by focusing the laser radiation with a 10 cm focal length lens. Then the fluorescence signal is collected perpendicular to the pump beam by a 7.5 cm infrasil lens, chopped and focused into the slits of a *Jobin Yvon* monochromator with 25 cm focal length. The monochromator is fully controlled via software and is equipped with three different gratings: 1200 gr/mm blazed at 0.5 μm, 600 gr/mm blazed at 1 μ, and 300 gr/mm blazed at 2 μm. Eventually, the light is filtered by long-pass or band-pass filters in order to prevent part of the pump beam from being focused into the monochromator.

The light signal is then detected by a suitable detector, amplified by means of a lock-in amplifier and then collected and stored on a PC for data analysis.

The obtained spectra are finally corrected for the optical response of the system using a halogen lamp as a 3000 K black-body reference source.

3.3 Decay time measurements

The experimental setup for decay time measurements is similar to the one described in the previous section, but with the implementation of a pulsed or chopped laser as excitation source (fig 3.3). Depending on the lifetime of the sample, the short pulse (30 ns) of the pulsed Ti-Sa laser or the chopped light of a cw laser was used. The signal is

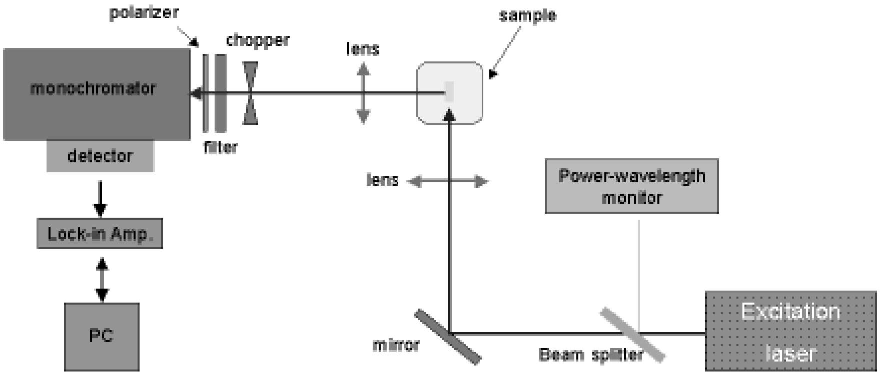

Figure 3.2: Fluorescence measurements setup - Schematic of the setup for fluorescence measurements.

then processed by fast amplifiers, displayed on an oscilloscope and stored on a PC. For lifetime measurements, particular care has been taken in order to excite the sample near an edge in order to reduce the radiation trapping effect. An interesting and reliable method to estimate the fluorescence lifetime avoiding this effect is the pinhole method described in ref (57): this method was adopted whenever there was a reasonable doubt on the measurements of the lifetimes with the ”standard” method.

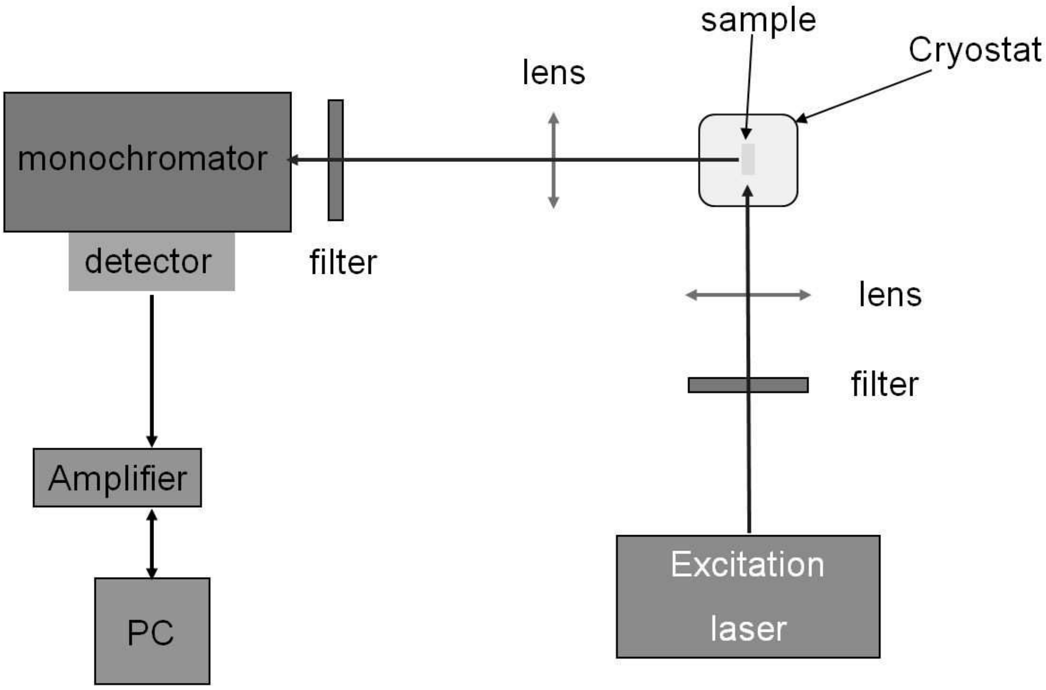

Figure 3.3: Lifetime measurements setup - Schematic of the setup for lifetime measurements.

3.4 Experimental setup at ILP laboratories in Hamburg

A part of my work during my PhD was carried out in the group of Prof. Günter Huber at the Insitute fuer Laser Physics in Hamburg, where the growth of Tm-doped sesquioxides thin films by the Pulsed Laser Deposition method was done.
In the following section the basic aspects of the experimental setups that were used for this work are described.

3.4.1 Pulsed laser deposition setup

The Pulsed Laser Deposition setup in Hamburg ILP laboratories is schematically shown in fig. 3.4. As excitation source a KrF excimer laser was used: the wavelength of emission is 248 nm, and the pulse energy can be varied and controlled up to circa 3 J with a pulse duration of 20 ns. The radiation of the laser is focused on the target via a 50 cm focal length lens, and the area of the target was scanned by means of scanning mirrors. The chamber consists of two units: the bigger one is the main chamber, where the deposition process takes place, and where the heated substrate and the target are placed. There is also a small chamber, that is the transfer chamber, which is in contact with the main chamber and can be separated via a valve, where one can store substrates and targets under vacuum, and can be used to mount new samples inside the main chamber without destroying the vacuum. Every movimentation inside the chambers can be performed via software-controlled manipulators, and so highly clean conditions can be achieved.
The main chamber is equipped with gas inlets in order to let background gases flow inside: for the deposition of oxide films in fact an oxigen atmosphere is required to compensate for the volatilization of oxigen during the growth.
The substrate was kept at high temperature (depending on the material) via an optical heater: a stack of laser diodes (7 X 20 W @ 980 nm) is fiber-coupled and focused into the chamber on a heatspreader (Aluminum Nitride), in thermal contact with the substrate itself. A pyrometer is used to monitor the temperature, that can reach values of about 1000°C.
The thickness of the deposited films can be controlled during the growth by means of an optical reflectometer implemented qith a blue diode: due to the different refractive index of the substrate and the growing film, the blue diode produces fringes that can be

counted observing the signal coming from a photodiode placed at the reflection angle. This give an information of the growth speed and is used to set the thickness of the films to the desired value. All the growth process is controlled via software, and a stop signal can be sent to the laser when the desired thickness is reached.
Another important in-situ analysis that was possible to perform was the RHEED analysis. This is an important tool to control the single-crystallinity of the growing film, but its use is not described in this work, since the growth of single-crystalline, lattice matched films was not completely performed.

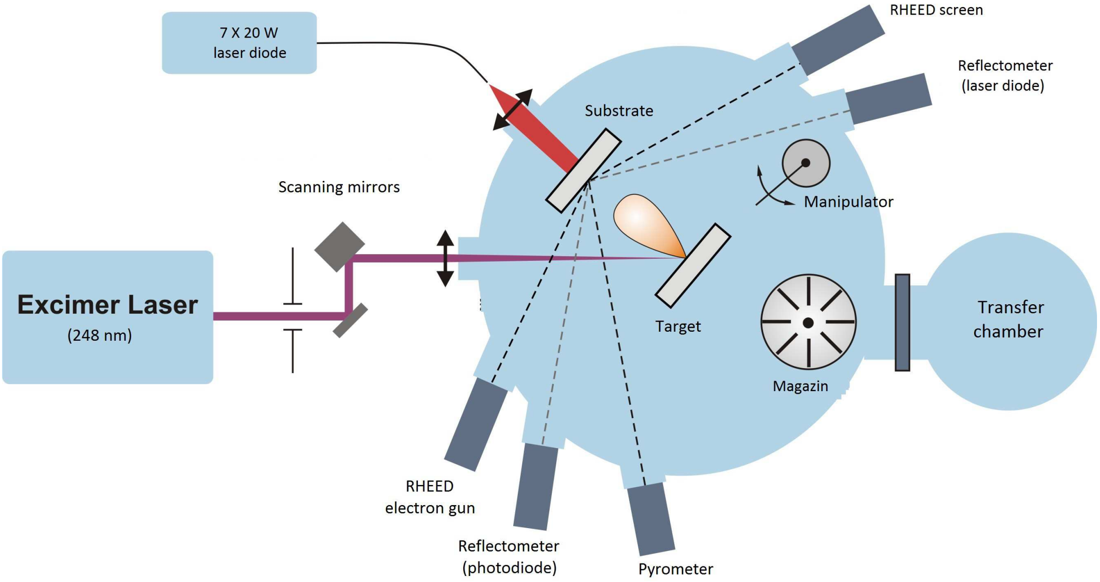

Figure 3.4: PLD setup - Schematic of the Pulsed Laser Deposition setup at ILP laboratories in Hamburg.

3.4.2 Atomic Force Microscope

The surfaces of the thin films deposited by means of the PLD technique were investigated by means of an atomic force microscope.
Also SEM (scanning electron analysis) was performed for some samples in NEST laboratories in Pisa, even though this latter technique is less indicated for insulating samples as the ones used in this work. AFM does not have this drawback and is a non-distructive technique that can give useful informations especially about the presence and size of dropplets on the surface of the observed samples. In the framework of this thesis the

measurements were taken in non-contact mode, and silicon cantilevers with spring constants k = 20 - 80 N/m were used for the analysis.

Chapter 4

Garnets - general aspects

In recent years Nd^{3+} doped crystals with broad absorption and emission bands have attracted much attention because they are ideal for pumping with AlGaAs commercial laser diodes, and good candidates as tunable and mode-locked laser materials.

A good example of such crystals are the Garnets, whose structure is shown in fig. 4.1. They are well known multi-center crystals, meaning that when a dopant ion is inserted into this kind of matrices it can occupy different locations and experience different crystal fields. Due to this, the position of the enery levels depends on the site in which the ion is placed and so multi-wavelength, broad emissions can be obtained (64) (88). Among these crystals, $Ca_3Ga_2Ge_3O_{12}$, $Y_3Sc_2Al_3O_{12}$, $Ca_3Sc_2Ge_3O_{12}$, $Ca_3(Nb,Ga)_2Ga_3O_{12}$, have shown attractive properties in the laser field (2, 4, 9, 12, 78, 82).

Usually, the multisite nature of these matrices is not evident at room temperature, because of the vibronic broadening of the emission (and absorption) bands, which tends to mask the different lines making them indistinguishable. So a low-temperature analysis is generally required, and the experiments are performed at cryogenic temperatures.

The interest on garnet crystals in optics is also linked to their thermo-mechanical properties. A high thermal conductivity is generally required for laser applications, where one has to cool down the active medium efficiently, in order to minimize the non radiative processes and to avoid damages caused by eccessive heating. Mechanincal properties are also important, for example for cutting and surface polishing of the samples. A good laser crystal also should be non-hygroscopic and so is expected not to modify its characteristics over a long operating period.

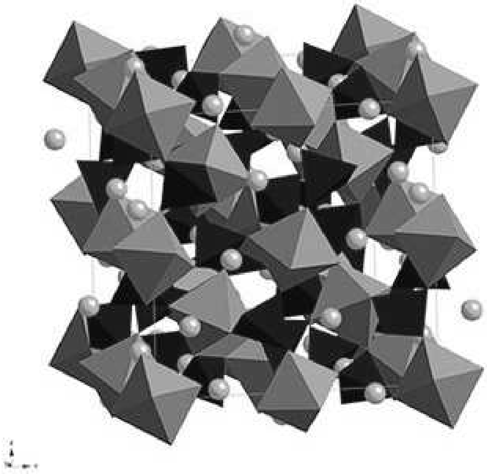

Figure 4.1: Garnets structure. - Schematic structure of garnet crystals.

Garnet crystals match quite well many of these requirements: it is a matter of fact that the largely widest diffused laser material, YAG, belongs to the family of garnets. The continued research on this class of materials is still very important because, for example, in rare earth-doped YAG lasers there is a lack of tunability that would be interesting to have for some applications. Moreover, YAG presents a core formation in the Chzochralski grown boules, that makes necessary a processing after the growth.

The research of new candidates as laser active media has continued also among the garnets, and a wide class of intermediate-gain laser crystals, known as *Mixed Garnets*, has been developed over the last 50 years. The pioneering works on mixed garnet materials date back to the 1960's, when the first papers on mixed Yttrium Aluminum Gallium Garnets were published (68), (67).

Later, the study of the possibility of doping with Nd^{3+} ions in these hosts was investigated, showing that different sites may be occupied and selective emissions could be obtained (76). Then, in the 1990's, many studies reported on fine compositional tuning for laser emission at precise wavelengths in order to match molecular lines of diluted gases in the atmosphere (93) (92). This works are of particular relevance because they show the potentials of these laser crystals for immediate applications in the field of remote sensing (82). More recently, in the last decade, mixed garnets found a resurgence of interest with the development of the ceramic technique for laser materials (35), and because of this they are expected to have a promising future with novel applications as versatile, low-cost, and high-performance gain media. In fact, thanks to the advent of commercially available high-power laser diodes, laser ceramics seem to play a key-role for those industry-oriented applications in which superior beam quality and high efficiencies are not required.

Among the garnets, Nd^{3+}-doped Gadolinium Gallium Garnet (GGG) crystal has been demonstrated to be a very interesting material for high-power solid-state laser operation (97), showing several advantages compared to Nd^{3+}-doped glasses and other garnet crystals: good thermal conductivity, easy fabrication with high growth speed (up to 5 mm/h), large segregation coefficient and no core formation. Unfortunately, the disadvantages of Nd:GGG crystal come from the high price and serious volatilization during the growth of the component Ga_2O_3. Thus, the search for an appropriate substitute for this component is of particular importance.

In this work two alternative materials are presented, both derived from the GGG crystal: the GAGG ($Gd_3Al_xGa_{5-x}O_{12}$) and the LGGG ($(Lu_x{+}Gd_{1-x})_3Ga_5O_{12}$). The former is derived from GGG by adding Al_2O_3 in the raw materials mixture (Al ions replacing Ga ions), the latter by adding Lu_2O_3 (Lu ions replacing Gd ions). This partial substitution of the GGG components is expected to bring new features in combination with Nd^{3+} doping: in fact, a modification of the crystal structure is reflected by the splitting of the energy levels of the dopant, which are sensitive to the surrounding crystal field.

Both crystals were deeply investigated in their spectroscopic properties in order to determine the positions of the energy levels of Nd^{3+} in these matrices, and their properties are discussed in chapter 6 and 7. Then, they were tested by other groups for cw and mode-locked operation. The results are discussed for each crystal, showing that their multisite structure can lead to interesting novel applications: in fact, despite that the relatively broad emission bands around 1 μm can not be used to compress pulses dow to the sub-ps regime, they give the possibility to obtain dual-wavelength operation in the pulsed regime that might be interesting for the realization of solid-state devices emitting in the Terahertz spectral range, via frequency difference combination. This will be discussed in details in chapter 8.

Chapter 5

Nd,Yb : GGG

Active media based on Yb^{3+} ions doped materials are well known for high power and ultrashort pulsed laser applications in a variety of conditions and geometries: from cryogenically cooled systems (66) to thin disk geometry (73) just to cite two novel trends in high power optics. Basically, this is due to the fact that laser action in the IR from Yb^{3+} ions shows several interesting properties, including the absence of excited-state absorption or upconversion processes, a small quantum defect, the possibility of a certain tunability and mode-locking operation.

At the same time many efforts have been devoted to the research for high quality and large dimension laser crystals to support such high amounts of energy. Yb^{3+} doped $Gd_3Ga_5O_{12}$ crystal is a good example of the combination of the above qualities. This crystal, grown by Czochralski and micro pulling down μ-PD methods, has been extensively studied in the past years due to its potential application for high power solid-state laser (32) (15). GGG crystals with large diameter and good optical quality can be grown by Czochralski method (41)(40) at relatively high pulling speed. The codoping with both Nd^{3+} and Yb^{3+} opens interesting perspectives, (85) (75) because of the possibility to use 800 nm AlGaAs laser diodes as pump sources, instead of InGaAs strained quantum well laser diodes at 980 nm, commonly used to pump Yb^{3+} -doped crystals.

Moreover, in Yb^{3+}-Nd^{3+} codoped crystals, bistable chromatic switching, (77) (39) (33) also referred to as *intrinsic optical bistability*, has attracted much attention in recent years due to its potential optoelectronic applications.

The motivation to study the codoped Nd^{3+},Yb^{3+}:GGG, is to determine whether it's possible to combine the good absorption properties of Nd^{3+} and the emission characteristics of Yb^{3+} with the good thermo-mechanical features of GGG as a host material. As a result, Yb^{3+} emission around 1 μm may be obtained by pumping Nd^{3+} with conventional LD in the 800 nm region where it presents high absorption cross sections, taking advantage of an efficient $Nd^{3+} \longrightarrow Yb^{3+}$ energy transfer (see the energy level scheme in fig 5.1).

In this chapter I'll report a detailed spectroscopic investigation of the Nd,Yb:GGG crystal with a specific focus on this energy transfer mechanism.

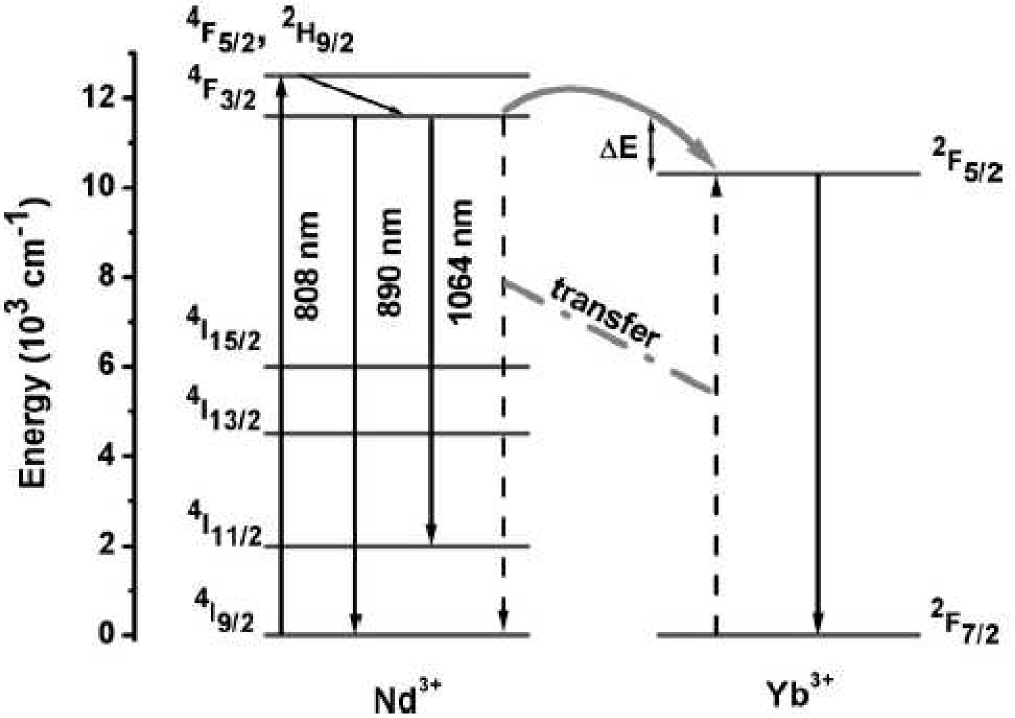

Figure 5.1: Nd,Yb:GGG, simplified energy-level diagram. - Simplified energy-level diagram of the Nd^{3+} and Yb^{3+} ions with energy-transfer mechanism. In the case of Nd^{3+} ions, only the levels of interest in this study are sketched.

5.1 Crystal growth

The concentrations of Nd^{3+} and Yb^{3+} were both of 5 at.% in the melt. These concentrations were adopted because good laser results have been obtained in Yb:GGG crystals (15) with this doping level. Regarding Nd^{3+}, the energy transfer efficiency is not very influenced by the donor (Nd) concentration (37), so a standard concentration was chosen in order to have a good absorption around 800 nm.

The crystal was grown in a RF inductive Czochralski furnace with Eurotherm temperature controller and Ir crucible. The pulling rate and the rotation rate were 1171.5 mm/h and 101720 rpm, respectively. Good optical quality samples with dimensions of ϕ = 20 x 30 mm^3 were obtained fig 5.2. The details of the crystal growth procedure, similar to that of the Nd:GGG crystal, can be found in (40).

A sample from the upper part of the boule has been cut and polished for absorption and emission spectroscopy measurements.

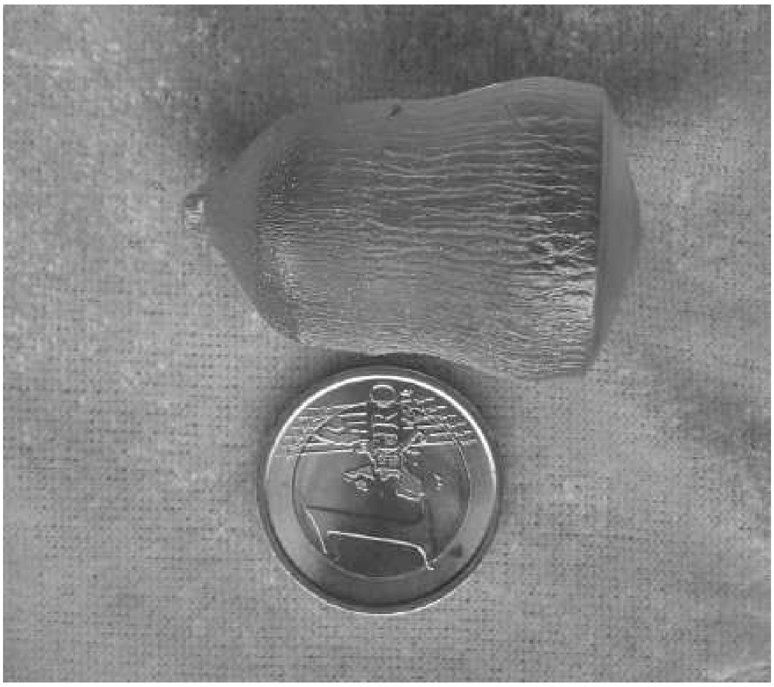

Figure 5.2: Yb,Nd:GGG, image of the crystal. - Image of the as-grown Yb,Nd:GGG crystal with 1 euro coin for contrast.

5.2 Spectroscopic analysis

5.2.1 Absorption and emission spectroscopy

The absorption spectrum was measured at room temperature in order to calculate the absorption cross sections. For this also the knowledge of the dopant concentrations in the sample is required.

In general, the dopant concentration of a sample [C$_s$] can be calculated by

$$C_s = C_m k_{eff}(1-g)^{keff-1} \tag{5.1}$$

where C$_m$ is the dopant concentration in the melt, k$_{eff}$ is the effective segregation coefficient, and g denotes the fraction of the crystallized melt. In literature the effective segregation coefficients of single-doped GGG are reported with values of 1.14 (15) for Yb^{3+} and 0.41 (86) for Nd^{3+}. Here we assume these values to be valid also in the case of codoping with Nd^{3+} and Yb^{3+}

Considering the factor g, in our case it only ranges from 0 to 0.18 in the whole growth process, i.e. only a small part of melt has been used in the growth process, so it can be almost neglected when calculating the dopant concentration. To support this, we performed absorption measurements on two different samples, cut from the upper and bottom part of the boule, which didn't show any difference within our instrument sensibility. So the concentrations of Yb^{3+} and Nd^{3+} ions in our sample can be calculated with values of 5.70 at.% (7.18 x 10^{20} ions/cm^3) and 2.05 at.% (2.58 x 10^{20} ions/cm^3), respectively.

The absorption cross sections are shown in fig 5.3, where one can find the strong absorption at 807.7 nm due to the ^{4}I$_{9/2}$ $\longrightarrow$ ^{4}F$_{5/2}$ + ^{2}H$_{9/2}$ transition in Nd^{3+}, and the absorption spectrum peaking at about 970 nm due to the transition between the lowest components of the ^{2}F$_{7/2}$ and ^{2}F$_{5/2}$ multiplets of Yb^{3+} ions. The broad absorption band located in the 910 ÷ 965 nm range comes from the strongly phonon coupled transitions to higher components of the ^{2}F$_{5/2}$ multiplet. Furthermore the absorption cross section of Nd^{3+} at 807.7 nm (σ_{abs} = 8.3 x 10^{-20} cm^{-2}) is about ten times the one at 970 nm (σ_{abs} = 0.82 x 10^{-20} cm^{-2}).

In table 5.1 a comparison with the peak values of the absorption cross sections of other popular laser crystals is given.

Table 5.1: Peak absorption cross section for the Nd^{3+} $^4F_{5/2}$ level (around 808 nm) for Nd-doped GAGG, YAG and $YLiF_4$ crystals at RT.

Matrix	σ_{abs} (x 10^{-20} cm^2)	Reference
GGG	8.3	This work
YAG	12	(58)
$YLiF_4$	3.7	(80)

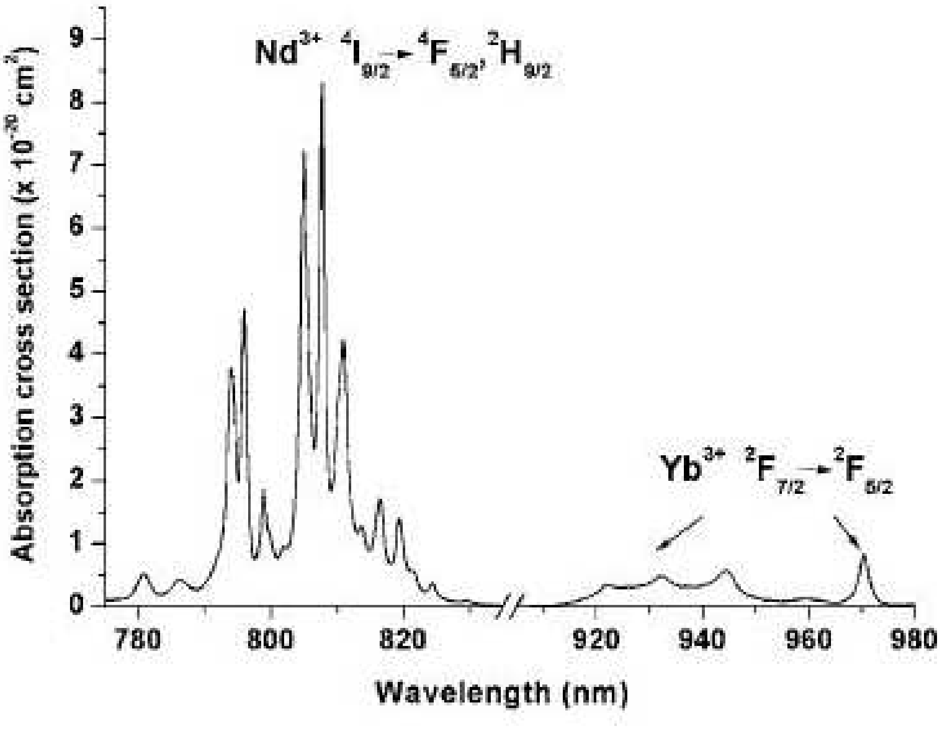

Figure 5.3: Yb,Nd:GGG, absorption cross sections. - Absorption cross sections of Yb,Nd:GGG. All data were derived by using the corresponding concentrations of Yb^{3+} and Nd^{3+} ions.

In fig 5.4 the fluorescence spectra measured at low temperature (10 K) and RT are presented. Pumping the crystal in the Nd^{3+} ^{4}F$_{5/2}$ level, we observe a strong fluorescence peak assigned to the Yb^{3+} ^{2}F$_{5/2}$ $\longrightarrow$ ^{2}F$_{7/2}$ transition located at around 1025 nm. On the other hand, the typical Nd^{3+} emission peaks around 1064 nm and in the spectral range of 1300 to 1450 nm are very small at RT, and even almost disappeared at 10 K when the absence of energy back transfer from Yb^{3+} to Nd^{3+} depopulates the Nd^{3+} ^{4}F$_{3/2}$ energy level.

The emission cross section for Yb^{3+} ions is calculated by the reciprocity method with the energy-level data found in Ref. (32). The result is shown in fig 5.5, where we can find that the calculated value for the emission cross section is σ_{em} = 8.3 x 10^{-21} cm^{-2} at 970.4 nm (zero phonon line) and the maximum value of σ_{em} = 1.6 x 10^{-20} cm^{-2} is obtained at 1024.6 nm. These results are comparable with those found in literature for other laser crystals, as shown in table 5.2.

Table 5.2: Peak emission cross section for the Yb^{3+} ^{2}F$_{5/2}$ level (around 1025 nm) for Nd-doped GAGG, YAG and YLiF$_4$ crystals at RT.

Matrix	σ_{em} (x 10^{-20} cm^2)	Reference
GGG	1.6	This work
YAG	2.3	(21)
YLiF$_4$	0.41	(16)

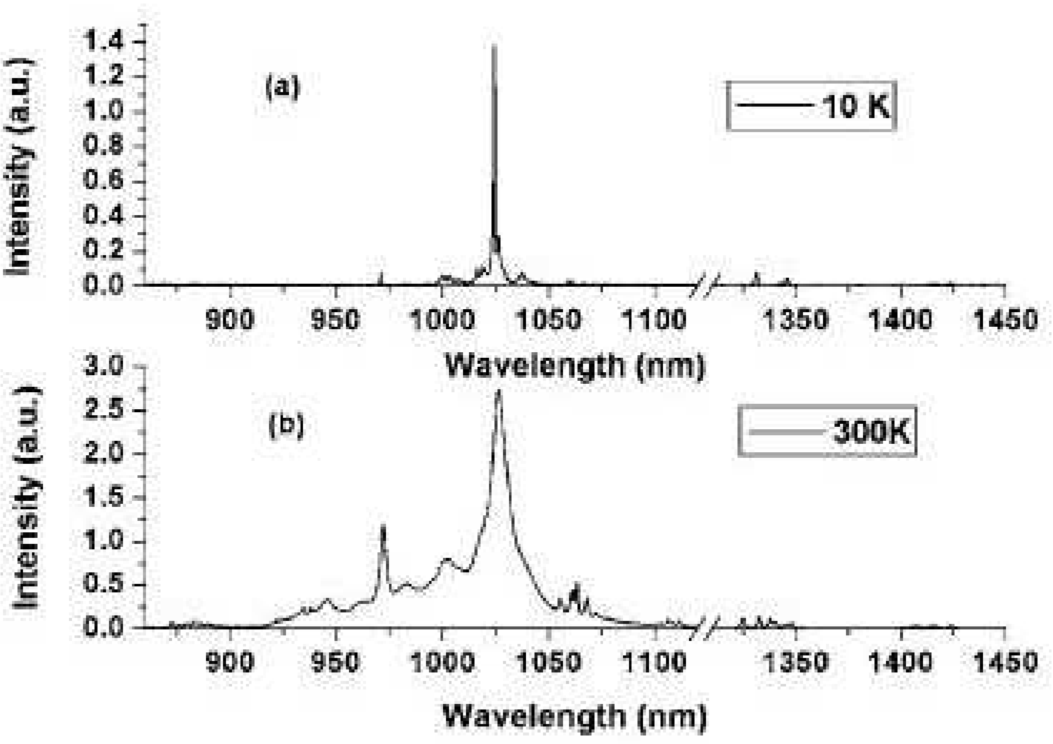

Figure 5.4: Nd,Yb:GGG, 10 K and RT emission spactra. - Emission spectra obtained under excitation at 805.2 nm at 10 K (a) and at 300 K (b). Corrected for grating efficiency and detection system spectral response. The resolutions are 0.2 nm from 850 to 1125 nm, and 0.6 nm from 1300 to 1450 nm.

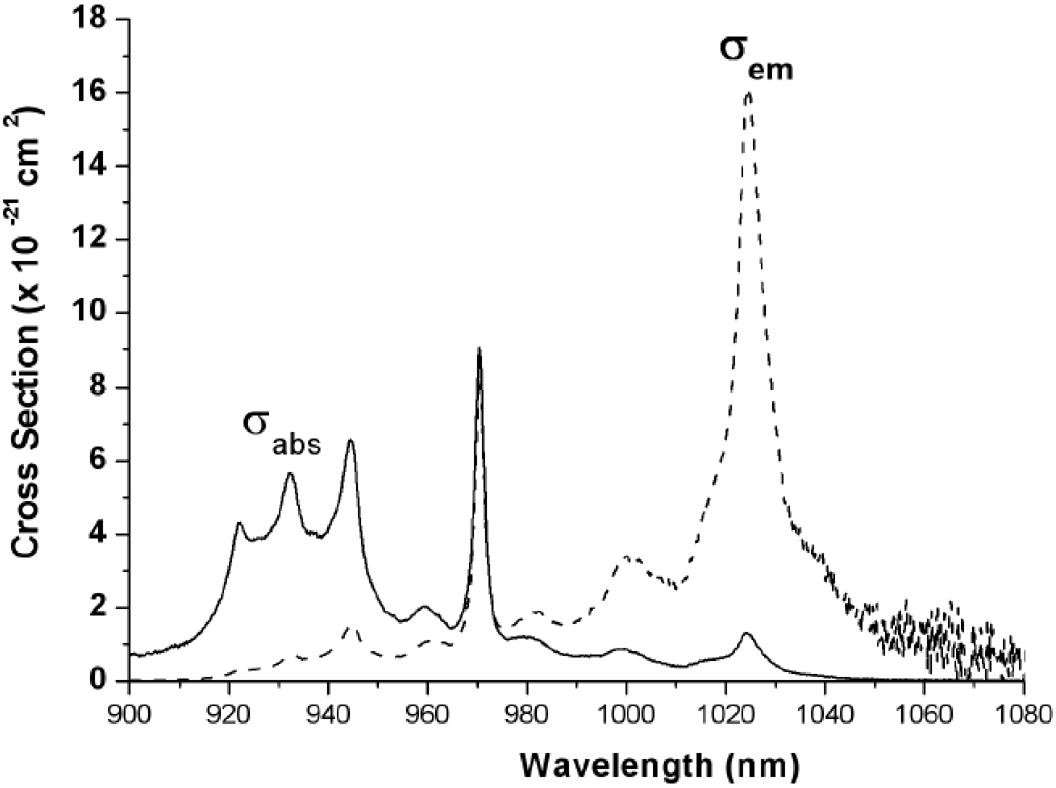

Figure 5.5: Yb,Nd:GGG, RT emission and absorption cross section. - Emission cross section (σ_{em}) of Yb^{3+} in Yb,Nd:GGG crystal at RT calculated by the reciprocity method, and absorption cross section (σ_{abs}) shown together.

5.2.2 Decay time kinetics

The dynamics of the emission from the upper multiplets of Nd^{3+} and Yb^{3+} was investigated.

The decay curves of the $^4F_{3/2}$ level of Nd^{3+} and the $^2F_{5/2}$ level of Yb^{3+} were measured between 9K and 300 K after pulsed excitation at 807 nm.

Here the decay time of the $^4F_{3/2}$ level of Nd^{3+} and the $^2F_{5/2}$ level of Yb^{3+} are named τ_{NdNd} and τ_{NdYb} respectively, where the first subscript denotes the pumped ion, and the second one is the luminescent ion.

The temperature dependence of decay times of Nd^{3+} and Yb^{3+} ions is shown in fig 5.6. The Nd^{3+} decay is nonexponential, and the average τ_{NdNd} is obtained by the τ-integral equation (6):

$$\langle \tau \rangle = \frac{\int I(t)dt}{I_0} \tag{5.2}$$

Here I(t) is the intensity at time t, and I_0 is the maximal value of the intensity. It can be found that τ_{NdNd} is almost constant, for the sensitivity of our apparatus (1 μs) from 9 to 77 K, then increasing up to 15 μs at 300 K. This can be motivated by the presence of reabsorption of radiation in the crystal, caused by the population of the ground state $^4I_{9/2}$ sublevels by Boltzmann distribution.

Concerning Yb^{3+} decay, it is exponential with time constant of about 1 ms at room temperature (as in Yb^{3+} singly-doped GGG (32) (15)). As shown in fig 5.6, τ_{NdYb} increases from 9 K (935 μs) to 190 K (1073 μs) and then decreases with temperature rising (983 μs at 300 K). This behaviour can be explained with the presence of reabsorption of radiation in the crystal, as explained for τ_{NdNd}. At the same time this effect is contrasted by the depopulation coming from the thermally enhanced energy back transfer probability from Yb^{3+} to Nd^{3+} ions, arising at about 200 K.

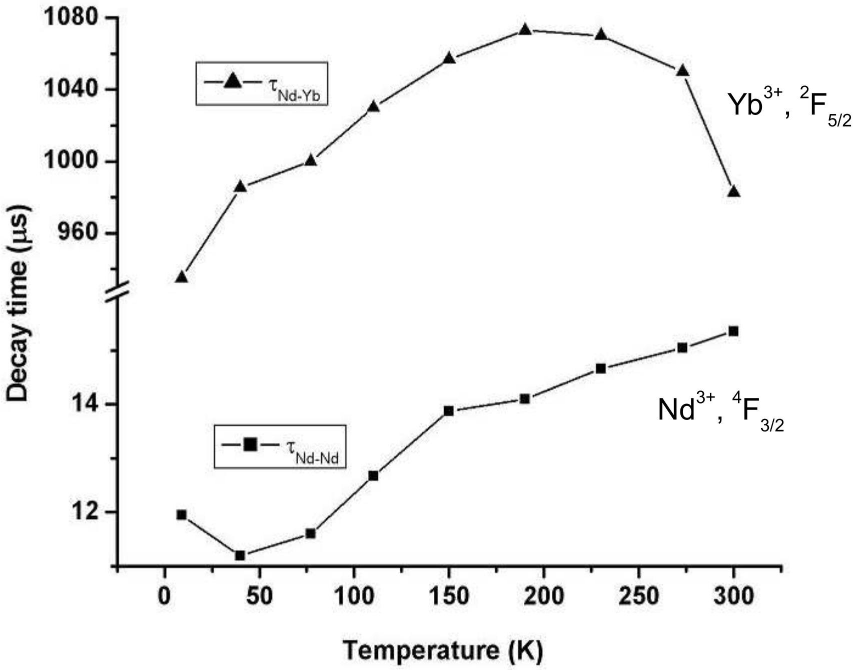

Figure 5.6: Nd,Yb:GGG, T-dep. decay time (Nd^{3+} pumping). - Decay time of Nd^{3+} and Yb^{3+} fluorescences by excitation of Nd^{3+} at 807 nm from 9 to 300 K. Here τ_{NdNd} and τ_{NdYb} denote the decay time of the $^4F_{3/2}$ level of Nd^{3+} and the $^2F_{5/2}$ level of Yb^{3+}, respectively.

5.2.3 Evaluation of energy-transfer efficiency

In this section I will describe the calculation of the energy-transfer efficiency at 77 K and 300 K.

Two different approaches were adopted, depending on the data found in literature that were necessary to perform this calculation: from the data of decay time and from the emission spectra. This study is very important to understand the possibility to use this codoped crystal to develop an efficient laser operating on the Yb^{3+} emission.

At 77 K the energy transfer efficiency η_t can be calculated by the formula (96) (20)

$$\eta_t = 1 - \frac{\tau_{NdYb}}{\tau_{Nd}} \tag{5.3}$$

where τ_{Nd} is the ^{4}F$_{3/2}$ level decay time of Nd^{3+} in a Nd^{3+} single doped GGG crystal (with the same Nd^{3+} concentration of our sample). The variation of τ_{Nd} with concentration at 77 K, based on Dexter and Schulmans theory (22), is given by

$$\tau = \frac{\tau_0}{1 + \left(\frac{C}{C_0}\right)^2} \tag{5.4}$$

where τ and τ_0 are the lifetime of the ^{4}F$_{3/2}$ level and the lifetime of the low Nd^{3+} concentration limit, C is the concentration of Nd^{3+} ions, and C$_0$ is the Nd^{3+} concentration when the fluorescence lifetime decreases to half of τ_0 ($\tau_0 = 282$ μs , C$_0$ = 3.46 x 10^{20} cm^{-3}) (65). As we mentioned above the concentration of Nd^{3+} ions in our sample is about 2.05% ($\approx$ 2.60 x 10^{20} cm^{-3}), and τ_{NdNd} measured at 77 K is 11.6 μs, so an energy-transfer efficiency η_t of 94% at 77 K can be calculated from eqs. 5.3 and 5.4.

The energy-transfer efficiency at 300 K was estimated from the emission spectra (38) (61) because of the absence of the exact value of decay time (τ_{Nd}) of 5% Nd:GGG at RT in literature and the absence of an equal sample in our lab. The η_t (i.e. the number of Nd^{3+} ions de-excited via Yb^{3+} emission divided by the total number of Nd^{3+} ions de-excited per unit of time) can be given as

$$\eta_t = \frac{W_t n_{Yb_1}}{W^r_{Nd} + W^n_{Nd} r + W_t n_{Yb_1}} \tag{5.5}$$

where W$_t$ is the Nd^{3+} $\longrightarrow$ Yb^{3+} energy-transfer term, n_{Yb_1} is the population density of the Yb^{3+} ^{2}F$_{7/2}$ level, and W$_{Nd}{}^r$ + W$_{Nd}{}^{nr}$ is the total de-excitation rate of the Nd^{3+} excited ions in the absence of energy transfer. Then, η_t can be given in terms of emission spectral data and intrinsic quantum efficiencies of Nd^{3+} (η_{Nd}) and Yb^{3+} (η_{Yb}) as follows:

$$\eta_t \approx \frac{\frac{1}{\eta_{Yb}} \int_{1120nm}^{850nm} I_{Yb}(\lambda) d\lambda}{\left(1 + \frac{\beta_{^4I_{13/2}} + \beta_{^4I_{15/2}}}{\beta_{^4I_{9/2}} + \beta_{^4I_{11/2}}}\right) \frac{1}{\eta_{Nd}} \int_{1120nm}^{850nm} I_{Nd}(\lambda) d\lambda + \frac{1}{\eta_{Yb}} \int_{1120nm}^{850nm} I_{Yb}(\lambda) d\lambda} \tag{5.6}$$

where I(λ) denotes the intensity of emission spectra at wavelength λ, and $\beta_{^4I_{J/2}}$ (J = 9, 11, 13, and 15, respectively) represents the branching ratio of the Nd^{3+} transitions in GGG. The values of $\beta_{^4I_{J/2}}$ can be found from previous works (55) (63) ($\approx$ 0.35, 1.54, 0.11, and 0.003, with J = 9, 11, 13, and 15, respectively), and the quantum efficiency of Yb^{3+} (η_{Yb}) is about 0.9 in 5.7 at.% Yb:GGG (14). For the quantum efficiency of Nd^{3+} (η_{Nd}) at RT, it is estimated from Nd-doped Gadolinium Scandium Gallium Garnet (GSGG) (56) with a value of 0.79.

Now, the energy transfer efficiency value of $\eta_t = 84\%$ can be obtained by Eq. 5.6: this is among the largest values in Nd^{3+},Yb^{3+} co-doped crystals. The result means that there is very efficient energy transfer from Nd^{3+} to Yb^{3+} in GGG, and this is favorable for its potential laser applications.

5.2.4 Analysis of $Nd^{3+} \leftarrow Yb^{3+}$ energy back transfer

In Sec. 5.2.3 an energy-transfer efficiency of 94% at 77 K and 84% at RT was calculated. So an energy back transfer process begins to be effective at temperatures below RT. We carefully tried to capture the Nd^{3+} emission when pumping Yb^{3+} ions at 970 nm in the range from 9 to 300 K, and the decay times of Yb^{3+} (τ_{Yb-Yb}) and Nd^{3+} (τ_{Yb-Nd}) ions were also obtained as shown in fig 5.7, together with τ_{Nd-Yb} for contrast. Both decay profiles of Nd^{3+} and Yb^{3+} have exponential behaviour when pumping at 970 nm.

From fig 5.7 it can be found that τ_{Yb-Yb} and τ_{Nd-Yb} show the similar tendency in all the temperature from 9 to 300 K, and the fluorescence of Nd^{3+} has the same decay constant of Yb^{3+}, as it appears distinctly above 190 K. This means that thermally activated $Nd^{3+} \leftarrow Yb^{3+}$ back transfer begins to take place at about 190 K, becoming stronger and stronger with temperature increasing. So the trend of the energy-transfer rate can be explained as follows: below 190 K the energy-transfer efficiency increases with temperature. Above 190 K the increasing speed reduces due to the thermally activated $Nd^{3+} \leftarrow Yb^{3+}$ back transfer, so the energy transfer efficiency reaches a maximum and then decreases with temperature rising. As a result the maximum of energy-transfer efficiency in this crystal is expected to be located at temperatures between 190 K and 300 K.

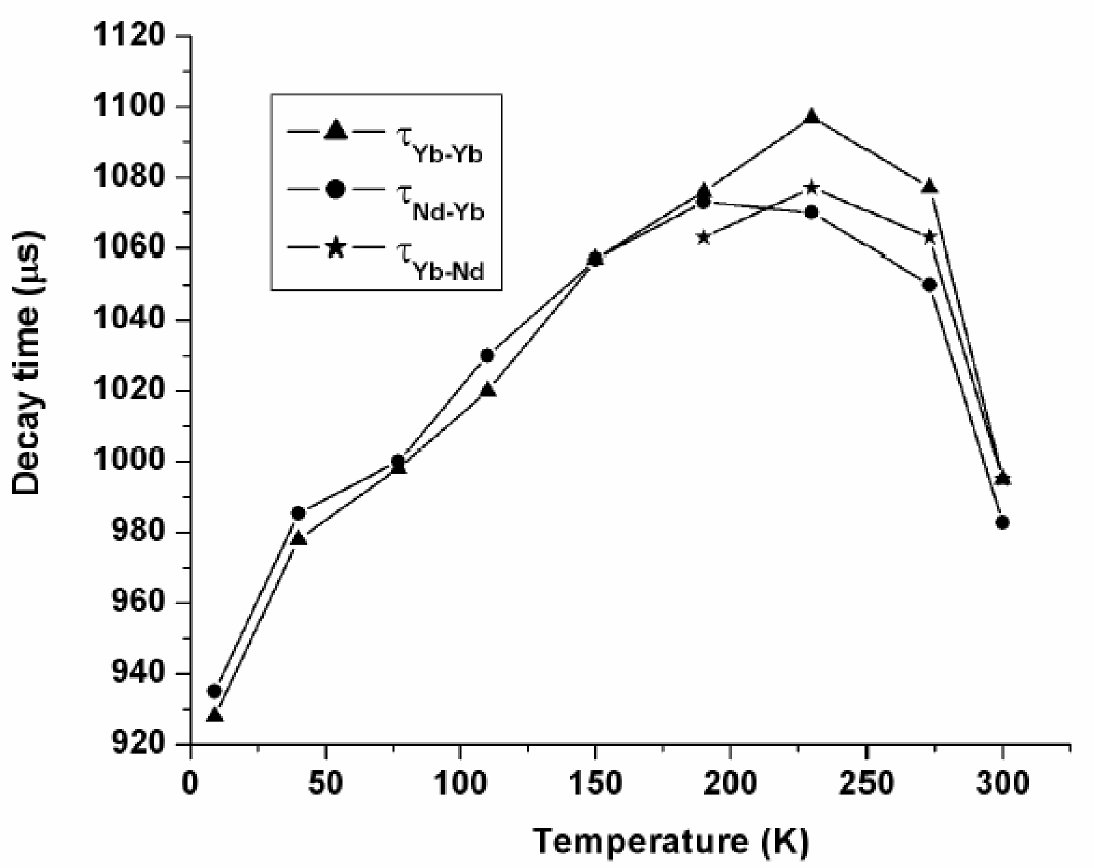

Figure 5.7: Nd,Yb:GGG, T-dep. decay time (Yb^{3+} and Nd^{3+} pumping compared). - Decay time of Nd^{3+} and Yb^{3+} fluorescences by excitation of Yb^{3+} (at 970 nm) or Nd^{3+} (at 808 nm) from 9 K to 300 K. Here the first alphabet in the legends denotes the pumped ions, and the second one means the luminescent ions.

5.2.5 Analysis of the decay curve: Nd^{3+} $\longrightarrow$ Yb^{3+} energy-transfer mechanism

As described in Sec. 5.2.2, the decay curves of Nd^{3+} from the ^{4}F$_{3/2}$ level display a nonexponential behavior. The intensity of luminescence can be fitted by the formula (38) (7) (27):

$$I(t) = I_0 exp\left(-\frac{t}{\tau_0} - \gamma_S t^{3/S} - \omega t\right) \tag{5.7}$$

where t is the time after excitation, τ_0 is the intrinsic lifetime of Nd^{3+} in GGG crystal, γ_S is a constant related to the direct Nd^{3+} $\longrightarrow$ Yb^{3+} energy transfer, where S = 6, 8, and 10 stand for dipole-dipole, dipole-quadrupole, and quadrupole-quadrupole interactions, and ω is the migration parameter taking into account the donor migration. The decay curve at 300 K was fitted to Eq. 5.7, and the best result was obtained for S = 6 as shown in fig 5.8. This means that the dominant energy-transfer process is the electric dipole-dipole interaction. From the fitting the value of $\gamma_6 = 243 \pm 6$ s$^{-1/2}$ has been achieved.

Finally, the energy-transfer microparameter (C_{DA}), which represents the efficiency of a donor-acceptor system for energy transfer independently of the donor-acceptor distance, can be calculated from (38)

$$\gamma_6 = \frac{4}{3}\pi^{3/2}\rho_A\sqrt{C_{DA}} \tag{5.8}$$

where ρ_A is the acceptor density. Here the Yb^{3+} concentration $\rho_A \approx 7.20$ x 10^{20} cm^{-3} (5.70 at.%) is applied, and a value of 2.1 x $10^{-39} cm^6 s^{-1}$ is obtained for C_{DA} using eq. 5.8. This is an interesting value if compared with other Nd^{3+},Yb^{3+} codoped glasses and crystals, such as 18 x 10^{-39} (YA1$_3$(BO$_3$)$_4$ crystal), 6.0 x 10^{-39} (borate glass), 3.8 x 10^{-39} (tellurite glass), 1.6 x 10^{-39} (metaphosphate glass), 0.34 x 10^{-39} (fluoroindogallate glass), and 0.56 x 10^{-39} cm^6 s^{-1} (Sr$_{0.6}$Ba$_{0.4}$Nb$_2$O$_6$) (38) (8).

Such a high value of C$_{DA}$ can be explained in term of Yb^{3+} and Nd^{3+} ions17 multicenter distribution and inhomogeneous broadening of the absorption and emission spectra risulting from the disordered structure typical of garnet crystals (70).

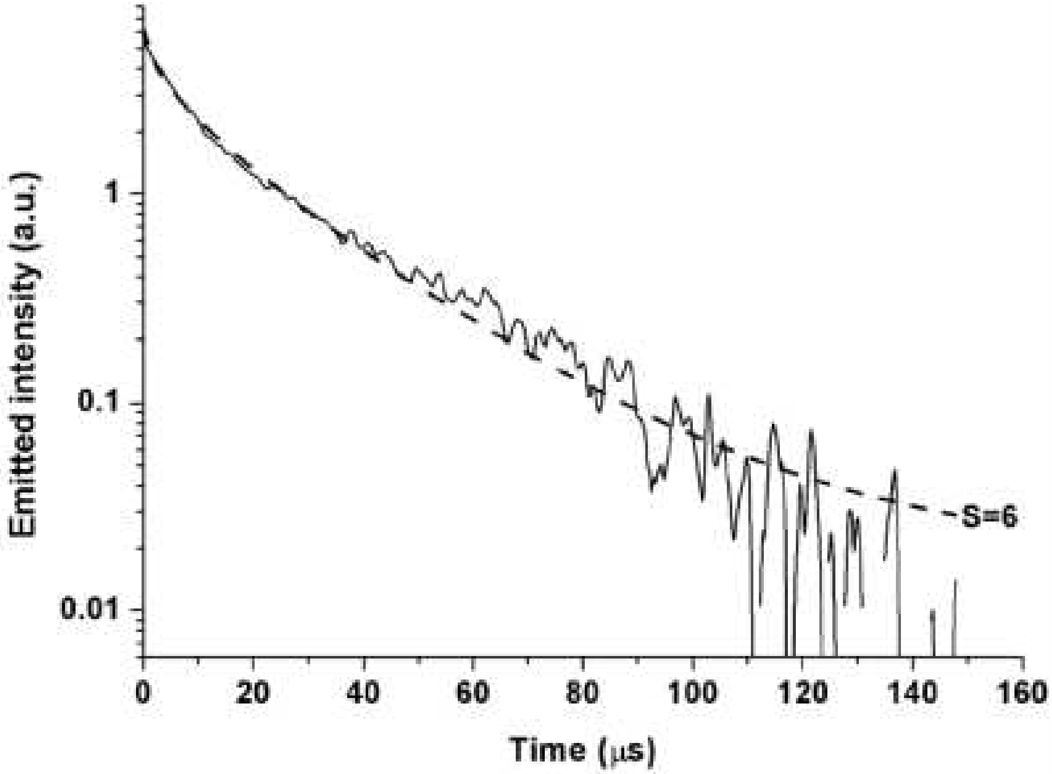

Figure 5.8: Nd,Yb:GGG, Nd^{3+} fluorescence decay fit. - Best fit of the time dependence of Nd^{3+} emission at RT to Eq. 5.7 for dipole-dipole interaction (S=6).

5.3 Summary

In this chapter a detailed spectroscopic characterizations of Czochralski-grown Yb,Nd:GGG crystal was presented.

The absorption spectrum has been measured at RT with a notable cross section value of 8.3 x 10^{-20} cm^2 at 807.7 nm, very favorable for pumping with powerful AlGaAs QW LD.

Emission spectra at 10 K and RT have been obtained by pumping Nd^{3+} at 805 nm with a cw LD, and the strong emissions of Yb^{3+} around 1.02 μm were observed as expected.

Lifetime measurements show strong temperature dependence when pumping the sample at 807 nm. The Nd^{3+} decay increases from 12 μs at 9 K to 15 μs at 300 K: when temperature rises, the overlap between emission and absorption bands is increasingly important and some radiation trapping is present in the crystal, causing the lengthening of the lifetime of the $^4F_{3/2}$ level. Concerning the lifetime of the Yb^{3+} $^2F_{5/2}$ level in function of the temperature (fig 5.6), the increase in the time constant with temperature is due to reabsorption of radiation by Yb^{3+} ions. Above 200 K the value of the lifetime decreases with temperature rising, due to the thermally activated $Nd^{3+} \leftarrow Yb^{3+}$ energy back transfer process. This point is validated by the analysis performed pumping the sample at 970 nm from 10 to 300 K: Nd^{3+} emission was detected above 190 K, proving the effectiveness of $Nd^{3+} \leftarrow Yb^{3+}$ energy back transfer process.

From the data of decay time and from the emission spectra, large energy-transfer efficiency values of 94% at 77 K and 84% at 300 K, respectively have been calculated.

At the same time, the energy transfer microparameter C_{DA} was estimated with a value of 2.1 x 10^{-39} cm^6 s^{-1}, fitting the nonexponential Nd^{3+} decay curve at 300 K.

The analysis exposed in this chapter may be considered a good starting point in order to determine the best values for Nd^{3+} and Yb^{3+} for laser tests.

Chapter 6

Nd : GAGG

In chapter 4 the problem of finding appropriate alternatives to the well known Gadolinium Gallium Garnet laser crystal was briefly discussed. Here a possible alternative is presented, obtaiend from the GGG by adding the Al_2O_3 component that partially replaces Ga_2O_3, following the former studies on $Gd_3Al_xGa_{5-x}O_{12}$ (GAGG) where crystal structure, dislocations and thermal conductivity were reported (50) (51) (52). As will be shown, this leads to slight modifications of the emission and absorption properties of this material doped with Nd^{3+}. In particular, even though this doesn't introduce additional occupational sites for Nd^{3+}, this new composition allows for interesting multiwavelength laser operation in mode-locked regime, as will be presented in chapter 8. So the idea is to study the optical properties of this material with particular attention to the multisite distribution of Nd^{3+} ions in the lattice. This results in different emission and absorption peaks shifted by a few cm^{-1}, clearly visible in the low temperature spectra. At room temperature (RT), these peaks are broader and the overlap between them results in broad emission and absorption bands, which contribute to a certain tunability around 1 μm as well as to the possibility to compress the pulses in ps mode-locked operation.

6.1 Crystal growth

A single crystal with the nominal composition $Gd_3Al_xGa_{5-x}O_{12}$ (with x = 1) doped with Nd was grown by the conventional Czochralski method at the State Key Laboratory of Crystal Materials of Shandong University in China. The powders of Gd_2O_3, Ga_2O_3, Al_2O_3, and Nd_2O_3 (1.92 at% relative to Gd in the melt) were mixed by a planetary mixer and pressed into tablets. Then, polycrystalline material was obtained by sintering the tablets at about 1200 C for 25 h. The crystal growth was carried out in an radiofrequency-heated apparatus under the mixed atmosphere of Ar plus 20 vol% CO_2, and the growth parameters were about 1 mm/h for the pulling rate and 20 rpm for the rotation rate. Good optical quality crystals were obtained and then processed for the following optical analysis. The measurement of concentration of Nd and Al ions in the as-obtained crystal was performed by the x-ray fluorescence method and showed a doping level for Nd and Al of 0.74 at% (0.95 x 10^{-20} ions/cm^3) and 19 at%, respectively.

6.2 Spectroscopic analysis

The absorption spectra were collected at both 10K and RT. The analysis of the absorption peaks showed no clear evidence of impurities in the crystal, ensuring the good chemical quality of the sample.

Absorption data at RT show the expected broad absorption band around 800 nm, corresponding to the $^4I_{9/2} \rightarrow {}^4F_{5/2} + {}^2H_{9/2}$ transition. In fig 6.1 the region from 400 to 900 nm and, in particular, the 800 nm wavelength band is reported. It is important to notice that the whole absorption band around 800 nm extends from 780 to 830 nm, with a particularly interesting region between 800 and 815 nm, where one can find three peaks that are suitable for pumping with powerful commercial laser diodes at 805.3 nm, 807.9 nm and 811.3 nm (see tab 6.1).

Table 6.1: Main absorption peaks in the $^4F_{5/2} + {}^2H_{9/2}$ level of Nd:GAGG crystal at RT.

λ(nm)	$\Delta\lambda$ (nm)	$\alpha(cm^{-1})$
805.3	2.3	5.1
807.9	1.5	7.0
811.3	2.5	3.6

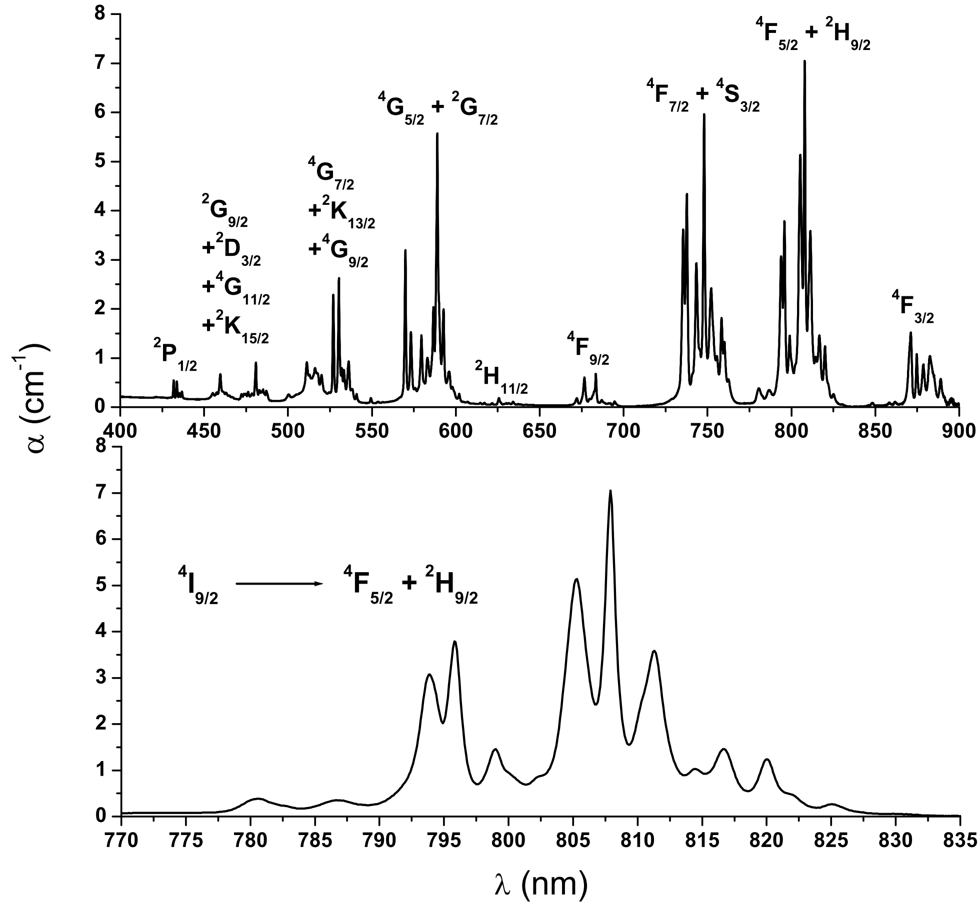

Figure 6.1: Nd:GAGG, RT absorption - Room temperature absorption spectrum of Nd:GAGG crystal

From absorption (and emission) spectra at 10K the position of the energy levels of Nd^{3+} can be determined (see Table 6.2); the presence of different sites for Nd^{3+} ions in this crystal is evident from the difference between the expected number of peaks for a single site structure and the actually observed peaks.
To show this, in fig 6.2 the $^4I_{9/2} \rightarrow {}^4F_{5/2} + {}^2H_{9/2}$ transition is reported as an example. For this transition one would expect to observe 8 peaks at low temperature (10K), corresponding to the absorption from the lowest Stark level of the ground state to the 8 Stark sublevels of the excited states. Instead, one can clearly distinguish at least 14 transitions: this is a clear hint that more than one site is present, although their number is not clearly determined by just this measurement.
Observing other transitions at 10 K, both in absorption and emission, and counting the number o peaks, one can conclude that there are at least three different sites (see Table 6.2): in fact for some transitions the observed peaks are more than double those expected for a single-site structure.
Since four sites have been observed in Nd-doped GGG (30), we can suppose that Al doping does not introduce any new site for Nd, or the population of these extra sites is not enough to be detected with our apparatus. In our experimental conditions, it was not possible to perform a complete site-selective analysis and so the energy levels reported in Table 6.2 are not labeled site by site.

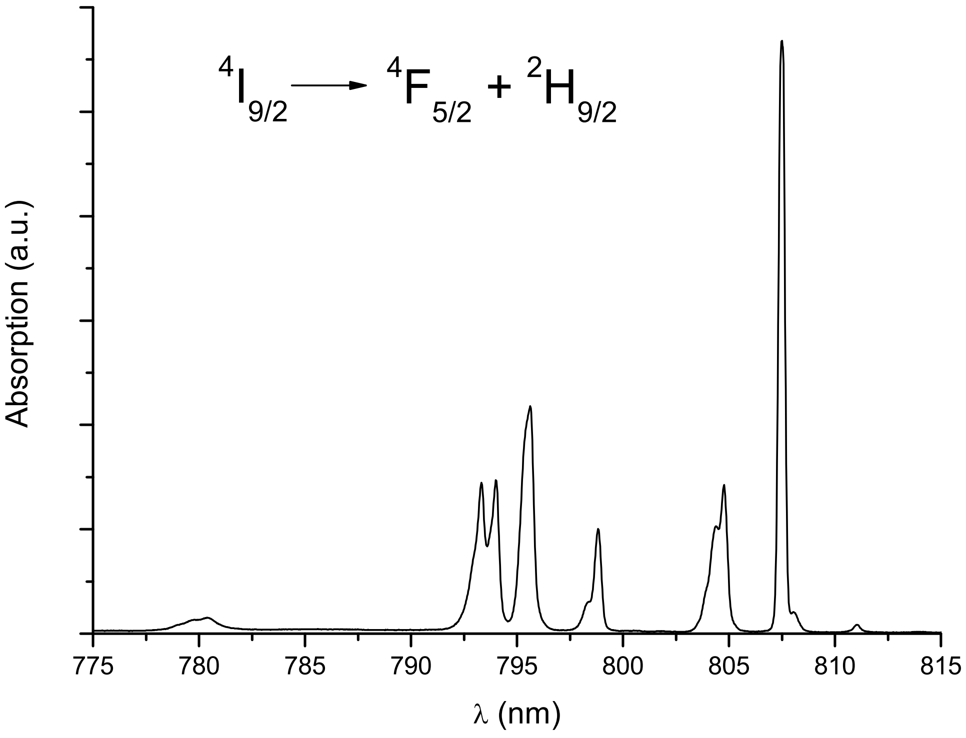

Figure 6.2: Nd:GAGG, 10 K absorption - 10 K absorption spectrum of Nd:GAGG crystal

Table 6.2: Experimentally observed energy levels of Nd^{3+} in GAGG

$^{2S+1}\mathrm{L}_J$	Energy (cm^{-1})	Number of Observed Levels
$^{4}\mathrm{I}_{\frac{15}{2}}$	5767.4, 5769.2, 5772.7, 5822.2, 5825.5, 5829.5, 5918.6, 5930.9, 5943.5, 6509.5, 6526.2, 6559.7, 6566.1, 6579.7, 6666.9, 6682.2	16
$^{4}\mathrm{F}_{\frac{3}{2}}$	11434.7, 11441.8, 11483.9, 11491.1, 11499.0, 11506.2, 11512.9	7
$^{4}\mathrm{F}_{\frac{5}{2}}$	12286.9, 12330.1, 12375.5, 12383.9, 12425.8, 12432.0, 12439.4, 12518.4, 12525.1	9
$^{2}\mathrm{H}_{\frac{9}{2}}$	12568.7, 12573.5, 12594.5, 12605.2, 12611.5, 12814.4, 12824.6, 12834.9	8
$^{4}\mathrm{F}_{\frac{7}{2}} + {}^{4}\mathrm{S}_{\frac{3}{2}}$	13278.9, 13320.5, 13375.2, 13415.6, 13422.4, 13429.1, 13460.8, 13553.8, 13559.3, 13568.5, 13582.3, 13604.1, 13612.9, 13665.9, 13736.7	15
$^{4}\mathrm{F}_{\frac{9}{2}}$	14628.9, 14637.5, 14657.9, 14675.1, 14782.5, 14795.1, 14821.4, 14882.6, 14895.4	9
$^{2}\mathrm{H}_{\frac{11}{2}}$	15664.2, 15708.5, 15764.2, 15803.4, 15839.1, 15849.1, 15873.0, 15883.1, 15956.6, 15987.9, 16086.9, 16091.4	12
$^{4}\mathrm{G}_{\frac{5}{2}}$	16772.2, 16870.5, 16880.5, 16955.6, 16982.3, 17001.7, 17019.8, 17051.8, 17058.3, 17088.2	10
$^{2}\mathrm{G}_{\frac{7}{2}}$	17162.9, 17219.1, 17251.8, 17260.7, 17273.4, 17319.8, 17331.8, 17455.1, 17552.3, 17560.8, 17666.3	11
$^{4}\mathrm{G}_{\frac{7}{2}}$	18654.9, 18752.9, 18763.5, 18836.8, 18851.9, 18863.5, 18985.2, 19091.3	8
$^{2}\mathrm{K}_{\frac{13}{2}} + {}^{4}\mathrm{G}_{\frac{9}{2}}$	19180.9, 19233.5, 19310.6, 19330.2, 19442.9, 19519.8, 19558.9, 19573.3, 19602.1, 19634.8, 19823.6, 19983.0	12
$^{2}\mathrm{G}_{\frac{9}{2}}$	20659.0, 20700.7, 20725.4, 20763.0, 20768.4, 20797.6, 20804.1, 20821.4, 20828.9	9
$^{4}\mathrm{G}_{\frac{11}{2}}$	21008.4, 21057.1, 21065.9, 21108.2, 21123.8, 21174.1, 21186.4	7
$^{2}\mathrm{D}_{\frac{3}{2}} + {}^{2}\mathrm{K}_{\frac{15}{2}}$	21592.4, 21608.8, 21653.2, 21682.6, 21689.6, 21761.6, 21869.9, 21897.4, 21970.8, 22016.7	10
$^{2}\mathrm{P}_{\frac{1}{2}}$	23165.3, 23166.9, 23173.6	3
$^{2}\mathrm{D}_{\frac{5}{2}}$	23706.5, 23717.8, 23755.8, 23762.9, 23788.3	5

The emission from the Nd:GAGG crystal after pumping with a tunable cw Ti-Al_2O_3 laser at low temperature (10 K) emphasizes the presence of the different sites: selective emission spectra were collected after pumping at different wavelengths in the absorption band around 800 nm and the results are shown in fig 6.3 for the $^4F_{3/2} \rightarrow {}^4I_{9/2}$ and $^4F_{32} \rightarrow {}^4I_{11/2}$ transitions. It is quite evident that the three pumping wavelengths correspond to the excitation wavelengths of three different sites because of the shift in the position of the emissions peaks.

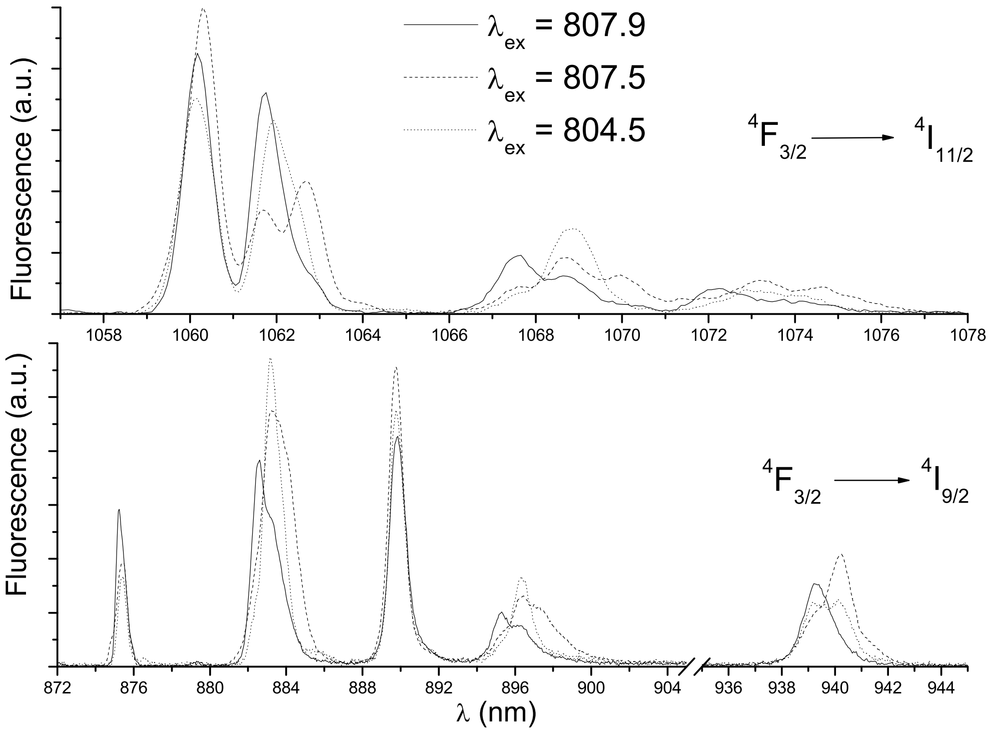

Figure 6.3: Nd:GAGG, 10 K emission - 10 K emission spectra of Nd:GAGG obtained after pumping at different wavelengths in the 808 nm region. The different shapes of the three emission curves indicate the presence of different sites for Nd^{3+} in the garnet host.

The disordered structure of GAGG can be also investigated by excitation spectroscopy. Fig 6.4 shows the spectra obtained observing the $^4F_{3/2} \rightarrow {}^4I_{9/2}$ transition at three different wavelengths (883.2, 882.5, and 884.4 nm) identified in the low-temperature emission measurements (see fig 6.3) and that are supposed to belong to different Nd^{3+} sites. The result shows a distinct behavior of the three observed sites: in particular, the excitation spectrum collected observing the fluorescence at 882.5 nm is the most intense and narrow, while the other two observed spectra are weaker and broader.

For what concerns the measurement of the lifetime of the $^4F_{3/2}$ energy multiplet, we tried to distinguish the different sites, observing the decay of fluorescence at low temperatures at different wavelengths, but without appreciable results: in fact, the different sites are expected to have similar decay times and are so close in energy (only a few cm^{-1}) that, at temperatures above 30 K, they are in thermal contact and then the experimental value of lifetimes is affected by the thermal mixing. The decay curves were all exponential and, from a fit, we could obtain the value τ of the decay time. As expected for our relatively small Nd^{3+} doping level, the temperature dependence of the lifetime of the $^4F_{3/2}$ multiplet is not strong, ranging from 251 μs at 10 K to 231 μs at RT, a typical value for Nd^{3+} in oxide crystals (45).

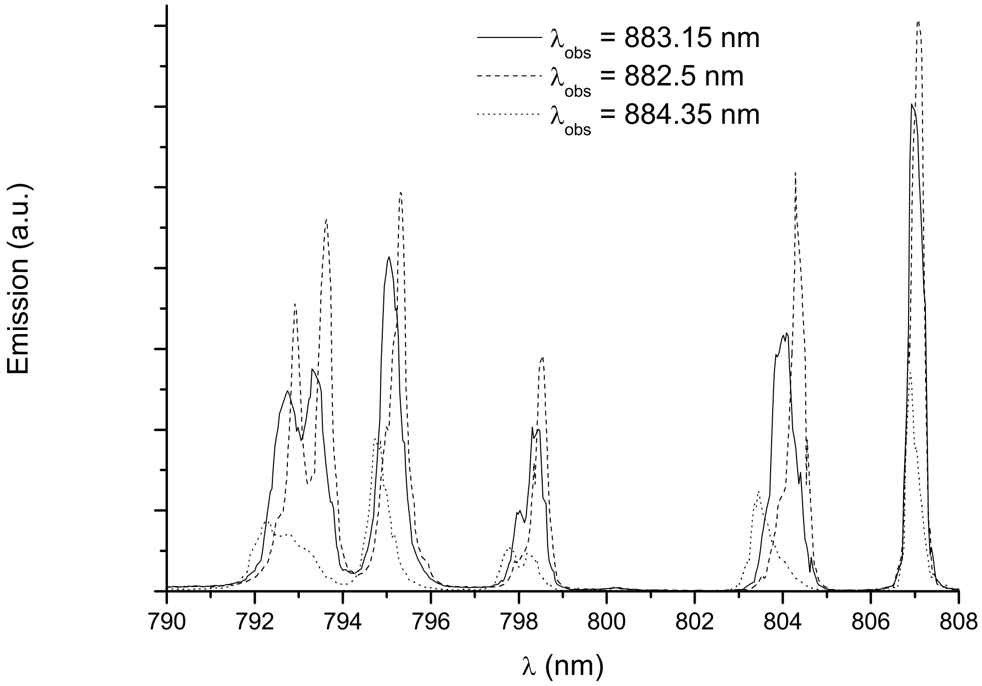

Figure 6.4: Nd:GAGG, excitation spectra. - Excitation spectra of Nd:GAGG crystal. The measurements have been taken observing at three different wavelengths, corresponding to the same transition in different sites for Nd^{3+} ions.

6.3 Judd-Ofelt analysis and laser parameters

The emission spectra at room temperature around 900 nm, 1060 nm and 1300 nm were obtained after diode pumping at 805 nm. From these measurements, all performed in the same experimental conditions, one can evaluate the stimulated emission cross sections (fig 6.5) and the branching ratios for the three main transitions: $^4F_{\frac{3}{2}} \longrightarrow {^4I_{\frac{9}{2}}}$ (β = 30.5%), $^4F_{\frac{3}{2}} \longrightarrow {^4I_{\frac{11}{2}}}$ (β = 55.7%) and $^4F_{\frac{3}{2}} \longrightarrow {^4I_{\frac{13}{2}}}$ (β = 13.8%). The cross sections were calculated according to the Fuchtbauer-Landenburg theory (the integral β-τ method (5)). For this calculation, a value of the refractive index of 1.94 at 1 μm (59) was adopted.

The $^4F_{3/2} \longrightarrow {^4I_{15/2}}$ transition is not reported because it has not been observed, due to its low branching ratio.

In the most relevant wavelength region for laser operation around 1 μm we can find the peak value of σ_{em} = 1.0 x 10^{-19} cm^2 at λ = 1063.5 nm. This is an interesting value if compared with other similar garnet crystals (11) (1). Also the peak at 1068.5 nm (σ_{em} = 5.3 x 10^{-20} cm^2), with a FWHM of 3 nm, is suitable for laser oparation, especially in the mode-locked regime.

The $^4F_{3/2} \longrightarrow {^4I_{9/2}}$ transition shows a broad band composed of 7 peaks from 870 to 900 nm, which is not very interesting for laser operation because of ground state reabsorption, and two more interesting peaks at 935.25 nm (σ_{em} = 1.0 x 10^{-20} cm^2) and 939.25 nm (σ_{em} = 1.3 x 10^{-20} cm^2): with a FWHM of 2.5 nm these two peaks are suitable for water vapour DIAL application, via further compositional tuning for wavelength optimization (95).

Also the $^4F_{3/2} \longrightarrow {^4I_{13/2}}$ transition is reported here: the most intense peak (σ_{em} = 3.1 x 10^{-20} cm^2 at 1333.25 nm) seems to be promising for laser application in the 1.3 μm wavelength region.

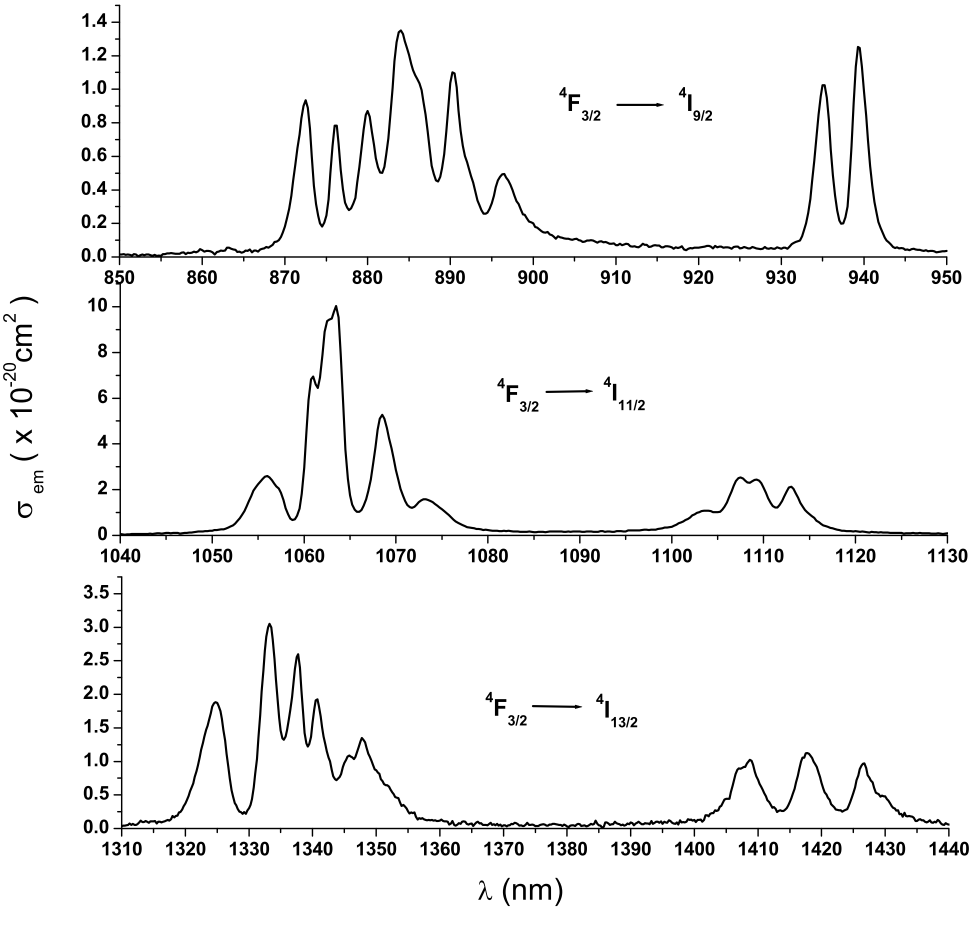

Figure 6.5: Nd:GAGG, RT emission cross sections - Room temperature emission cross sections for Nd:GAGG calculated by the Fuchtbauer-Landeburg equation, for the $^4F_{\frac{3}{2}} \longrightarrow {}^4I_J$ transitions (J = 9/2, 11/2, 13/2)

The RT absorption spectrum was used to perform a Judd-Ofelt analysis (43) (71), using the reduced matrix elements published by Kaminskii (46). In Tab. 6.3 the results including measured and calculated oscillator strengths, the intensity parameters, and the root mean square deviation can be found. The spectroscopic quality parameter $X = \Omega_4/\Omega_6$ is 0.69, and this means that the $^4I_{11/2}$ is the preferential final level for the emission from ^{4}F$_{3/2}$ energy level. Moreover in this case one can find that this X is quite lower than in Nd doped GGG, where it ranges from 0.9 to 1.0 (46). This means that the branching ratio of Nd^{3+} $^4I_{11/2}$ level is greatly improved by doping with Al.

Tab. 6.4 shows the calculated spontaneous emission probabilities, the calculated and experimental radiative branching ratios for the transitions ^{4}F$_{3/2} \rightarrow {}^4$I$_J$ (J = 15/2, 13/2, 11/2 and 9/2), and the radiative lifetime of the emitting level.

The deviation between the calculated lifetime (158 μs) and the measured one (231 μs) can be explained as follows: first, the intrinsic uncertainty (around 30 %) of the Judd-Ofelt method should be the dominant factor; moreover, the effect of radiation trapping can not be completely neglected, especially in crystals having a high refractive index such as GAGG.

Table 6.3: Experimental and calculated oscillator strengths (P) and the Judd-Ofelt parameters of Nd:GAGG are given for the transitions from the ground state (^{4}I$_{9/2}$) to the $^{2S+1}$L$_J$ excited manifolds.

Excited state	Barycenter (cm^{-1})	P$_{exp}$ (10^6)	P$_{calc}$ (10^6)
^{4}F$_{\frac{3}{2}}$	11388	9.85	12.5
^{4}F$_{\frac{5}{2}}$ + ^{2}H$_{\frac{9}{2}}$	12421	43.5	40.1
^{4}F$_{\frac{7}{2}}$ + ^{4}S$_{\frac{3}{2}}$	13405	37.6	40.6
^{4}F$_{\frac{9}{2}}$	14682	3.16	2.83
^{2}H$_{\frac{11}{2}}$ + ^{4}G$_{\frac{5}{2}}$ + ^{2}G$_{\frac{7}{2}}$	17074	33.3	33.6
^{4}G$_{\frac{7}{2}}$ + ^{2}K$_{\frac{13}{2}}$ + ^{4}G$_{\frac{9}{2}}$	19113	20.1	16.6
^{2}G$_{\frac{9}{2}}$ + ^{2}D$_{\frac{3}{2}}$ + ^{4}G$_{\frac{11}{2}}$ + ^{2}K$_{\frac{15}{2}}$	21191	6.35	3.93
^{2}P$_{\frac{1}{2}}$ + ^{2}D$_{\frac{5}{2}}$	23127	1.31	1.61
^{4}D$_{\frac{3}{2}}$ + ^{4}D$_{\frac{5}{2}}$ + ^{2}I$_{\frac{11}{2}}$ + ^{4}D$_{\frac{1}{2}}$	28050	22.5	24.0
$\Omega_2 = 5.04 * 10^{-21} cm^2$	$\Omega_4 = 4.03 * 10^{-20} cm^2$		
$\Omega_6 = 5.89 * 10^{-20} cm^2$	RMS = $2.80 * 10^{-21} cm^2$		%RMS = 14.4

Table 6.4: Calculated spontaneous emission probabilities (A), radiative branching ratio (β) and radiative lifetime (τ_R) for the emission from the $^4F_{3/2}$ level of Nd:GAGG crystal at RT.

Final state	A (s^{-1})	β_{calc}	β_{exp}	τ_R (μs)
$^4I_{\frac{9}{2}}$	$2.39 * 10^3$	0.377	0.305	
$^4I_{\frac{11}{2}}$	$3.23 * 10^3$	0.510	0.557	158
$^4I_{\frac{13}{2}}$	$6.81 * 10^2$	0.108	0.138	
$^4I_{\frac{15}{2}}$	$3.53 * 10^1$	0.006	0	

6.4 Summary

In this chapter complete spectroscopic analysis of the Nd:GAGG laser crystal is reported. The characterization includes absorption and emission at 10 K and RT, temperature-dependent lifetime measurements of the $^4F_{3/2}$ upper laser level, and low-temperature excitation spectroscopy. From the low temperature measurements, three different centers for Nd^{3+} ions are identified.

The JuddOfelt analysis shows the promising features of this crystal as a laser crystal. From RT emission and from lifetime measurements, the emission cross sections have been calculated via the Fuchtbauer-Landenburg formula for the $^4F_{3/2} \rightarrow {}^4I_J$ transitions (J = 9/2, 11/2, 13/2). The results show the possibility to obtain laser emission from this crystal in both cw and modelocking regimes in the 1 and 1.3 μm wavelength regions. Then, two broad emission peaks around 940 nm have been observed, suggesting a possible application for water vapor DIAL applications via further compositional tuning for emission wavelength optimization.

In chapter 8 I will show that these characteristics are emphasized in the laser operation in both cw and mode-locked regime.

Chapter 7

Nd : LGGG

In this chapter another derivative of Nd:GGG crystal, $(Lu_x{+}Gd_{1-x})_3Ga_5O_{12}$, is reported. The samples (with x = 0.1 in the melt, abbreviated as Nd:LGGG below) with good optical quality have been grown successfully by Czochralski (Cz) method, and elementary optical properties and both cw and pulsed laser results have been published during the time of my PhD (3, 42). Here a detailed spectroscopic analysis, required to characterize this material, is shown.

In this chapter I report a complete optical investigation of Nd^{3+} doped $(Lu_x{+}Gd_{1-x})_3Ga_5O_{12}$ crystal, including absorption and emission spectroscopy at room temperature and 10 K, excitation spectroscopy at 10 K showing the multi-sites features, and lifetimes at temperatures from 10 K to 300 K. The Judd-Ofelt theory has been applied to calculate the spontaneous transition probabilities, the branching ratio, and the radiative lifetime of the $^4F_{3/2}$ multiplet; the calculated results are in good agreement with the experimental ones. Finally, the emission cross-sections for different transitions are reported, showing the potentials of this material for laser applications.

7.1 Crystal growth

A Nd:LGGG sample with good optical quality was grown by the RF-heating Cz method at State Key Laboratory of Crystal Materials, Shandong University, China, and the details of the growth process can be found in ref. (42). To check the structure of the crystal, X-ray powder diffraction measurement was performed. The obtained crystal has the same cubic structure ofh $Gd_3Ga_5O_{12}$ (GGG), except for a small difference of lattice parameter (42). The doping level of Nd^{3+} in the sample is 0.53 at.%, and the Lu concentration is 13.6 at %: these were measured by X-ray fluorescence method from the first part of the as-grown Cz boule. The concentration of Lu in the crystal is expected to be almost constant, even if the segregation coefficient is different from 1, because the Cz boule has a very little mass (78 g) with respect to the raw materials (452 g). Moreover, the sample used for the measurements was cut from the first part of the boule, where the concentration has been measured.

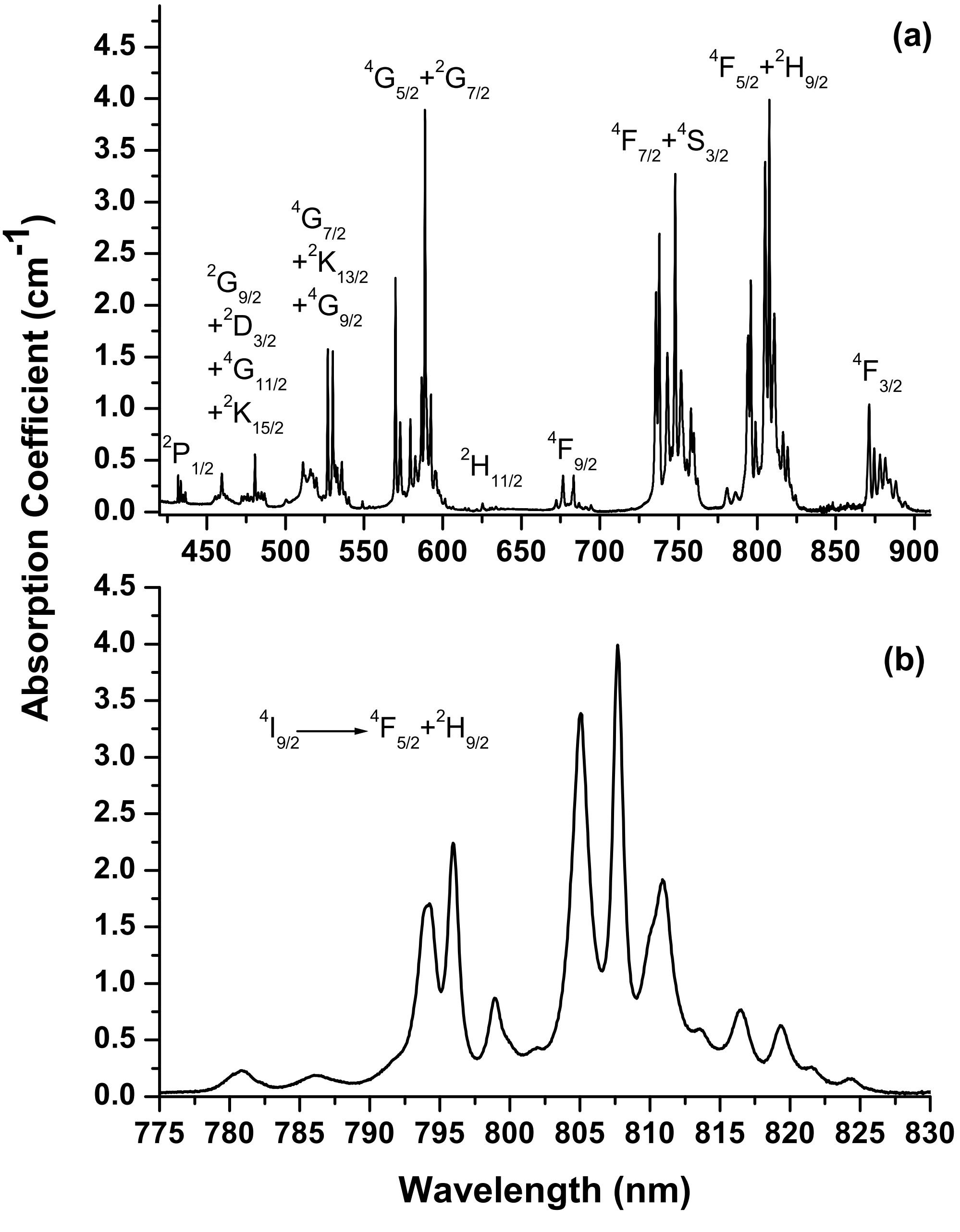

Figure 7.1: Nd:LGGG, room temperature absorption. - Room temperature absorption spectroscopy in visible and NIR range (a), and the particular of absorption around 800 nm of $^4I_{9/2}{\longrightarrow}^4F_{5/2}{+}^2H_{9/2}$ transition (b)

7.2 Spectroscopic analysis

The absorption spectrum of Nd:LGGG crystal at RT is shown in fig 7.1(a), and all the peaks labeled according to the expected positions found in (46) can be ascribed to Nd^{3+}: this confirms the high purity of the sample.

The broad absorption band around 800 nm ranges from 778 nm to 825 nm, as shown in fig 7.1(b). Concerning the most interesting band for diode pumping around 808 nm, there are two intense peaks at 805.0 nm and 807.7 nm with FWHM of about 1.55 nm and 0.95 nm respectively, comparable with the absorption peaks in Nd:YAG (13).

A detailed study of the absorption and emission peaks at 10K is required in order to evaluate the postion of the energy Stark sublevels in the matrix: this work is required everytime one has to deal with new crystal compositions, as in this case. Fig 7.2(a) shows the absorption spectra at 10 K, performed with a resolution of 0.06 nm. For clarity and for comparison with the excitation spectra shown later in this section, I report only the part from 775 to 810 nm. In table 7.1 the energy levels of Nd^{3+} in LGGG crystal, obtained from 10 K emission (for $^4I_{9/2}$ and $^4I_{11/2}$ levels) and absorption (for others) spectra, are given. The table shows that for most of the $^{2S+1}L_J$ manifolds the experimental number of levels is larger than the one expected for a single-site matrix, but less than two times. It is important to notice that a site-selective analysis is needed to label each site, while in tab 7.1 only the detected level positions have been indicated. Fig 7.2(b) shows the absorption band relative to the $^4I_{9/2} \longrightarrow {}^4F_{3/2}$ transition at 10 K to clarify this multi-site feature: here four peaks can be clearly distinguished, instead of the two that one would expect, so there should be at least two different kinds of sites occupied by Nd^{3+} ions in LGGG. This multisite structure has been observed also in Nd doped GGG, where four different sites are present (31), and in the previous chapter (6) the same analysis showed the presence of three distinct sites. From fig 7.2(b) (and from lifetime measurements) we can guess that the two sites have a very similar symmetry; a possible kind of center could be a Nd ion on the dodecahedral site with a Lu ion at the neighbouring octahedral site (antisite position (64)). This suggests that the partial replacement of Gd^{3+} by Lu^{3+} does not bring new Nd^{3+} sites in the host crystal, or at least the other sites are not populated significantly and can be neglected in a laser-oriented analysis.

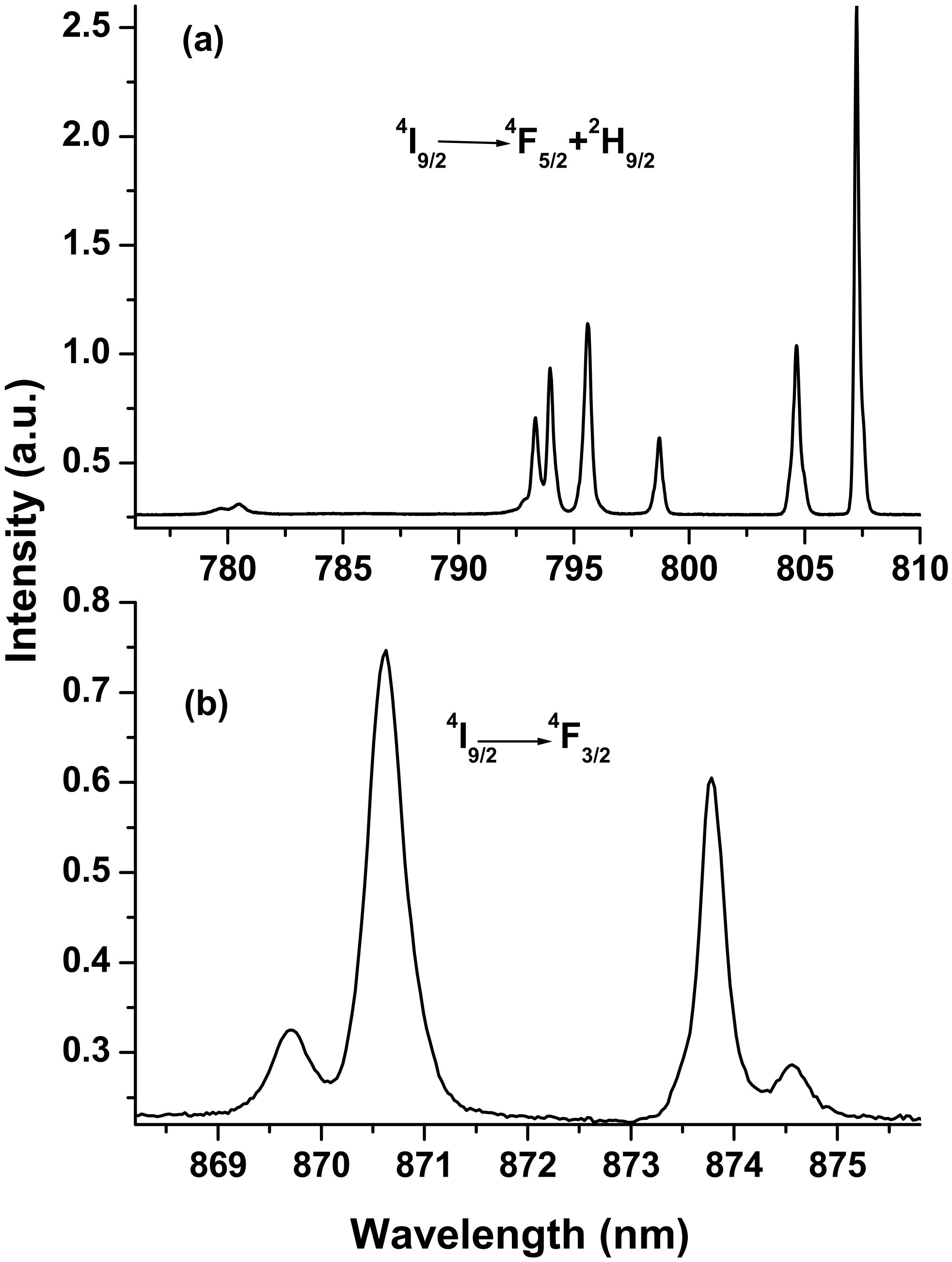

Figure 7.2: Nd:LGGG, 10 K absorption. - Absorption spectra at 10 K of Nd:LGGG crystal for two transitions: $^4I_{9/2}\longrightarrow{}^4F_{5/2}+{}^2H_{9/2}$ (a) and $^4I_{9/2}\longrightarrow{}^4F_{3/2}$ (b)

Table 7.1: Experimentally observed energy levels of Nd^{3+} in LGGG

$^{2S+1}L_J$	Energy (cm^{-1})	Number of Observed Levels
$^4I_{\frac{9}{2}}$	0, 11.0, 93.8, 116.3, 188.1, 255.4, 281.3, 786.7	8
$^4I_{\frac{11}{2}}$	1989.8, 2004.2, 2016.7, 2050.2, 2058.7, 2079.5, 2096.5, -*	7
$^4I_{\frac{13}{2}}$	3918.8, 3922.2, 3925.9, 3983.1, 3993.9, 4007.7, 4025.7, 4370.2, 4385.2, 4414.2	10
$^4I_{\frac{15}{2}}$	5770.3, 5818.7, 5822.8, 5892.8, 5915.1, 5933.3, 5954.5, 6496.9, 6518.9, 6560.8, 6665.8	11
$^4F_{\frac{3}{2}}$	11434.6, 11444.3, 11486.1, 11497.9	4
$^4F_{\frac{5}{2}}$	12382.9, 12387.6, 12422.9, 12427.9,12520.3	5
$^2H_{\frac{9}{2}}$	12569.1, 12591.6, 12594.8, 12604.9, 12612.9, 12812.3, 12824.8	7
$^4F_{\frac{7}{2}} + {}^4S_{\frac{3}{2}}$	13372.2, 13377.6, 13418.1, 13556.0, 13561.2, 13568.2, 13575.9, 13602.9, 13610.6, 13662.7	10
$^4F_{\frac{9}{2}}$	14635.3, 14642.1, 14645.1, 14658.9, 14667.5, 14783.3, 14822.3, 14881.4, 14899.1	9
$^2H_{\frac{11}{2}}$	15760.4, 15841.8, 15846.4, 15875.5, 15880.6, 15952.2, 15955.6, 16082.9, 16085.9, 16092.7, 16104.6	11
$^4G_{\frac{5}{2}}$	16878.8, 16988.9, 17055.5	3
$^2G_{\frac{7}{2}}$	17257.4, 17265.2, 17320.2, 17393.7, 17466.6, 17553.1	6
$^4G_{\frac{7}{2}}$	18763.8, 18841.6, 18869.3, 18988.3	4
$^2K_{\frac{13}{2}} + {}^4G_{\frac{9}{2}}$	19176.9, 19190.9, 19213.0, 19313.9, 19335.6, 19451.5, 19527.4, 19564.1, 19580.2, 19603.2, 19632.5, 19832.6, 19977.6	13
$^2G_{\frac{9}{2}}$	20716.8, 20771.9, 20805.6, 20812.5, 20829.0	5
$^4G_{\frac{11}{2}}$	21015.5, 21061.5, 21114.0, 21182.8, 21190.9	5
$^2D_{\frac{3}{2}} + {}^2K_{\frac{15}{2}}$	21506.3, 21602.0, 21614.1, 21694.8, 21750.5, 21767.5, 21871.3, 21957.8	8
$^2P_{\frac{1}{2}}$	23170.7, 23173.9	2
$^2D_{\frac{5}{2}}$	23722.5, 23760.9, 23790.3	3

*The data corresponding to the bands around 2407 cm^{-1} and 243 cm^{-1} (according to (46)) have not been collected

In fig 7.3 one can see the site-selective excitation spectrum at 10 K, from 778 to 810 nm, corresponding to the $^4I_{9/2}\longrightarrow{}^4F_{5/2}+{}^2H_{9/2}$ transition. The emission intensity is corrected for the corresponding incident power. Two fixed wavelengths are monitored here: 884.01 nm and 882.17 nm. These are expected to correspond to the emission from the same Stark sub-level of $^4F_{3/2}$, but from two different Nd^{3+} sites. These wavelengths were chosen because the energy difference between the two Nd^{3+} observed ”‘species”’ for this transition is quite large (about 23 cm^{-1}) and the fluorescence is intense, as can be found from 10 K emission spectroscopy reported in fig 7.4. One can clearly notice that both excitation spectra have similar shape, compared to the absorption spectrum at 10 K, as shown in fig 7.2(a), while the position and the intensity of the peaks clearly depend on which site has been excited. This confirms that there are at least two different Nd^{3+} sites in LGGG host crystal, as was deduced from the 10 K absorption spectroscopy.

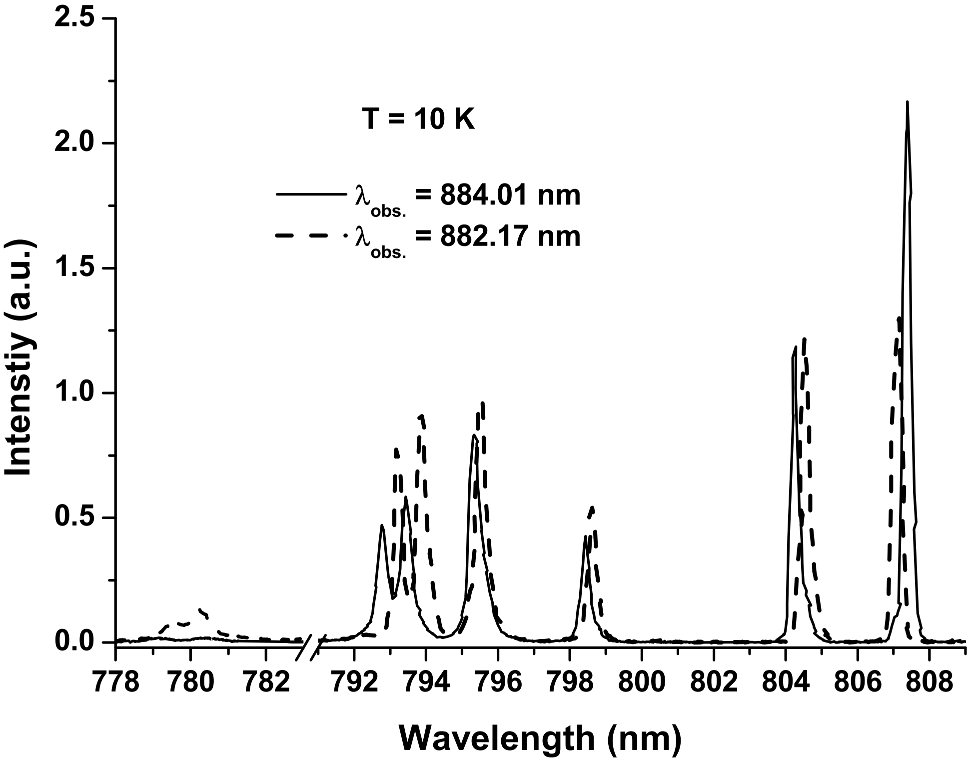

Figure 7.3: Nd:LGGG, site-selective excitation. - Site-selective excitation spectroscopy at 10 K of the $^4F_{3/2} \longrightarrow {}^4I_{9/2}$ transition at two different observed wavelengths: 884.0 nm and 882.2 nm

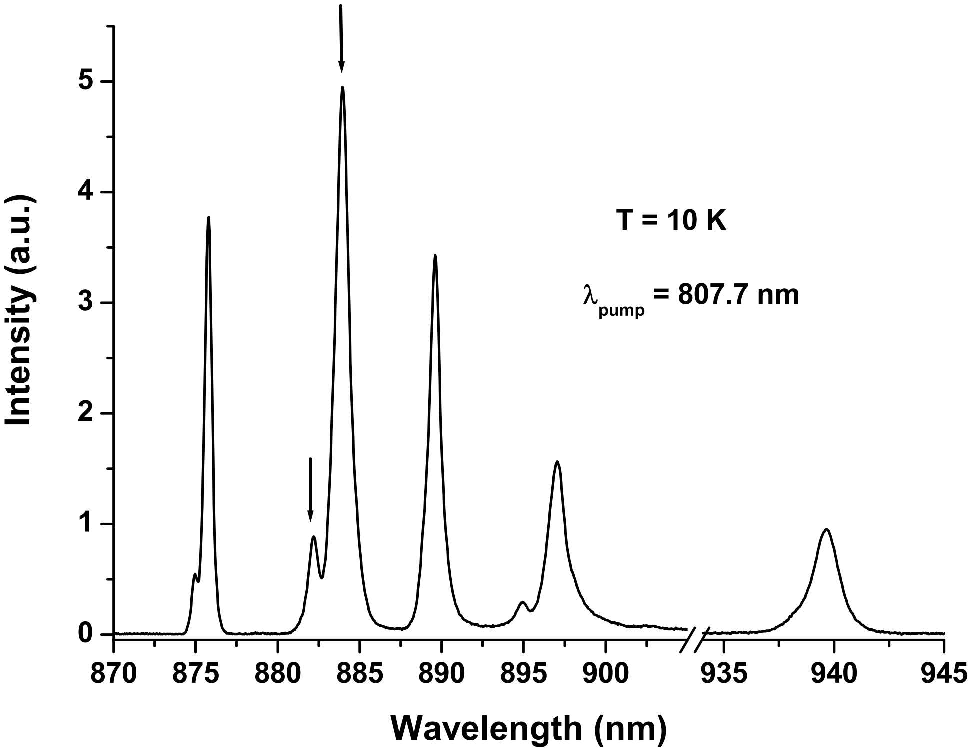

Figure 7.4: Nd:LGGG, $^4F_{3/2}\longrightarrow{}^4I_{9/2}$ transition at 10 K. - Emission spectroscopy of $^4F_{3/2}\longrightarrow{}^4I_{9/2}$ transition at 10 K. The two arrows show the observed wavelengths in excitation spectroscopy

Fluorescence spectra of Nd:LGGG at RT in the regions of the $^4F_{3/2}\longrightarrow{}^4I_{9/2}$, $^4I_{11/2}$ and $^4I_{13/2}$ transitions have been measured, separately but with the same resolution of 0.15 nm: there are three main laser channels, centred at around 940, 1060, and 1330 nm, corresponding to the $^4F_{3/2}\longrightarrow{}^4I_{9/2}$, $^4F_{3/2}\longrightarrow{}^4I_{11/2}$, and $^4F_{3/2}\longrightarrow{}^4I_{13/2}$ transitions, respectively. To check if some information about the multi-site nature of the tested crystal was detectable also at room temperature, an idea was to try to collect fluorescence spectra after pumping the sample at room temperature with different wavelengths: 798.9 nm, 805.1 nm, 807.8 nm, and 811.1 nm. The four emission spectra that were obtained are almost identical,in this case meaning that the different sites can not be distinguished because of the thermal broadening of the absorption bands.
In fig 7.4 the fluorescence spectroscopy of $^4F_{3/2}\longrightarrow{}^4I_{9/2}$ transition at 10 K after pumping at 807.7 nm is shown for comparison. The ground multiplet is characterized by an overall splitting of 787 cm^{-1}. The peaks at 889.6 and 939.6 nm appear unique, and the peaks at around 875 nm, 883 nm, and 896 nm are all split into two lines separated by 11, 23, and 26 cm^{-1}, respectively, due to the presence of two Nd^{3+} "‘species"’.

7.2.1 Decay time kinetics

A time-resolved fluorescence study at different temperatures from 10 K to 300 K was also performed. At 10 K we tried to discriminate two different sites by observing the decay-time of two different peaks separately (at 882.2 nm and 884.0 nm). It was found that both Nd^{3+} decays were exponential and their decay-time are nearly identical, with values of 261 μs and 258 μs (error: 1 μs), respectively. This suggests that the two kinds of Nd^{3+} sites in LGGG host material have a similar surrounding crystal-field. Since at higher temperature the Stark sublevels are thermally coupled , it is meaningless to perform site selective measurements beyond 10 K. For this reason, the decay-time measurements as a function of the temperature have been performed by observing a broad emission window. As observed in other similar Nd^{3+} doped garnet crystals (1) and also in Nd:GAGG (see chapter 6), the dependence of the decay time on temperature from 10 K to 300 K is not strong: in fact the value at room temperature was 246 μs, about 5 % less than the one at 10 K (260 μs).

7.3 Judd-Ofelt analysis and laser parameters

The Judd-Ofelt analysis (43, 71) was performed from the absorption spectroscopy at RT, where the eight bands shown in table 7.2 were considered for calculating the intensity parameters. As a value for the refractive index, the value in GGG ($n = 1.94$) was adopted, and the reduced matrix elements were found in (46).

In table 7.2 the results of the analysis, can be found. The Ω_2 parameter here presents a low value, but this has no practical effect on the emission from Nd^{3+} $^4F_{3/2}$ state (46). It is worth to notice that the Ω_4 is much smaller than Ω_6 for Nd^{3+} in LGGG crystal, whereas Ω_4 has nearly the same value of Ω_6 in GGG crystal (46, 55, 62). This is interesting because the spectroscopic quality parameter, defined as $X = \Omega_4/\Omega_6$ for Nd^{3+}, turns out to be about 0.76 in LGGG, smaller than the criteria (0.984) for Nd^{3+} doped laser crystals (62), and is between those of Nd:YAG and Nd:GGG crystals, as shown in table 7.3. This means that the Nd^{3+} $^4I_{11/2}$ level becomes a more preferential level for the emission from $^4F_{3/2}$ energy level than in GGG.

The calculated spontaneous emission probabilities, branching ratio of $^4F_{3/2} \longrightarrow {}^4I_J$ ($J = 9/2, 11/2, 13/2$, and $15/2$) transitions, and radiative lifetimes are shown in table 7.4 together with the experimental branching ratio obtained from the emission spectra. Considering the intrinsic error of Judd-Ofelt method (30%), the calculated lifetime and branching ratios are in good agreement with the experimental data. This fact, together with the exponential shape of the decay-time profile, indicates that non-radiative processes are not very effective in this crystal, at least at this doping concentration.

Excited state	Barycenter (cm^{-1})	P_{exp} (10^6)	P_{calc} (10^6)
$^4F_{\frac{3}{2}}$	11371	6.08	9.25
$^4F_{\frac{5}{2}} + {}^2H_{\frac{9}{2}}$	12422	30	28.3
$^4F_{\frac{7}{2}} + {}^4S_{\frac{3}{2}}$	13410	26.6	28.1
$^4F_{\frac{9}{2}}$	14684	2.03	1.97
$^2H_{\frac{11}{2}} + {}^4G_{\frac{5}{2}} + {}^2G_{\frac{7}{2}}$	17099	21.9	22.0
$^4G_{\frac{7}{2}} + {}^2K_{\frac{13}{2}} + {}^4G_{\frac{9}{2}}$	19099	13.7	11.9
$^2G_{\frac{9}{2}} + {}^2D_{\frac{3}{2}} + {}^4G_{\frac{11}{2}} + {}^2K_{\frac{15}{2}}$	21195	4.44	2.93
$^2P_{\frac{1}{2}}$	23052	0.59	1.12
$\Omega_2 = 6.39 * 10^{-22} cm^2$	$\Omega_4 = 3.06 * 10^{-20} cm^2$		
$\Omega_6 = 4.05 * 10^{-20} cm^2$	RMS $= 2.1 * 10^{-21} cm^2$		%RMS = 15.8

Table 7.2: Experimental and calculated oscillator strengths (P), Judd-Ofelt parameters (Ω_t) of Nd:LGGG

Material	Ω_t (10^{-20} cm^2)			X	Ref
	t = 2	t = 4	t = 6		
Nd:YAG	0.2	2.7	5.0	0.54	(12)
Nd:GGG	0.02	6.7	6.7	1	(46)
	0	3.3	3.7	0.89	(12)
Nd:LGGG	0.094	3.1	4.1	0.76	This work

Table 7.3: Judd-Ofelt parameters (Ω_t) and spectroscopic quality parameter (X) of Nd doped YAG, GGG and LGGG crystals

Final state	A (s^{-1})	β_{calc}	β_{exp}	τ_R (μs)	τ_{exp} (μs)
$^4I_{\frac{9}{2}}$	1760.5	0.391	0.299		
$^4I_{\frac{11}{2}}$	2249.2	0.500	0.545	222	246
$^4I_{\frac{13}{2}}$	465.9	0.104	0.156		
$^4I_{\frac{15}{2}}$	24.1	0.005			

Table 7.4: Calculated spontaneous-emission probabilities (A), radiative branching ratio (β) and radiative lifetime (τ_R) for the emission from the $^4F_{3/2}$ level of Nd:GAGG crystal at RT. The experimental values of β and τ are given for comparison.

The stimulated emission cross sections (σ_{em}) of $^4F_{3/2} \longrightarrow ^4I_J$ (J = 9/2, 11/2, and 13/2) transitions at RT calculated by the β-τ method (5) are reported in fig 7.5. Here, the σ_{em} of $^4F_{3/2} \longrightarrow ^4I_{15/2}$ transition is not included because of its low branching ratio and indeed has not been observed experimentally (1, 46). The $^4F_{3/2} \longrightarrow ^4I_{9/2}$ transition consists of two wavelength regions: a broad one composed by 7 well resolved peaks between 870 nm and 900 nm and an intense one composed by two peaks between 930 and 940 nm. The first band has a peak value of 1.2 x 10^{-20} cm^2 at 872.7 nm, but it is not interesting for the laser application because of large ground state re-absorption. The second band is composed of two peaks at 934.5 and 938.3 nm. The values of σ_{em} and FWHM at 938.3 nm are 1.17 x 10^{-20} cm^2 and 20.8 cm^{-1}, respectively. Although the σ_{em} of our sample is about one third of that of Nd:YAG, the FWHM is about 5 times larger (91). So Nd:LGGG crystal presents good characteristics as a possible laser material for water vapour DIAL applications.

The most important transition of Nd^{3+} for laser application is the $^4F_{3/2} \longrightarrow ^4I_{11/2}$ transition, which includes two regions around 1.06 and 1.15 μm. The first broad region ranges from 1050 to 1075 nm, with three intense peaks at around 1.06 μm. The peak values of the emission cross-section are 7.1, 7.4, and 10.6 x 10^{-20} cm^2 at 1060.2, 1061.7, and 1063.2 nm respectively, comparable to those of other garnet crystals, as shown in table 7.5. The emission around 1.06 μm is very broad in this crystal, so it should be possible to develop tunable solid state lasers in this region, opening interesting perspectives for second harmonic generation (47, 79). Also the σ_{em} of $^4F_{3/2} \longrightarrow ^4I_{13/2}$ transition is reported, consisting of two bands around 1.33 μm and 1.42 μm. It is remarkable that the band centered at 1.33 μm is broad, and has a maximum peak value of 3.7 x 10^{-20} cm^2 at 1332 nm. So, Nd:LGGG is a promising candidate for laser operation also in 1.3 μm region.

Table 7.5: Emission cross sections around 1.06 μm for several Nd-doped garnet crystals.

Material	λ(nm)	σ_{em} (x 10^{-19} cm^2)	Ref
LGGG	1063.2	1.1	This work
YAG	1064.2	3.3	(47)
GGG	1062.1	2.9	(47, 79)
CNGG	1067.0	0.54	(1)
YSAG	1062.2	0.90	(4)
CaSGG	1060.0	0.26	(12)

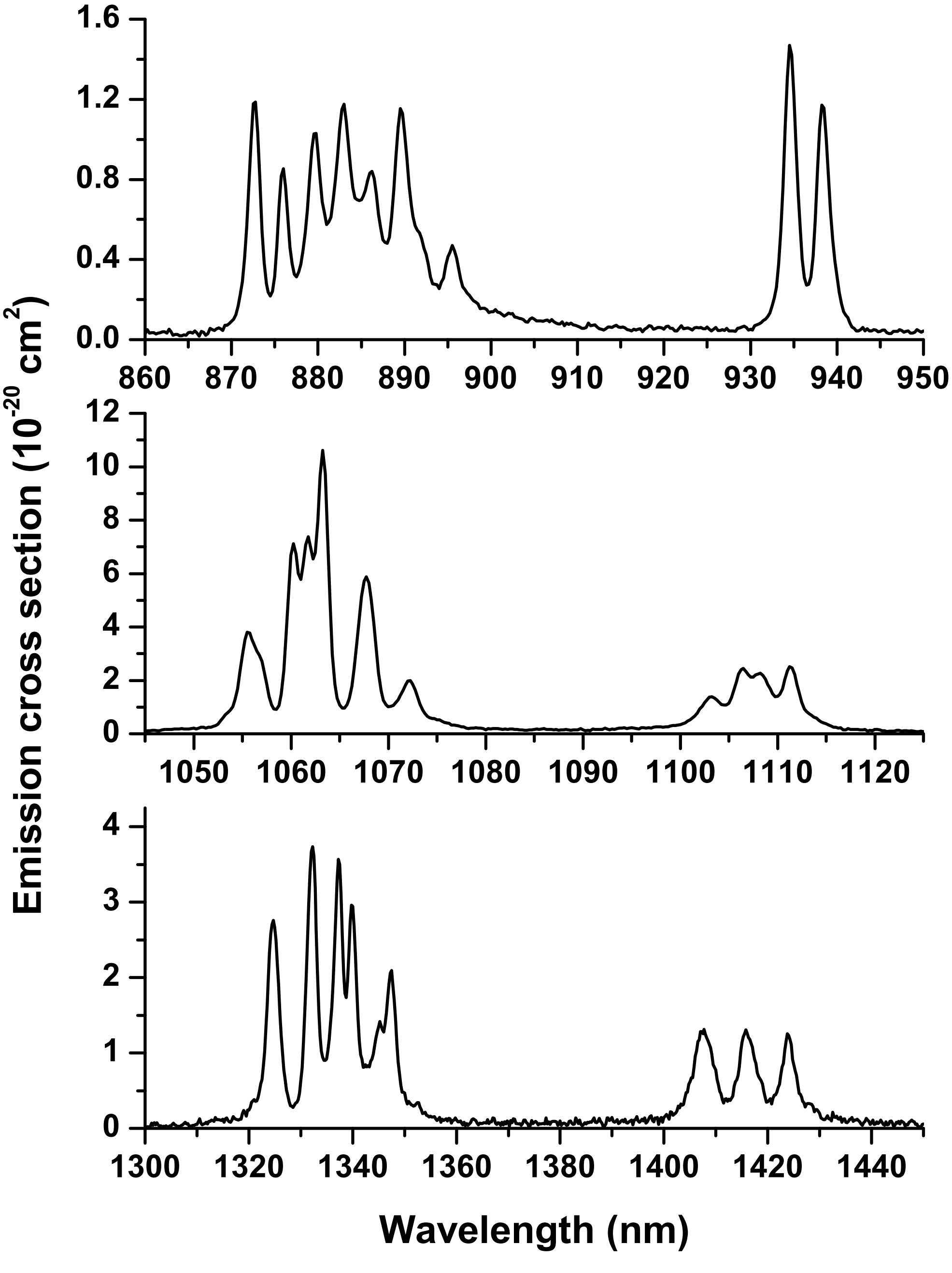

Figure 7.5: - Room temperature stimulated emission cross section for the $^4F_{3/2}\longrightarrow{}^4I_J$ (J = 9/2, 11/2, and 13/2) transitions

7.4 Summary

A complete spectroscopic characterization, including absorption and emission spectroscopy at 10 K and RT, excitation spectroscopy at 10 K, temperature dependence of the lifetime, and Judd-Ofelt analysis, has been shown in this chapter. From these results the evidence of at least two different Nd^{3+} sites in this matrix is described, and from decay time measurements at 10 K it's hinted that the crystal fields at the two different Nd^{3+} sites are similar.

The Judd-Ofelt theory has been applied to calculate the branching ratios and lifetimes, which result in good agreement with the experimental data. In addition, the emission cross sections of $^4F_{3/2} \longrightarrow {}^4I_J$ (J = 9/2, 11/2, and 13/2) transitions at RT are also given, showing promising laser channels centered around 940 nm, 1063 nm and 1332 nm.

Chapter 8

Laser results with Nd:LGGG and Nd:GAGG

In this chapter I will summarize the main results that were obtained with the Garnet crystals that were investigated in my thesis. The laser experiments were carried out at the Department of Electronics, University of Pavia.

First I will present the resuts obtained with Nd:LGGG, in which a peculiar effect due to its multisite structure is shown. Then, I will present the experiments performed on Nd:GAGG.

The crystals were tested in both CW and mode-locked operation and show multiple-wavelength emission, particularly suitable for THz radiation generation via frequency-difference, once the radiation is amplified and combined in non-linear media. I will show that, despite the broad emission bands at room temperature, sub-ps operation is not achieved for these disordered Nd-doped garnet crystals.

In fig 8.1 the room temperature characteristics of the two samples are summarized for a more convenient consultation of this chapter; for the complete spectroscopic investigation of the two crystals, the reader may refer to chapter 6 and 7.

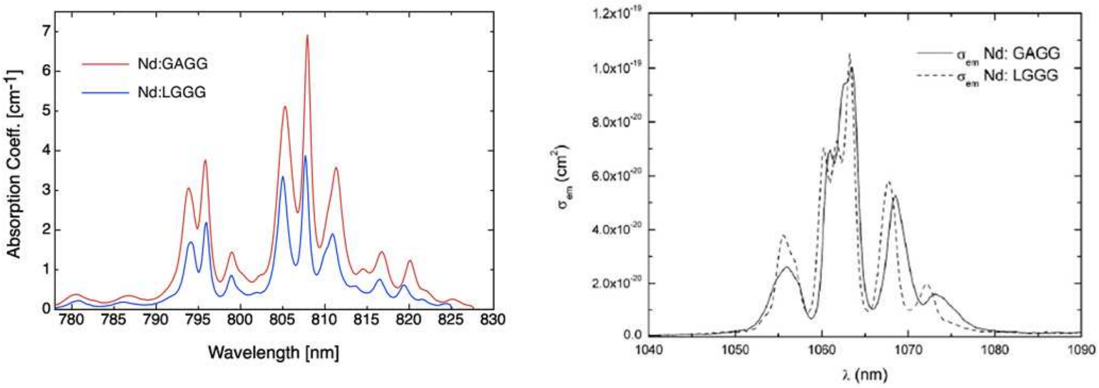

Figure 8.1: - Room temperature absorption and emission properties of of Nd:GAGG and Nd:LGGG crystals

8.1 Experimental setup for laser experiments

8.1.1 Continuous wave operation setup

In fig 8.2 the resonator for CW laser experiments on both samples is shown. The pump source used for both CW and mode-locked operation was a 50 x 1 μm^2 high brightness laser diode operating at the central wavelength of 808 nm with the maximum output power of 1 W. This was chosen to match the strong absorption lines in our samples as much as possible. The pump scheme is shown in fig 8.3: the diode beam was collimated by an 8 mm focal length aspheric lens (L1), shaped by a cilindrical telescope (C1, C2) and finally focused by an 80 mm length achromat (L2). After this, the spot size (in air, measured with a CCD camera) was W$_x$ x W$_y$ = 21 x 11 μm^2 along the slow and fast axis, respectively (see fig 8.3). The distance between the mirrors were: M1 - M2 = 107 mm, M2 - M3 = 350 mm, M1 - OC1= 340 mm. The waist radius of the cavity was 70 x 37 μm^2.

The crystals were placed in the cavity at Brewster angle in order to minimize the losses.

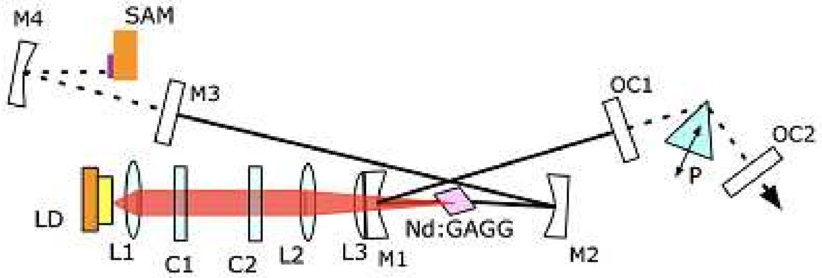

Figure 8.2: Laser setup, resonator. - Resonator layout. PD: pump laser diode; L1: aspheric lens; L2: achromatic lens; L3: spherical lens; C1, C2: cylindrical lenses (15 x telescope); M1, M2: concave mirrors, 100-mm curvature, HR at 1064 nm, high transmissivity at 800 810 nm; M3: HR flat mirror for cw experiments; M4: concave mirror, HR with 75-mm radius of curvature; P: SF10 Brewster-cut prism; OC1: 30 wedge output coupler mirror for cw experiments cavity; OC2: 30 wedge output coupler mirror for cw-modelocking experiments cavity.

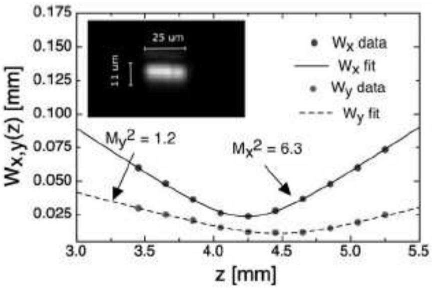

Figure 8.3: Laser setup, pump beam. - Pump beam spot and divergence measured with the setup shown in fig 8.4

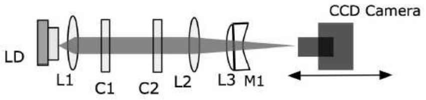

Figure 8.4: Laser setup, pump shaping optics. - Pump shaping optics used for CW and mode-locked operation. PD: pump laser diode; L1: aspheric lens; L2: achromatic lens; C1, C2: cylindrical lenses (15 x telescope)

8.1.2 Mode-Locking operation setup

The setup used for mode-locking operation was obtained from the CW setup replacing the plane M3 mirror (see fig 8.2) by a 75 mm - radius focusing mirror (M4) and a semiconductor Saturable Absorber Mirror (SAM) with either 1% or 2% nominal absorption (from *BAOTP GmbH*).

In this case the distances between the mirrors were set to M1 - M2 = 107 mm, M2 - M4 = 350 mm, M1 - OC2= 340 mm, M4 - SAM = 36 mm.

A single-prism setup for dispersion compensation was used in these experiments: this geometry allows straightforward central output wavelength selection by proper horizontal alignment of the OC (54). The effect of the SF10 Brewster prism, placed at 240 mm from M1 mirror, is equivalent to that of a pair of SF10 prisms separated by 60 cm.

8.2 Laser operation of Nd:LGGG

8.2.1 Continuous wave operation

A 4.5 mm long Nd-doped LGGG crystal ([Nd] = 0.67 x 10^{20} ions/cm^3) was placed at Brewster angle in the cavity to minimize losses, without any active cooling system. The highest slope efficiency (61%) was obtained with an output coupler of transmittivity T_{OC} = 10%. A slighty lower slope efficiency with the maximum otput power of 230 mW was instead obtained with a T_{OC} = 5% output coupler. The results are summarized in fig 8.5. It is worth to notice that the absorbed pump power was limited to 400 mW due to the slight mismatch between pump and absorption lines.

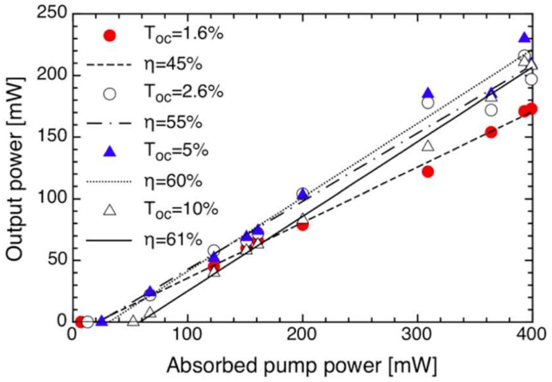

Figure 8.5: Nd:LGGG, cw laser slopes. - Performance of Nd:LGGG in cw operation, with several output couplers.

8.2.2 Mode - locking operation

For the mode-locked operation output couplers with low transmittivity were used, in order to reduce the critical pulse energy required for the stabilization of the mode-locking.

For this sample three different operating regimes were observed: single wavelength, double wavelength and triple wavelength.

In the single wavelength regime pulses of $\tau = 9.1$ ps fwhm were obtained, with a $\Delta\lambda$ of 0.16 nm, at 1062.2 nm. In this case the pulses are nearly Fourier limited ($\Delta\tau$ x $\Delta\lambda$ = 0.39).

In the dual wavelength operating regime two synchronized pulses at 1066.6 nm and 1067.1 nm were simultaneously running in the cavity with a measured pulse duration of about 6.3 ps fwhm. In fig 8.6 the two wavelengths are modeled with Gaussian peaks (S_1 and S_2): using this model the calculated autocorrelation results in good agreement with the experimental measurement (see fig 8.7), apart for a slight discrepancy, supposed to be due to the fact that the two peaks are not perfectly Fourier limited (by a factor 1.2). As shown in fig 8.8 the mode locking is stable and no timing jitter is observed.

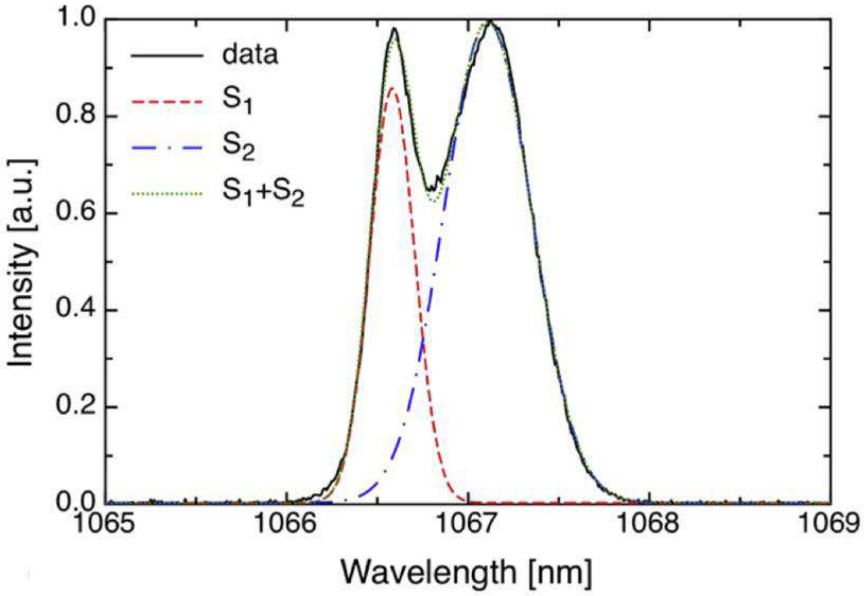

Figure 8.6: Nd:LGGG, mode-locked spectrum. - Spectrum decomposition of mode-locking pulses at two wavelengths (1066.6 and 1067.1 nm)

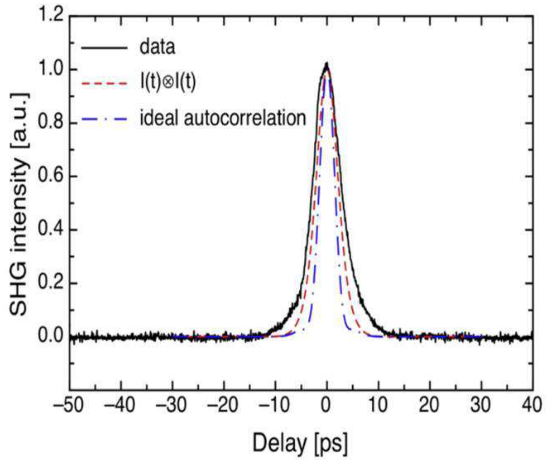

Figure 8.7: Nd:LGGG, autocorrelation spectrum. - Non-collinear second-harmonic autocorrelation in dual-wavelength regime. Also shown are the autocorrelation curve corresponding to the total intensity I(t) = I_1(t)+I_2(t) of Fourier limited pulses with spectral density S_1 and S_2, with τ = 5.6 ps and 3.0 ps (fwhm), and the ideal autocorrelation trace corresponding to the whole spectrum supposed to be perfectly phase-locked

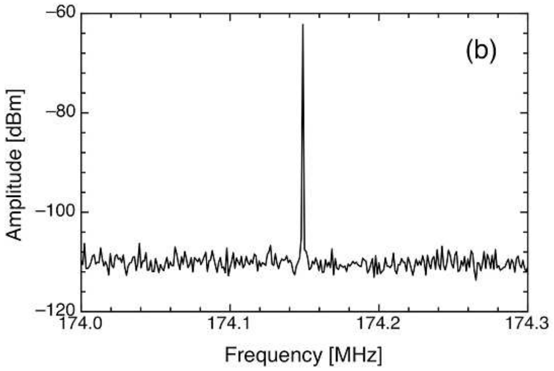

Figure 8.8: Nd:LGGG, RF spectrum. - RF spectrum (measured by a 3-GHz *Agilent N9320B* analyzer) of the two-wavelength mode-locking regime

This dual wavelength operation was quite of unexpected, where one would eventually expect a shorter single-wavelength operation obtained by a compression of the broad spectrum shown in fig 8.6. If we take a look at the low temperature fluorescence measurements of the $^4F_{3/2} \longrightarrow {}^4I_{11/2}$ transition, we can notice an asymmetric broadening of the emission around 1065 nm: this suggests the presence of two non resolved lines, as shown in fig 8.9 by the fitting with two Gaussian curves, peaked at 1065.5 nm and 1066.1 nm. This may explain the dual wavelength operation in the mode-locked regime. It is worth noticing that the laser transitions at room temperature are red-shifted, as it happens for example with Nd:YAG, whose emission peak shifts by 4 pm/°C (49).

Finally, in the three-wavelength operating regime, three pulses at 1062.2 nm, 1066.6 nm and 1067.1 nm with a duration of about 3 ps were observed, with a relatively small dispersion on the output coupler, which is an important fact thinking of possible applications via extra-cavity frequency mixing setups.

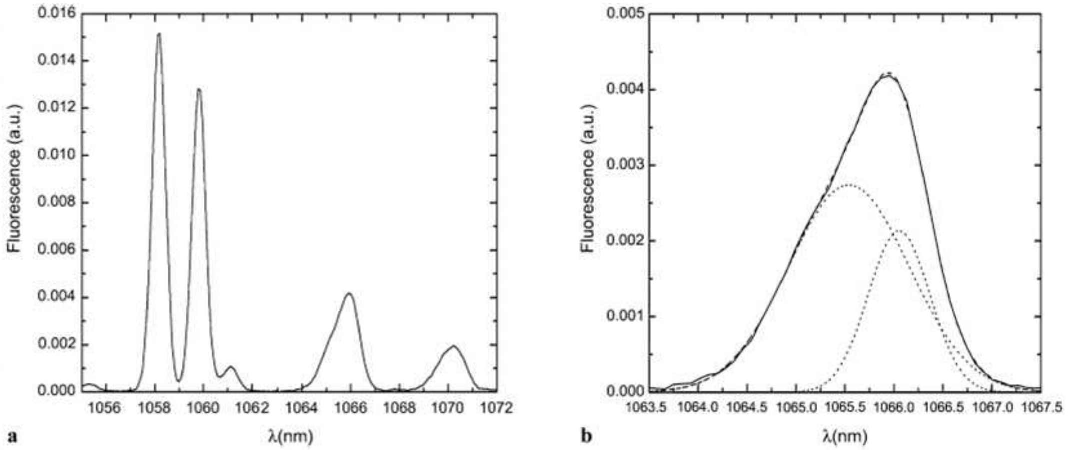

Figure 8.9: Nd:LGGG, multiple emission. - Multi-site structure of Nd: LGGG shown by the luminescence at 10 K after pumping at 807.2 nm. The emission around 1066 nm (solid line) is fitted by two Gaussian curves centered at 1065.5 nm and 1066.1 nm (dotted line). The dashed line is the sum of the two Gaussian curves.

8.3 Laser operation of Nd:GAGG

8.3.1 Continuous wave operation

The Nd:GAGG sample ([Nd] = 0.95 x 10^{20} ions/cm^3) was 3 mm long and placed into the cavity at Brewster angle in order to minimize losses. In this case the absorbed pump power was limited to 500 mW due to the relative position and bandwidth of pump and absorption lines, and the length of the crystal.

Also with this sample, efficient CW laser operation was achieved: with an output coupler of transmittivity $T_{OC} = 5\%$ the maximum output power of 256 mW with a slope efficiency of 55% was obtained. The results are summarized in fig 8.10.

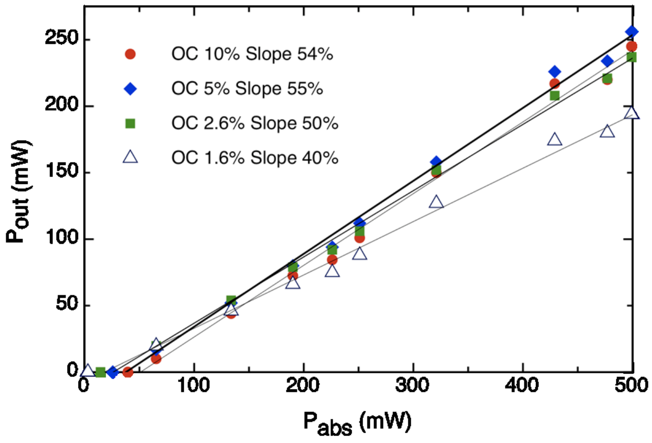

Figure 8.10: Nd:GAGG, cw laser slopes. - Performance of Nd:GAGG in cw operation, with several output couplers.

8.3.2 Mode-locking operation

As for Nd:LGGG, the shortest mode-locked pulses were observed with the 2% SAM (1.2% saturable loss) and 0.8% OC. In these conditions, stable and simultaneous mode-locking of two different wavelengths centered around 1061.4 nm and 1062.7 nm was obtained.

In fig 8.11 the spectrum of the 65 mW average power pulse train is shown. Also in this case we can considered the mode-locking spectrum as the sum of contributions from two distinct spectral features, modeled as gaussian profiles (S1 and S2). This leads to pulses as short as 5.9 ps and 3.7 ps, with the 60% of the energy carried by the shorter pulse. The calculated autocorrelation of the total intensity $I(t) = I_1(t) + I_2(t)$ yields a result in good agreement with the measured autocorrelation (fig 8.12).

It has to be considered that in principle the autocorrelation should be calculated starting from the total intensity corresponding to the sum of the pulse amplitudes: in addition to the pure intensity autocorrelation, this gives frequency-beating cross-correlation terms as well as high-frequency terms, which are displayed in fig 8.12 for comparison. This was not observed in our case. A possible explanation is that phase noise and timing jitter (≈ 1 ps) typical of passively mode-locked solid state lasers (87) average to zero such correlation contributions, leaving only the intensity term that was observed. This jitter contribution should not be of the order of the pulse width, however, since this would produce a clearly detectable pedestal in the autocorrelation spectrum. Moreover, the autocorrelation measurement was carried out with a *Femtochrome Research FR-103XL* autocorrelator that allows clean result by adjusting an integration parameter (that happens to produce an even smoother trailing edge). Furthermore many traces are usually averaged to improve the signal-to-noise ratio, probably contributing to a general wash-out of the beating fringes.

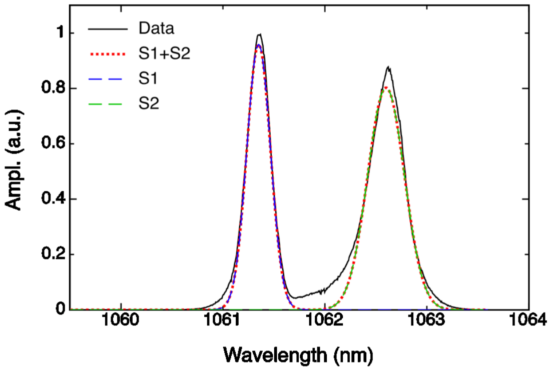

Figure 8.11: Nd:GAGG, mode-locked spectrum. - Spectrum of mode-locked laser at two wavelengths (1061.4 and 1062.7 nm). Decomposition with two gaussian lineshapes.

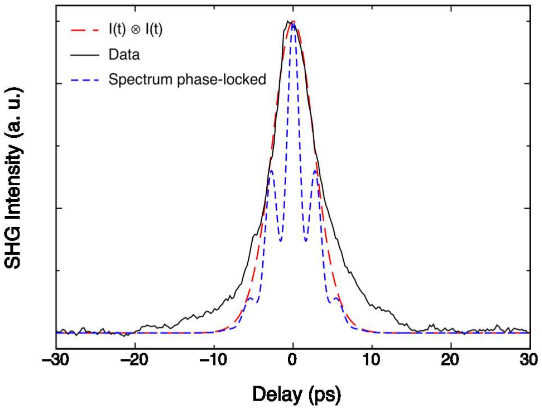

Figure 8.12: Nd:GAGG, autocorrelation spectrum. - Non-collinear second-harmonic autocorrelation in dual-wavelength regime. Also shown are: a) autocorrelation curve corresponding to the total intensity of Fourier limited pulses with spectral density S1 and S2, with $\tau = 5.9$ ps and 3.7 ps (intensity fwhm) (red dash line); b) intensity autocorrelation corresponding to the measured spectrum (Fig. 11) (no fringes, black continuous line); c) autocorrelation corresponding to the measured spectrum (fig 8.11) assumed ideally phase-locked (blue dashed line).

8.4 Summary

The results presented in this section confirm that obtaining sub-ps pulses with disordered Nd-doped materials is not as obvious as the quite broad emission spectra would suggest. What happens instead is that pulses at several different wavelengths are oscillating simultaneously in the resonator. This could lead to promising applications in the THz generation field: the average output powers presented here are still definitely too low for an efficient THz generation, but powers of a few Watts could be obtained via extracavity amplification, now possible with commercially available fibre modules. Via frequency mixing in suitable non-linear media, then, radiation in the 0.13 - 1.3 THz region could be generated.

Chapter 9

Ho : $LiYF_4$

$LiYF_4$ is an insulating, uniaxial crystal which presents the Scheelite structure. A wide transparency range, extending from the UV up to 5 μm, together with a low phonon energy ($\approx$ 550 cm^{-1}), makes it an excellent candidate for laser applications over a wide spectral range.

The symmetry group of this crystal is C^6_{4h} and the unit cell is made of four molecules, with rare earths entering the Y^{3+} site with S^4 point simmetry. The cell parameters are: a = b = 0.5160 nm, c = 1.085 nm.

In this chapter I will show the spectroscopic investigation performed on $LiYF_4$ (hereafter YLF) single crystal doped with Ho^{3+}. The sample used for spectroscopic measurements in this thesis was grown in our lab with the Czochralski method and presents a Ho^{3+} atomic concentration of 0.8 %. A review of the energy level structure of this Ho^{3+}-doped crystal can be found in literature (94).

9.1 Introduction

Ho^{3+}- doped crystals are well known emitters for laser application in the mid-infrared wavelength region, around 2 μm. This can have several application, from water absorption LIDAR to gas sensing or laser surgery. The best known pumping scheme is the in-band pumping of the $^5I_7$ level (fig. 9.1) around 1.9 μm with Tm^{3+} lasers, and subsequent emission on the long wavelength tail of the $^5I_7 \rightarrow {}^5I_8$ transition (48).

Also the codoping of Tm^{3+} and Ho^{3+} is a well studied combination, where one can have the advantage of pumping Tm^{3+} around 790 nm, obtaining laser emission at 2μm from Ho^{3+} via Tm^{3+} → Ho^{3+} energy transfer (25).

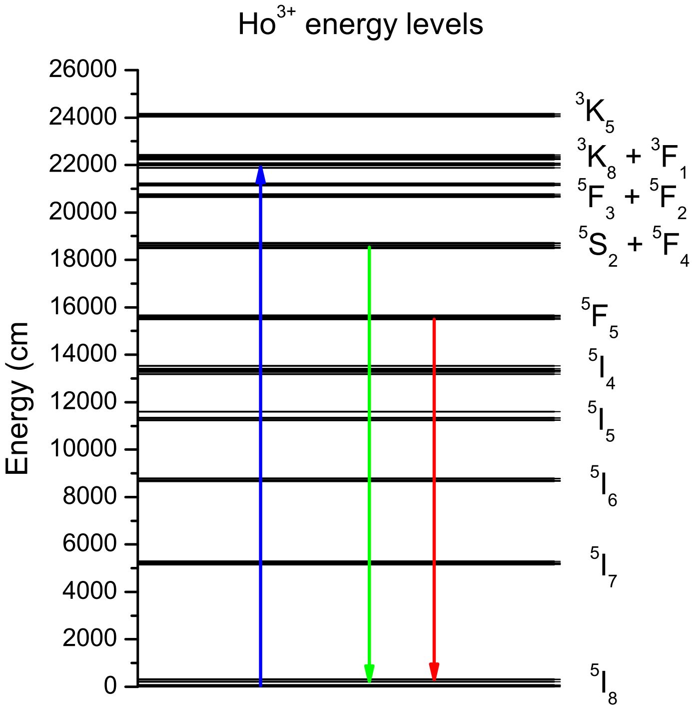

Figure 9.1: Ho^{3+}, energy levels - Energy level scheme of Ho^{3+}

In my case, I decided to focus on the visible transitions that can be observed in the single-doped system, toward the realization of all-solid-state visible laser devices. This aspect has not been investgated deeply in past years for Ho^{3+}- doped materials (although stimulated emission in the green spectral range was observed at 77 K in Ho3+:CaF_2 by Kaminskii et al in 1965 (90)), but it's becoming an interesting research field due to the recent developement of InGaN laser diodes, which allow to direct pumping of upper levels around 22500 cm^{-1}, i.e. in the blue region. The possible applications range from basic research to industrial fields such as display technology.

Taking a look to the energy level scheme of Ho^{3+} (9.1), one can notice that the $^5F_4$ + $^5S_2$ multiplet should be efficiently populated by pumping the $^3K_8$ + $^3F_1$ manifolds around 22500 cm^{-1}, and so direct emission to the ground $^5I_8$ state or to the first excited states $^5I_7$ and $^5I_6$ might be efficiently obtained. The point of how much of the population is transferred by non-radiative processes to the $^5F_4$ + $^5S_2$ multiplets seems to be an issue for the efficiency of this system: in fact these levels are separated from the upper $^3K_8$ + $^3F_1$ levels (in which the electrons are pumped) by circa 3000 cm^{-1}. Considering that the maximum phonon energy in YLF is about 550 cm^{-1}, multiphonon relaxation driven by 5 phonons is possible but other depopulation channels from the upper level have to be considered.

Also the transitions starting from the $^5F_5$ excited multiplet to the $^5I_8$ ground state are interesting, being located in the red specral region; in fact, the possibility of obtaining multiple visible emissions from the same crystal is something that has been deeply investigated for example for Pr^{3+}-doped materials (18) but not yet for Ho^{3+}.

With this purpose, I performed a study of the absorption and emission properties of this crystal, measuring the absorption and emission cross sections at room temperature and investigating the temperature dependence of the lifetime of the upper multiplets, in order to determine the radiative lifetimes.

9.2 Absorption measurements

The absorption measurements performed on the samples showed no evidence of optically active impurities, within the sensitivity of the spectrophotometer. The spectra were taken in both polarization (parallel and perpendicular to the c axis of the matrix) with

a resolution of 0.1 nm, and the absorption coefficient was then calculated.
From these spectra also the absorption cross section was calculated in the region of interest. Since the main idea exposed in this chapter is to discuss the possibility of the realization of a visible laser via pumping in the blue spectral region with GaInN diodes, in fig 9.2 I show the result of the measurement between 400 and 500 nm. Here one can notice that the main absorption line (peaked at 453 nm) is not perfectly matching the wavelength of commercially available blue diodes operating around 445 nm, and so the overall conversion efficiency will be consequently reduced due to the loss of pump energy.

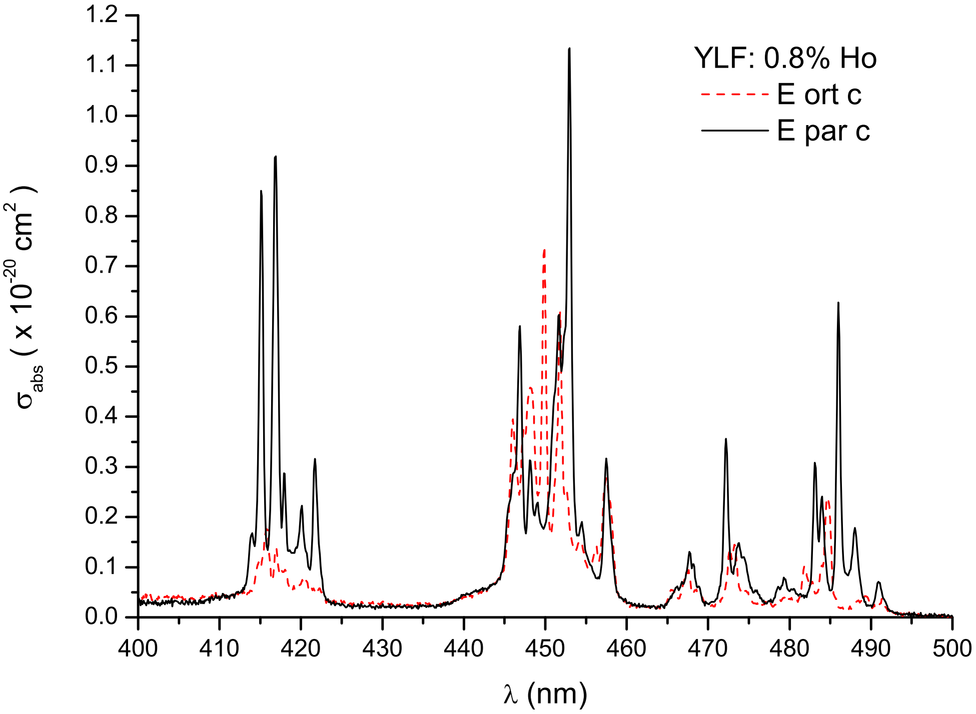

Figure 9.2: Ho:YLF, σ_{abs} - Room temperature absorption cross section of Ho^{3+} doped LiYF$_4$

9.2.1 Emision cross sections

The emission cross sections were evaluated via the reciprocity method and the partition functions were calculated according to the energy level structure given in (94). The results are plotted in fig 9.3 and 9.4 respectively for the $^5I_8 \rightarrow {}^5S_2$ and $^5I_8 \rightarrow {}^5F_5$ transitions. One can notice clearly that the cross sections are promising for both transitions, being in the order of 10^{-20} cm^2.

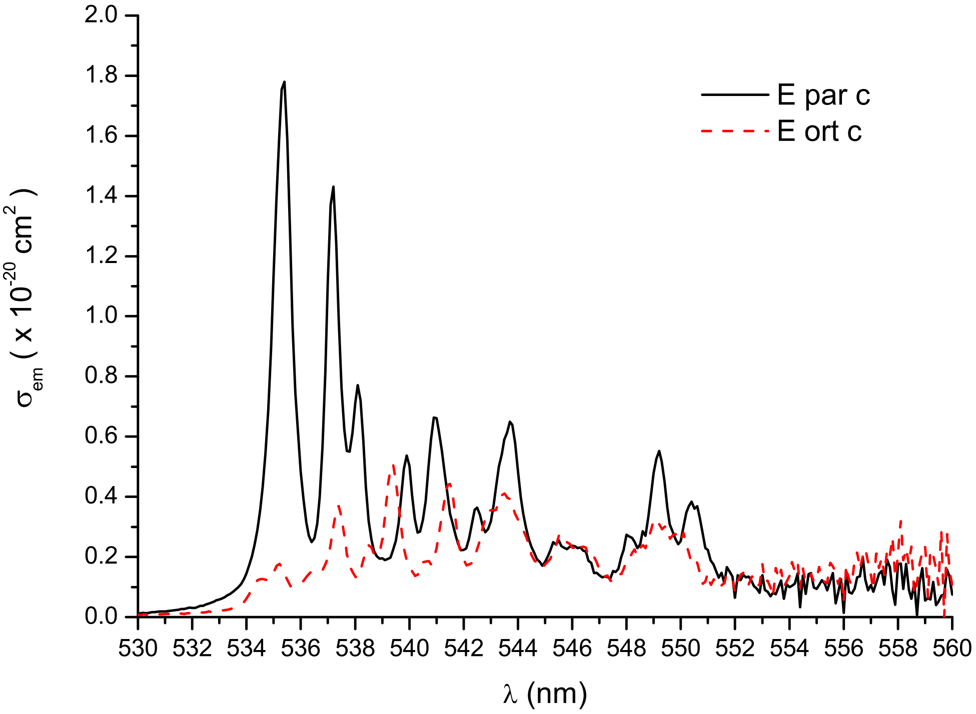

Figure 9.3: Ho:YLF, σ_{em} $^5S_2 \rightarrow {}^5I_8$. - Emission cross section calculated via the reciprocity method for the $^5S_2 \rightarrow {}^5I_8$ at room temperature in Ho^{3+} doped LiYF$_4$.

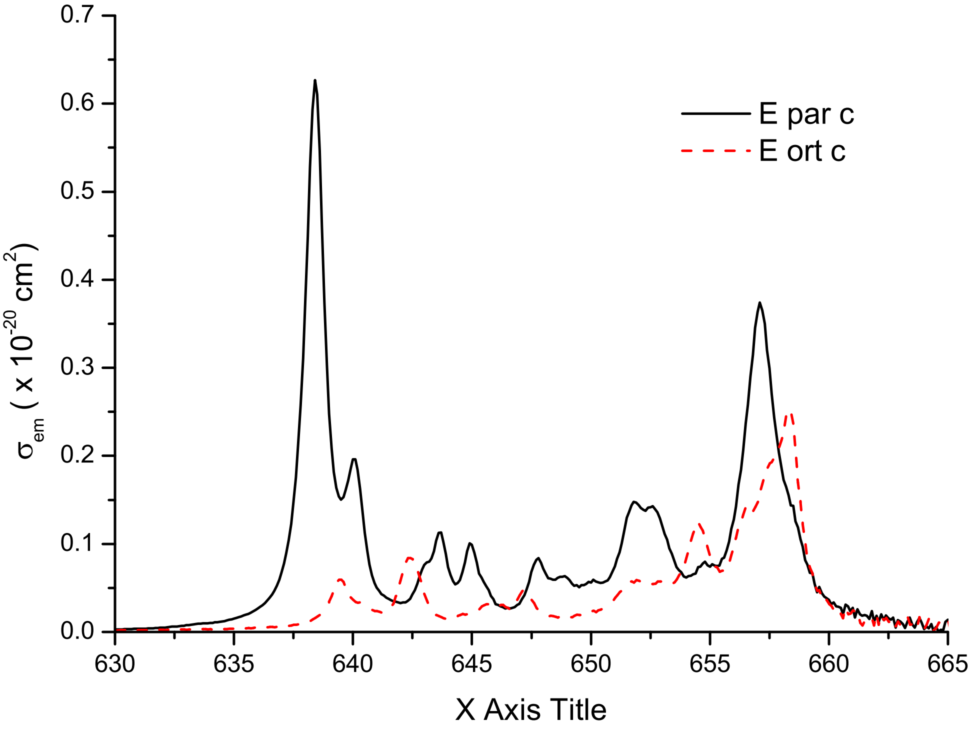

Figure 9.4: Ho:YLF, σ_{em} ^{5}F$_5$ → ^{5}I$_8$. - Emission cross section calculated via the reciprocity method for the $^5F_5 \rightarrow {}^5I_8$ at room temperature in Ho^{3+} doped LiYF$_4$.

9.3 Decay time measurements

The measurement of the decay times from the interested levels has been performed at both room temperature and low temperature, down to 10 K. The observed transitions were $^5S_2 \rightarrow {}^5I_8$ and $^5F_5 \rightarrow {}^5I_8$.

When measuring the decay from the $^5S_2$ level, one should consider all the possible processes that contribute to shorten the lifetime; non-radiative relaxations take place at higher temperature, but also cross relaxations are quite effective, due to the relatively high doping level of the sample (0.5 at%). In order to determine the radiative lifetime a less doped sample (for example 0.1 at%) should better be investigated, but unfortunately no sample with such a low doping concentration was present in our lab at the time of these measurements. Further investigations might be useful to check the importance of the cross-relaxation processes.

One more aspect that is important to consider is that the $^5S_2$ and the $^5F_4$ mainfolds are both populated when pumping the $^3F_1$ and $^3K_8$ states around 22500 cm^{-1}, and so the overall decay time is the result of the mixing of these two manifold.

Another multiplet that has been observed is the $^5F_5$, from which the $^5F_5 \rightarrow {}^5I_8$ transition around 660 nm originates. This is an other important transition to be observed in order to evaluate the possibility of the realization of an efficient laser source.

9.3.1 $^5F_4$ + $^5S_2$ manifolds

The temporal decay curve of the $^5F_4$ + $^5S_2$ manifolds was recorded as a function of temperature from 10 K to room temperature. The sample was pumped at 447 nm using the frequency doubled radiation of a pulsed Ti-Sapphire laser, taking care to reduce the incident energy to the lowest possible value in order to avoid nonlinear processes that might affect the value of the decay time introducing additional depopulation channels. The decay curves were non exponential (as shown in fig. 9.5), and the value of the decay time has been calculated via the τ-integral equation. In the logarithmic plot one can clearly notice the non-linear part of the decay curve at a short time scale, due to cross-relaxation processes, and the linear tale of the decay.

In fig 9.6 the results of the T-dependent decay measurements are plotted, showing the decrease of the lifetime with increasing temperature. The decay time at 10 K was found to be 180 μs, while at room temperature this value is reduced to 90 μs, due to phononic decays to the lower levels.

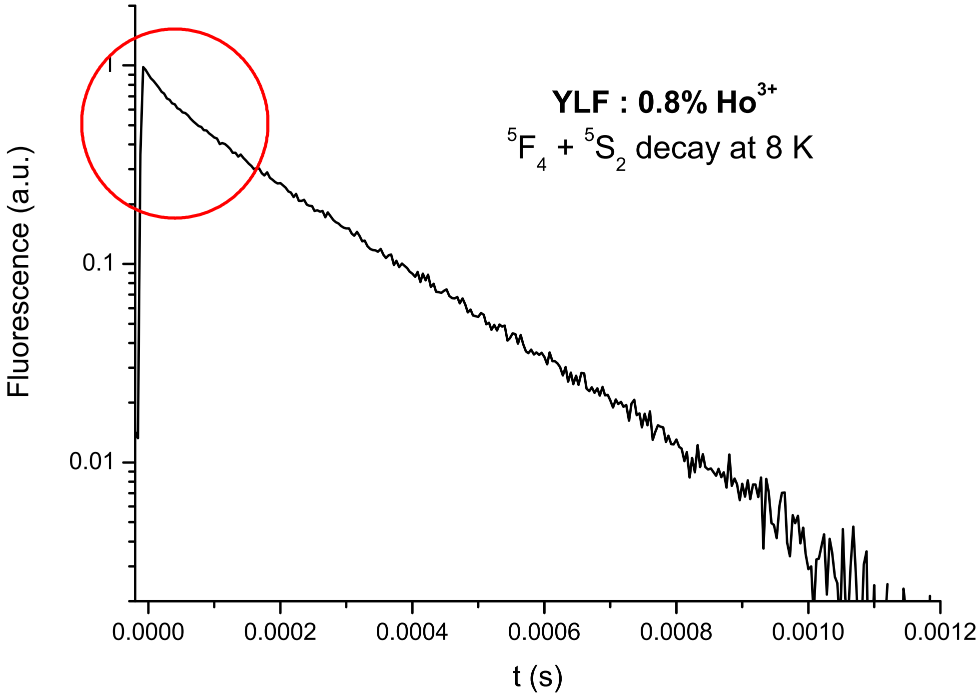

Figure 9.5: Ho:YLF, $^5F_4$ + $^5S_2$ decay, 8K - Non exponential decay curve of the $^5F_4$ + $^5S_2$ manifolds at 10 K in Ho^{3+} doped LiYF$_4$

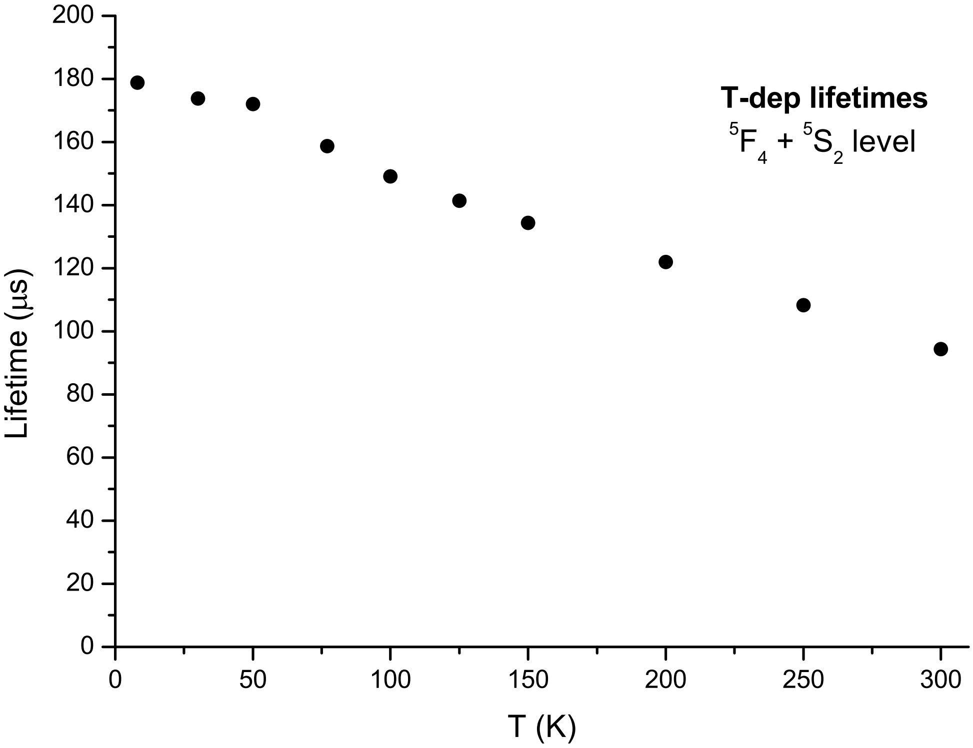

Figure 9.6: Ho:YLF, $^5F_4$ + $^5S_2$ decay, T-dep. - Temperature dependence of the decay time constant of the $^5F_4$ + $^5S_2$ manifolds from 10 K to room temperature in Ho^{3+} doped $LiYF_4$

9.3.2 ^{5}F$_5$ manifold

Also the temporal decay curves of the ^{5}F$_5$ manifold were recorded as a function of temperature from 10 K to room temperature. The decay curves observed at 658 nm also in this case were non exponential (as shown in fig. 9.7), and the value of the decay time has been calculated via the τ-integral equation. In fig 9.8 the results of the decay measurements from the ^{5}F$_5$ manifold are plotted, showing the decrease of the lifetime with increasing temperature. The measured decay time at 10 K was 210 μs, decreasing to 102 μs at room temperature.

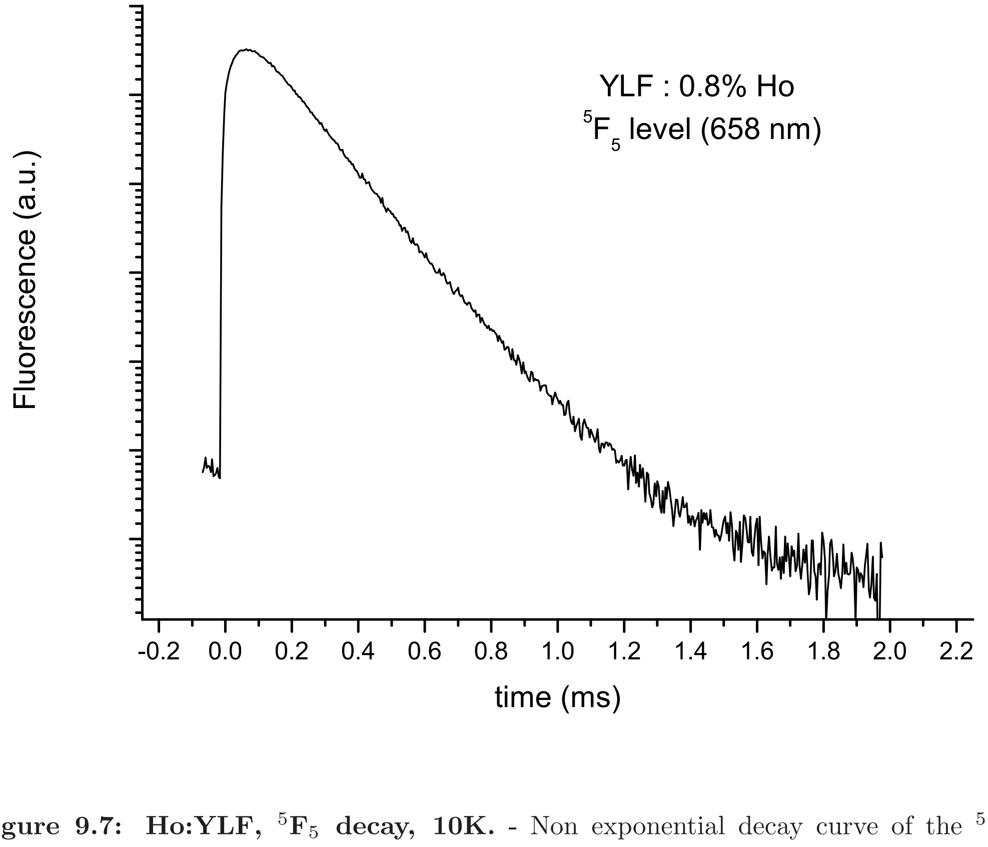

Figure 9.7: Ho:YLF, ^{5}F$_5$ decay, 10K. - Non exponential decay curve of the ^{5}F$_5$ manifolds at 10 K in Ho^{3+} doped LiYF$_4$

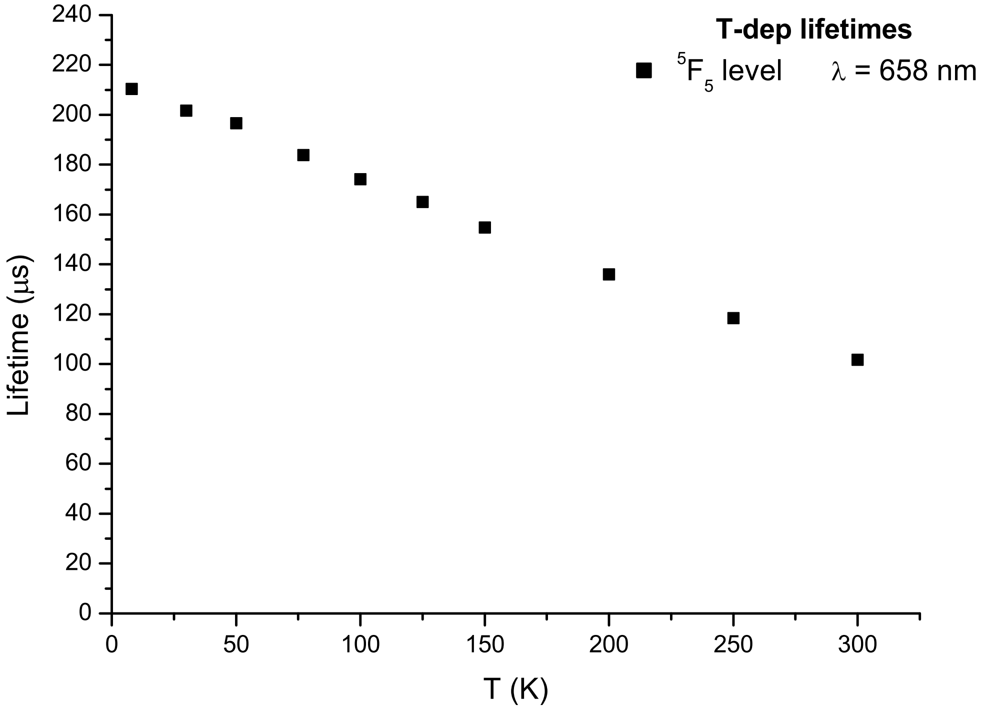

Figure 9.8: Ho:YLF, ^{5}F$_5$ decay, T-dep. - Temperature dependence of the decay time constant of the ^{5}F$_5$ manifold from 10 K to room temperature in Ho^{3+} doped LiYF$_4$

9.4 Summary

The analysis performed on the 0.8% Ho^{3+}- doped LiYF$_4$ crystal grown by Czochralski method showed that the absorption and emission characteristics, together with a reasonably high lifetime of the upper levels, might be interesting for the development of a laser system.

One of the big issues however is the reabsorption from the ground state that might increase the threshold for laser operation up to a few watts. At this level, this has to be considered just a starting point for a more detailed study and modelization of this system, but it seems that there are good potentials for a realization of a laser device with an accurate choice of the dopant concentration.

Chapter 10

Pulsed laser deposition of Tm-doped Sesquioxides

In this section the Pulsed Laser Deposition of Tm-doped sesquioxide films is reported. First, a general description of the technique is presented, and some references are indicated for more detailed explanations on the growth dynamics. Then, an overview of the materials that were used for the deposition is given. Finally, both the structural and spectroscopic analysis of the grown films is reported, showing morphological and optical properties of the samples.

The description of the experimental setup has already been given in chapter 3.

10.1 Pulsed laser deposition - general aspects

Pulsed laser deposition (PLD) is a method for the deposition of thin films, based on the ablation of a target by means of high energy UV laser radiation and subsequent balistic deposition of the ablated plume on a heated substrate. When the target is irradiated by the high energy laser beam, a plasma plume is ejected perpendicularly to the surface: the composition of this plume is complex, containing atoms, molecules, ionized material, and bigger molten particles of target material. The plume itself contributes to modify the material by means of collisions in the time of flight to the substrate. When this material reaches the substrate, depending on its temperature and on the energy of the particles in the plume, the formation of the film starts.

This technique was first demonstrated by Smith and Turner in 1965 (84), but it found an intensive development only in the 80's. Nowadays, it is a well established method for the growth of many kinds of materials, and treated on many textbooks (24)(19) and review papers (81).One of the major advantages of this technique is the possibility to obtain a stoichiometric transfer of material from the target to the substrate, thus reproducing the target composition. Moreover, PLD can be used for the deposition of materials which have a very high melting temperatures, above 2000 K, as for example sesquioxides. Also, this technique is operated in high vacuum or background controlled atmosphere, and being a non-contact growth method it is ideal to achieve high purities in the obtained samples.

Thanks to its intrinsic characteristics, this method has revealed to be effective for the growth of a wide range of materials, in particular oxides; in fact, recently waveguide laser emission has been obtained from rare earth doped oxide PLD-films (28) (29) (34) (44).

10.2 Materials

The sesquioxides are a crystal family with an anion/cation ratio of 3/2. Thanks mainly to their high thermal conductivity, relatively low phonon energies and the possibility of rare-earth doping, they attracted the attention of laser researches towards the realization of high power solid state lasers. Their main characteristics are presented in the review paper (72).

In table 10.1 some interesting properties of the sesquioxides studied in the framework of this thesis are reported.

10.2.1 Lu_2O_3

Among the sesquioxides, Lu_2O_3 has already been demonstrated to be an excellent candidate for laser operation in the 2 μm wavelength region when doped with Thulium, and efficient laser operation has been recently achieved (53). It presents a bixbyite structure, each cell containing 16 formula units (32 cations, 24 on sites with C2 point symmetry and eight with C3i point symmetry). Both sites are expected to be occupied by Thulium dopants, even though the C3i sites are apparently optically inactive.

One of the most important advantages of the $Tm : Lu_2O_3$ system is the possibility to

	Lu_2O_3	Y_2O_3	YAG	α-Al_2O_3
Crystal structure	cubic	cubic	cubic	hexagonal
Space Group	Ia3	Ia3	Ia3	$R\bar{3}c$
Cell constants (Angstrom)	10.391	10.603	12.003	a = 4.761, c = 12.996
Moss hardness	7	7	8.5	9
Thermal expansion coeff (10^{-6} K^{-1})	8.6	7.9	6.9	5.3 ($\parallel$c) 4.8 ($\perp$c)
Melting temperature (°C)	2450	2410	1930	2310
Refractive index @ 2 μm	1.90	1.87	1.80	1.73 ($\parallel$c) 1.74 ($\perp$c)
Thermal conductivity (W m^{-1} K^{-1})	13	17	11	46.6
Max. phonon energy (cm^{-1})	618	597	857	950
Ground state splitting for Tm^{3+}	835	792	610	—

Table 10.1: Properties of Lu_2O_3, Y_2O_3, YAG and Sapphire (α-Al_2O_3)

increase the doping level without reducing the thermal conductivity of the crystal: in fact, being the masses of Tm and Lu different by only 3%, the phonon propagation is not very much affected by hard doping.

During my thesis, thin films of this doped sesquioxide system (1 at%, 2 at%, 5 at% and 10 at%) were deposited on Sapphire substrates and investigated from a spectroscopical point of view, and the results are discussed in section 10.4.

10.2.2 Sapphire

Epitaxial-grade polished sapphire was used during this thesis as substrate material for the deposition of thin films. Sapphire is the α-form of undoped Al_2O_3, consisting of trigonal cells with two formula units. The choice of this material is due to its good thermo-mechanical properties, as well as its wide transparency range, which extends from 140 nm up to 6.5 μm. Moreover, thanks to its low refractive index compared to Lu_2O_3, waveguiding effect is possible for films deposited on Sapphire.

Also the main characteristics of Sapphire are summaized in table 10.1.

10.3 Tm : Lu_2O_3 deposition

10.3.1 Substrates preparation

The substrates for the depositions were epitaxial grade polished Sapphires, from *Crystech GmbH* (Berlin, Germany). The smoothness of the surface is of crucial importance for the film quality, so the substrates were annealed for 1-3 hours at 1000 °C in air before the deposition. This 'fast' annealing reduces the roughness of the substrates, giving them an atomically flat terraces surface (98).

For lattice-matched films Yttria substrates were used. These were cut out of Yttria crystals grown at ILP by Heat Exchanger Method (89) (74). Those samples were cut and polished after orientation by *Crystech GmbH*. Also in this case the annealing was crucial to obtain smooth surfaces. The deposition of lattice-matched samples, however, will not be discussed in this manuscript since only preliminary results were obtained during my work.

10.3.2 Target preparation

The targets consisted of tablets pressed and sintered at high temperature. The raw materials were high purity powders (5N or better), weighted and then pressed into tablets by means of a hydraulic press (15 Tons). The tablets were then annealed in air by means of a tubolar furnace at 1800 degrees for 80 hours, thus increasing the density of the targets by a factor of 40%. This reduces the dropplet formation during the ablation process, that is crucial for the growth of single-crystal structures. For example, the target used for the deposition of Tm - doped Lu_2O_3 had a density of 5.5 g/cm^3 before and 7.7 g/cm^3 after the annealing process.

10.3.3 Deposition parameters

The parameters for the growth of sesquioxides films that were used in this work were adjusted starting from the deep experience of the ILP group in Hamburg. Some paramenters were varied in order to increase the quality of the films, in some cases despite a reduction of the growth speed.

The main informations about the growth process are shown in table 10.2, where all the important paramenters are grouped together.

Parameter	Value
T substrate	700 ° C
Taget-substrate distance	9.75 cm
Substrate heating/cooling rate	50 ° C / min
Laser energy (per pulse)	300 mJ
Laser repetition rate	10 Hz
Total pulses number	2200000
Growth rate	2.25 pm/pulse

Table 10.2: Deposition parameters for the growth of Tm-doped Lu_2O_3 films

10.4 Film characterization

The grown films were characterized from a structural and spectroscopical point of view, to compare their properties with those of the single crystals grown by the Heat Exchanger Method. The goal was to demonstrate that the luminescence properties remain the same of the high quality bulk samples.

The characterization of the films was performed both during and after growth. The *in situ* analysis was done with a reflectometer to measure the thickness of the samples during the growth process. After the growth an Atomic Force Microscopy analysis was performed to check the smoothness of the film surfaces and to check the formation of dropplets.

The spectroscopic characterization included fluorescence analysis and time decay kinetics, from which the stimulated emission probabilities were calculated.

10.4.1 AFM analysis

The Atomic Force Microscopy analysis is a fast and non destructive technique useful to have a first information on the quality of the grown samples. In fact, the eventual presence of particulates of molten material is clearly shown in this kind of analysis, as can be seen in fig. 10.1.

The analysis was performed in the non-contact mode (sect. 3) and shows that the samples have a good surface quality, but still some particulate is present, and this is most likely the reason of the high losses measured in similar films during transmission measurements (44).

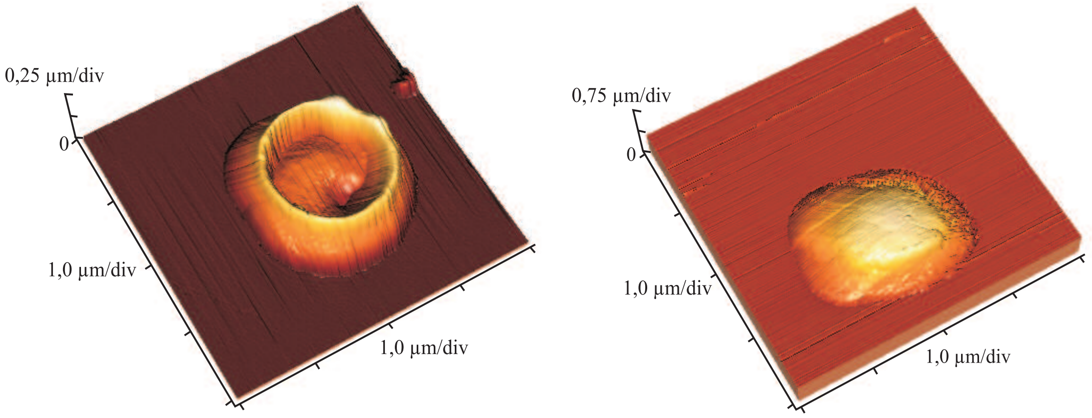

Figure 10.1: AFM image of a droplet. - AFM image of a droplet formed on Yttria film grown by PLD.

10.4.2 Fluorescence measurements

The fluorescence spectra were measured at 10 K, 77 K and room temperature under cw pumping with a laser diode operating at a central wavelength of 793 nm, taking advantage of the ($^3H_4$,$^3H_6$) $\longrightarrow$ ($^3F_4$,$^3F_4$) cross relaxation process that populates the $^3F_4$ manifold emitting around 2 μm (see fig. 10.2). The signal was detected with an InSb photodiode and the measurements were corrected for the spectral response of the experimental apparatus with a halogen lamp simulating a blackbody source at 3000 K.

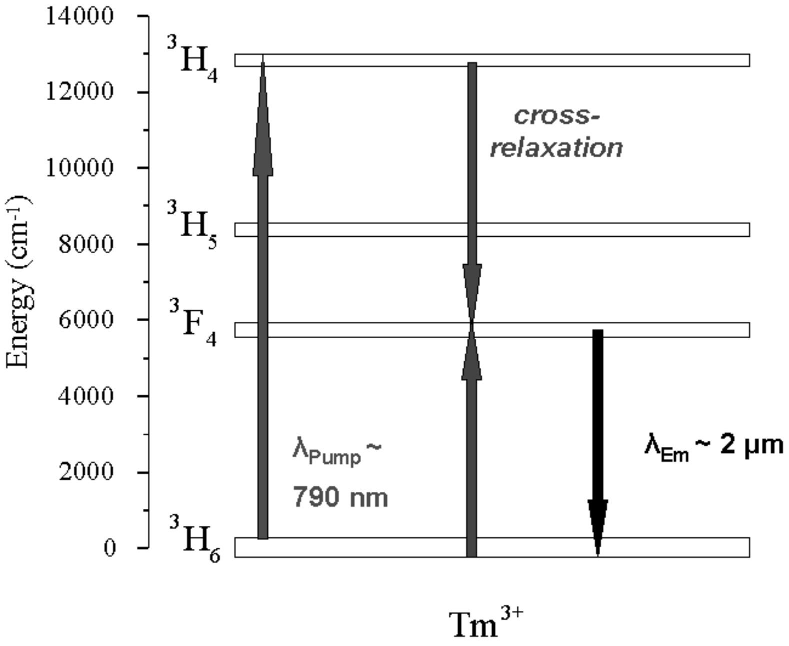

Figure 10.2: Tm^{3+} levels - Tm^{3+} energy levels scheme.

Fig 10.3 shows the measurements at the three different temperatures, normalized to the maximum of the emission. It's clearly visible that the hot bands start to blossom at 77 K and at room temperature the spectrum is very broad: this is one of the characteristics of Tm^{3+}-doped laser crystals, that allow for a broad tunability in cw operation and for a short-pulse operation in the mode-locked regime, where a broad gain band is required to compress the pulses down to the picoseconds (60) (17). Furthermore, in fig 10.4 a comparison with a bulk sample from ILP is given: one can notice that the peak position and width is mantained in the film sample, even though the relative height is slightly different in the two cases: this is most likely due to a non-perfect calibration of the measurements, which were performed in different labs with different experimental setups, and not to an intrinsic property of the samples. Also in this case, the two spectra are normalized to the maximum of the intensity.

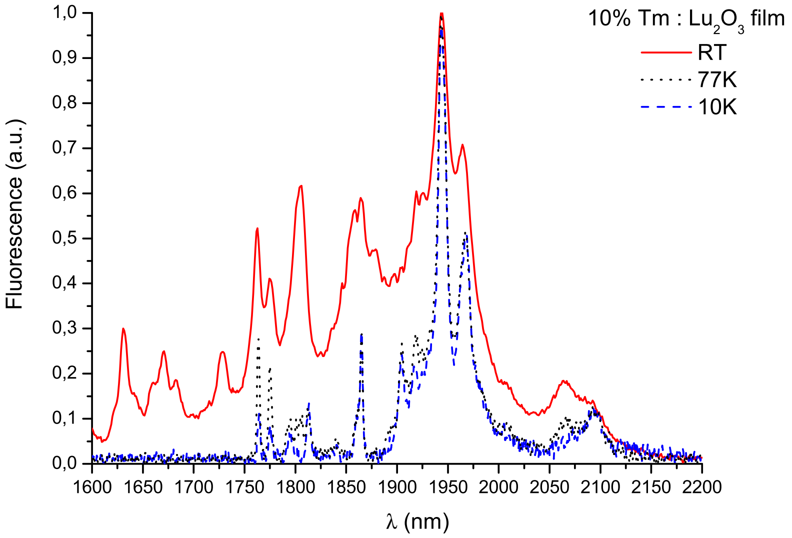

Figure 10.3: Tm:Lu_2O_3, fluorescence - Tm^{3+} : Lu_2O_3 fluorescence at 10 K, 77 K, and room temperature (RT).

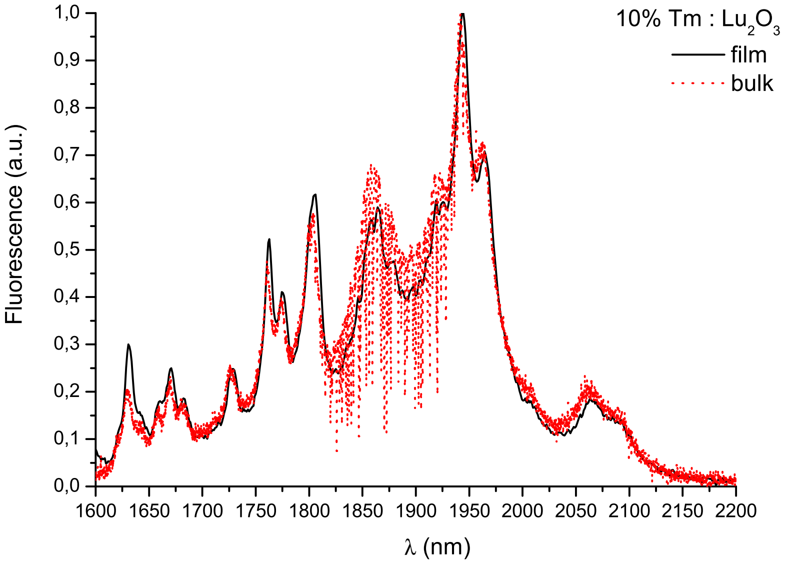

Figure 10.4: Tm:Lu$_2$O$_3$, film vs bulk - Tm^{3+} : Lu$_2$O$_3$ fluorescence spectrum at room temperature for a 10% deposited film and a 5% bulk sample from ILP laboratories.

10.4.3 Decay time kinetics

From the measurements of the lifetimes of the $^3H_4$ level one can understand the effectiveness of the $(^3H_4,^3H_6)\longrightarrow(^3F_4,^3F_4)$ cross relaxation process. In fact, increasing the Tm^{3+} concentration, this energy transfer mechanism is more efficient and the time decay of the $^3H_4$ level becomes faster, due to the fast depopulation to the $^3F_4$ manifold. Thus a study of the lifetime versus concentration is required, in order to find the optimum doping level for possible laser application. It has to be mentioned that the concentration of course also affects the lifetime of the $^3F_4$: with increasing concentration, dislocations and defects in the matrix are formed, and so energy migration to defects is increased, reducing the lifetime and hence the possibility to store energy in the upper laser level. A balance of these two effects would give the best results for laser applications.

10.4.4 $^3H_4$ manifold

In fig 10.5 one can clearly see that a strong cross relaxation takes place for samples beyond 2% doping level, when the lifetime of the upper $^3H_4$ reduces dramatically due to this effect. For the 10% sample, the value of the $^3H_4$ lifetime seems to be slightly increased with respect to the 5%: this is difficult to explain in terms of cross relaxation or energy migration, and is more likely explained with the experimental limits of the measurement itself. The fluorescence signal from the film in fact is very weak and the measurements turn out to be noisy and affected by a quite big statistic error, that can be extimated in the order of 5 μs. With this consideration, the measurements relative to the 5% and 10% samples give the same time constant, within the error.

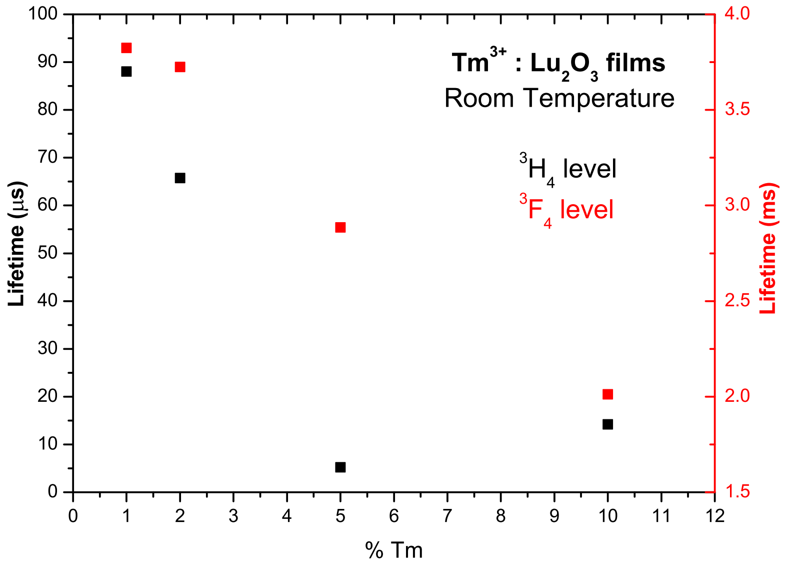

Figure 10.5: Tm:Lu$_2$O$_3$, lifetimes vs doping. - Tm^{3+} : Lu$_2$O$_3$ room temperature lifetimes versus concentration for 1%, 2%, 5% and 10% film samples. The observed manifolds are ^{3}H$_6$ and ^{3}F$_4$.

10.4.5 $^3F_4$ manifold

A detailed study of the decay kinetics from the $^3F_4$ manifold was performed. For Tm^{3+}-doped samples one doesn't expect a strong temperature dependence of the lifetime of this level: being separated by about 5000 cm^{-1} from the ground state, non-radiative transitions driven by phonons are in fact unlikely to occur. Energy migration caused by defects in the matrices are instead possible, especially for poly-crystalline films as the ones discussed here. In fig 10.6 the temperature dependence of the time decay constant at different temperatures, from 10 K to 300 K is reported. One can see that the lifetime reduces in this case from 3.3 ms to 1.6 ms increasing the temperature, and this decreasing takes place in two distinct regions: from 10 K to 100 K and from 250 K to 300 K. In the middle temperature region, from 100K to 250 K, the value of the time decay constant is nearly stable around 2 ms. This behaviour is not easy to be explained: a possible explanation is that the transitions from different Stark sublevels to the ground state have different temperature sensitizations, and the combination of these could give the global time dependence shown in fig 10.6. The lifetime of the whole manifold, in fact, is given by the combination of the emission probabilities of all the sublevels, hence the information on the single Stark-sublevel decay is lost. Also a reabsorption effect, due to temperature-dependent overlap of emission and absorption bands should be considered. A complete understanding of this would require absorption and emission measurements at the same temperatures at which the decay has been observed; the overlap of absorption and emission should be considered for each temperature and then compared to the lifetimes, but this work was not performed during this thesis.

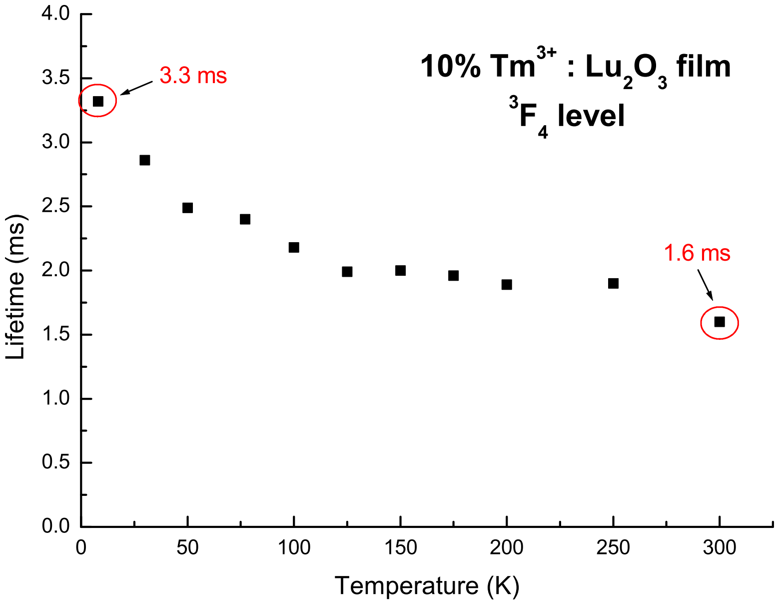

Figure 10.6: Tm:Lu_2O_3, $^3F_4$ lifetimes vs T. - Temperature dependence of the $^3F_4$ manifold time decay constant in 10% Tm^{3+} : Lu_2O_3 film sample.

10.5 Discussion of the film properties

From the performed analysis one can conclude that the deposition of Tm^{3+}-doped sesquioxide films is possible, and the properties of these films are comparable to those of bulk samples. Due to defects in the crystalline structure of the films, however, the lifetimes are reduced with respect to high quality bulk samples (53). In fact a part of the energy stored with the pump is lost via energy migration to defects and this of course reduces the lifetime of the populated manifolds. One should say, anyway, that the values of the lifetimes are still quite high and comparable to those of the earlier crystals grown at ILP in Hamburg (26), which showed laser operation. This is an important fact because this means that a laser operation of these samples might be possible, after channel waveguide writing with techniques that already revealed to be reliable, like reactive ion etching (44) or fs-laser writing (83). An example of fs-written waveguide from ILP laboratories is shown in fig. 10.7, where two parallel tracks written with fs laser pulses modify the refractive index of the propagation medium, giving it a waveguiding effect.

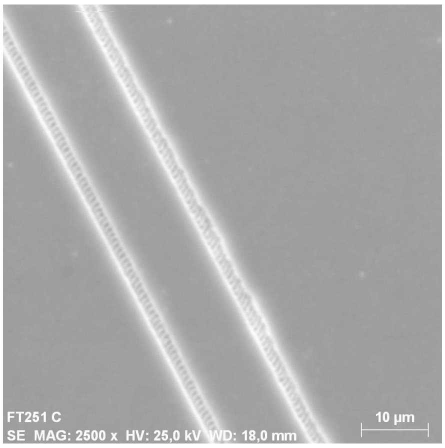

Figure 10.7: Fs-written waveguide. - Channel waveguide on YAG crystal obtained with fs-laser writing technique (top view). The waveguiding effect is due to the modification of the refractive index induced between the two clearly visible tracks (ILP laboratories, Hamburg).

Further work on finding the best deposition parameters would contribute to increase the film quality for better laser operation.
Thinking about possible practical developement of film-based laser devices, in my opinion one should focus on low-power operation, taking advanage of the typical low threshold of waveguide lasers. This might be the case for applications in the field of integrated optics, where one usually deals with low supply currents and in general low powers. Higher power operation would be much more difficult to achieve.

List of publications

- *Efficient* $Nd^{3+} \rightarrow Yb^{3+}$ *energy transfer in* $Nd^{3+},Yb^{3+}:Gd_3Ga_5O_{12}$ *multicenter garnet crystal.*
  Jia, Z; Tao, X.; Zhang, J.; Dong, C.; Jiang, M.; Arcangeli, A.; Bonelli, L.; Tonelli, M.
  Journal of Applied Physics **105**, 083113 (2009)

- *Multi-wavelength diode-pumped Nd:LGGG picosecond laser.*
  Agnesi, A.; Pirzio, F.; Reali, G. ; Arcangeli, A. ; Tonelli, M.; Jia, Z. ; Tao, X.
  Applied Physics B **99**, 135 (2010)

- *Multi-wavelength Nd:GAGG picosecond laser.*
  Agnesi, A. ; Pirzio, F.; Reali, G.; Arcangeli, A. ; Tonelli, M. ; Jia, Z. ; Tao, X.
  Optical Materials **32** 1130 (2010)

- *Spectroscopic analysis of* Nd^{3+} *doped* $(Lu_x+Gd_{1-x})_3Ga_5O_{12}$ *crystal.*
  Jia, Z.; Tao, X.; Dong, C.; Jiang, M.; Arcangeli, A.; Tonelli, M.;
  Applied Physics B **100**, 485 (2010)

- *Spectroscopic analysis of* $Nd^{3+}:Gd_3Al_xGa_{(5-x)}O_{12}$ *garnet crystal.*
  Arcangeli, A; Bigotta, S.; Tonelli, M.; Zhitai, J.; Zhang, J.; Tao, X.;
  Journal of the Optical Society of America B, **28**, 1475 (2011)

- *Continuous-wave and passively Q-switched laser of Nd:LGGG crystal at 0.93*μm*.*
  Jia, Z.; Zhang, B.; Li, Y.; Fu, X.; Arcangeli, A.; He, J.; Tao, X. and Tonelli, M.
  Laser Phys. Lett. **9**, 20 (2012)

- *Multi-wavelength picosecond laser sources.*
  Pirzio, F.; Agnesi, A. ; Reali, G. ; Arcangeli, A.; Tonelli, M.; Jia, Z. ; Tao, X.
  SPIE Newsroom, 29 March 2010
- *Multiwavelength picosecond pulse generation with diode-pumped Nd:GAGG and Nd:LGGG lasers.*
  Agnesi, A. ; Pirzio, F. ; Reali, G. ; Arcangeli, A. ; Tonelli, M. ; Jia, Z. ; Tao, X.
  Proc. SPIE, 7721, 77210d (2010)

References

[1] A. Agnesi, S. Dell'Acqua, A. Guandalini, G. Reali, F. Cornacchia, A. Toncelli, M. Toncelli, K. Shimamura, and T. Fukuda. *IEEE J. Quantum Electron.*, 37:304, 2001. 58, 71, 74

[2] A. Agnesi, S. Dell'Acqua, A. Guandalini, G. Reali, A. Toncelli, M. Tonelli, and E. Cavalli. *Appl. Phys. B*, 71:153, 2000. 29

[3] A. Agnesi, F. Pirzio, G. Reali, A. Arcangeli, M. Tonelli, Z. Jia, and X. Tao. *Applied Physics B*, 99:135, 2010. 63

[4] T. H. Allik, C. A. Morrison, J. B. Gruber, and M. R. Kokta. *Phys. Rev. B*, 41:21, 1990). 29, 74

[5] B.F. Aull and H.P. Jenssen. *IEEE J. Quantum Electron*, 18:925–930, 1982. 58, 74

[6] R. Balda, J. Fernndez, I. Iparraguirre, and M. Al-Saleh. *Opt. Mater.*, 28:1247, 2006. 41

[7] A. I. Burshtein. *Sov. Phys. JETP*, 35:882, 1972. 46

[8] U. Caldino, D. Jaque, E. Martin-Rodriguez, M. O. Ramirez, J. Garcia Sole, A. Speghini, and M. Bettinelli. *Phys. Rev. B*, 77:075121, 2008. 46

[9] U. Caldino, M. Voda, F. Jaque, J. Garca Sole, and A. A. Kaminskii. *Chem. Phys. Lett.*, 1993:84, 213. 29

[10] W. T. Carnall, P. R. Fields, and K. Rajnak. *J. Chem. Phys.*, 49:4424, 1968. 14

[11] E. Cavalli, E. Zannoni, A. Belletti, V. Carozzo, A. Toncelli, M.Tonelli, and M. Bettinelli. *Appl. Phys. B*, 68:677–681, 1999. 58

[12] E. Cavalli, E. Zannoni, A. Belletti, V. Carozzo, A. Toncelli, M. Tonelli, and M. Bettinelli. *Appl. Phys. B*, 68:677, 1999. 29, 73, 74

[13] E. Cavalli, E. Zannoni, C. Mucchino, V. Carozzo, A. Toncelli, M. Tonelli, and M. Bettinelli. *J. Opt. Soc. Am. B*, 16:1958, 1999. 66

[14] S. Chenais, F. Balembois, F. Druon, G. Lucas-Leclin, and P. Georges. *Proceedings of the Lasers and Electro-Optics Europe, Munich*, 2003:338. 44

[15] S. Chnais, F. Druon, F. Balembois, P. Georges, A. Brenier, and G. Boulon. *Opt. Mater.*, 22:99, 2003. 33, 35, 36, 41

[16] N. Coluccelli, G. Galzerano, L. Bonelli, A. Di Lieto, M. Tonelli, and P. Laporta. *Opt. Express*, 16:2922, 2008. 38

[17] N. Coluccelli, G. Galzerano, D. Gatti, A. Di Lieto, M. Tonelli, and P. Laporta. *Appl. Phys. B*, 101:75, 2010. 108

[18] F. Cornacchia, A. Di Lieto, M. Tonelli, A. Richter, E. Heumann, and G. Huber. *Opt. Express*, 16:15932–15941, 2008. 91

[19] G.K. Hubler D.B. Chrisey. *Pulsed laser deposition of thin films.* John Wiley & Sons, 1994. 102

[20] D. F. de Sousa, L. F. C. Zonetti, M. J. V. Bell, R. Lebullenger, A. C. Hernandes, and L. A. O. Nunes. *J. Appl. Phys.*, 85:2502, 1999. 43

[21] L. D. DeLoach, S. A. Payne, L. L. Chase, L. K. Smith, W. L. Kway, and W. F. Krupke. *IEEE J. Quantum Electron.*, 29:1179, 1993. 38

[22] D. L. Dexter and J. H. Schulman. *J. Chem. Phys.*, 22:1063, 1954. 15, 43

[23] G. H. Dieke. *Spectra and energy levels of rare earth ions in crystals.* John Wiley & Sons, 1968. 8

[24] R. Eason. *Pulsed laser deposition of thin films.* John Wiley & Sons, 2007. 102

[25] T.Y. Fan, G. Huber, R.L. Byer, and P. Mitzscherlich. *IEEE Journal of Quantum Electronics*, 24:924–933, 1988. 90

[26] L. Fornasiero. *Nd^{3+}-und Tm^{3+}-dotierte sesquioxides.* PhD thesis, University of Hamburg, 1999. 114

[27] T. Förster. *Z. Naturforsch. A*, 4A:321, 1949. 46

[28] C. Grivas, T. C. May-Smith, D. P. Shepherd, and R. W. Eason. *Optics Communications*, 229:355–361, 2004. 102

[29] C. Grivas, D. P. Shepherd, T. C. May-Smith, R. W. Eason, and M. Pollnau. *Optics Express*, 30:210–215, 2005. 102

[30] Y. Guyot, L.E. Bausa, E. Camarillo, J. Garcia Sole, I. Vergara, A. Monteil, and R. Moncorge. *J. Appl. Phys.*, 72:5876–5880, 1992. 52

[31] Y. Guyot, L.E. Bausa, E. Camarillo, J. Garcia Sole, I. Vergara, A. Monteil, and R. Moncorge. *J. Appl. Phys.*, 72:5876, 1992. 66

[32] Y. Guyot, H. Canibano, C. Goutaudier, A. Novoselov, A. Yoshikawa, T.Fukuda, and G. Boulon. *Opt. Mater.*, 27:1658, 2005. 33, 38, 41

[33] M. P. Hehlen, H. U. Gdel, Q. Shu, J. Rai, S. Rai, and S. C. Rand. *Phys. Rev. Lett.*, 73:1103, 1994. 33

[34] H.Kuhn, S. Heinrich, A. Kahn, K. Petermann, J.D.B. Bradley, K. Worhoff, M. Pollnau, and G. Huber. *Optics Letters*, 34:18, 2009. 102

[35] H.Okada, M. Tanaka, H. Kiriyama, Y.Nakai, Y. Ochi, A. Sugiyama, H. Daido, T. Rimura, T. Yanagitani, H. Yagi, and N. Meichin. *Opt. Lett.*, 35:3048–3050, 2010. 30

[36] G. F. Imbusch and R. Kopelman. *Optical spectroscopy of electronic centers in solids.* Springer, New York, 1981. 14

[37] D. Jaque, M. de la O Ramirez, L. Bausa, A. Speghini, M. Bettinelli, and E. Cavalli. *J. Opt. Soc. Am. B.*, 21:1203, 2004. 35

[38] D. Jaque, M. O. Ramirez, L. E. Bausa, J. Garcia Sole, E. Cavalli, A. Speghini, , and M. Bettinelli. *Phys. Rev. B*, 68:035118, 2003. 43, 46

[39] D. Jaque, J. Garcia Sole, L. Macalik, J. Hanuza, and A. Majchrowsk. *Appl. Phys. Lett.*, 86:011920, 2005. 33

[40] Z. Jia, X. Tao, C. Dong, X. Cheng, W. Zhang, F. Xu, and M. Jiang. *J. Cryst. Growth.*, 292:386, 2006. 33, 35

[41] Z. Jia, X. Tao, C. Dong, J. Zhang, and M. Jiang. *J. Synth. Cryst.*, 36:1257, 2007. 33

[42] Z. Jia, X. Tao, H. Yu, C. Dong, J. Zhang, H. Zhang, Z. Wang, and M. Jiang. *Opt. Mater.*, 31:346, 2008. 63, 64

[43] B. R. Judd. *Phys. Rev.*, 127:750–761, 1962. 14, 60, 72

[44] A. Kahn, S. Heinrich, H.Kuhn, K. Petermann, J.D.B. Bradley, K. Worhoff, M. Pollnau, and G. Huber. *Optics express*, 17:6, 2009. 102, 106, 114

[45] A. A. Kaminskii. *Laser Crystals.* Springer-Verlag, Berlin, 1981. 5, 56

[46] A. A. Kaminskii. *Crystalline lasers: physical processes and operating schemes.* CRC press, New York, 1996. 5, 60, 66, 68, 72, 73, 74

[47] A. A. Kaminskii, V. V. Osiko, S. E. Sarkisov, M. I. Timoshechkin, E. V. Zharikov, J. Bohm, P. Reiche, and D. Schultze. *Phys. Stat. Sol. (a)*, 49:305, 1978. 74

[48] J. W. Kim, J. I. Mackenzie, D. Parisi, S. Veronesi, M. Tonelli, and W. A. Clarkson. *Optics Letters*, 35:420–422, 2010. 89

[49] O. Kimmelma, I. Tittonen, and S. C. Buchter. *Appl. Opt.*, 47:4262, 2008. 84

[50] H. Kimura, H. Maeda, and M. Sato. *J. Crystal Growth*, 74:187–190, 1986. 49

[51] H. Kimura, T. Numazawa, M. Sato, and H. Maeda. *Jpn. J. Appl. Phys.*, 28:1644–1647, 1989. 49

[52] H. Kimura, T. Numazawa, M. Sato, and H. Maeda. *Jpn. J. Appl. Phys.*, 28:1654–1658, 1989. 49

[53] P. Koopmann, R. Peters, K. Petermann, and G. Huber. *Appl Phys B*, 102:19 24, 2011. 102, 114

[54] D. Kopf, G.J. Sphler, K.J. Weingarten, and U. Keller. *Appl. Opt.*, 35:912, 1996. 80

[55] W. F. Krupke. *Opt. Commun.*, 12:210, 1974. 44, 72

[56] W. F. Krupke, M. D. Shinn, J. E. Marion, J. A. Caird, and S. E. Stokowski. *J. Opt. Soc. Am. B*, 3:102, 1986. 44

[57] H. Kühn, S. T. Fredrich-Thornton, C. Kränkel, R. Peters, and K. Petermann. *Opt. Lett.*, 32:1908–1910, 2007. 23

[58] T. Kushida, H. M. Marcos, and J. E. Geusic. *Phys. Rev.*, 167:289, 1968. 37

[59] Y. Kuwano and S. Saito. *J. Crystal Growth*, 92:17–22, 1988. 58

[60] A.A. Lagatsky, S. Calvez, J. A. Gupta, V. E. Kisel, N. V. Kuleshov, C. T. A. Brown, M. D. Dawson, and W. Sibbett. *Optics Express, Vol., Issue 10, pp. (*, 19:9995–10000, 2011. 108

[61] F. Liegard, J. L. Doualan, R. Moncorge, and M. Bettinelli. *Appl. Phys. B*, 80:985, 2005. 43

[62] T. S. Lomheim and L. G. Deshazer. *Opt. Commun.*, 24:89, 1978. 72

[63] T. S. Lomheim and L. G. De Shazer. *Phys. Rev. B*, 20:4343, 1979. 44

[64] V. Lupei. *Opt. Mater.*, 19:95, 2002. 29, 66

[65] K. Maeda, N. Wada, M. Umino, M. Abe, Y. Takada, N. Nakano, and H. Kuroda. *Jpn. J. Appl. Phys., Part 2*, 23:L759, 1984. 43

[66] J. G. Manni, J. D. Hybl, D. Rand, D. J. Ripin, J. R. Ochoa, and T. Y. Fan. *IEEE Journal of Quantum Electron.*, 1:95, 2010. 33

[67] M. Marezio, J.P. Remeika, and P.D. Dernier. *Acta Cryst.*, B24:1670–1674, 1967. 30

[68] M. Marezio, J.P. Remeika, and A. Jayaraman. *J. Crystal Growth*, 45:1821–1824, 1966. 30

[69] D. E. McCumber. *Physical Review*, 136:954, 1964. 12

[70] G. Menzer. *Z. Kristallogr.*, 63:157, 1926. 46

[71] G. S. Ofelt. *J. Chem. Phys.*, 37:511–520, 1962. 14, 60, 72

[72] K. Petermann, G. Huber, L. Fornasiero, S. Kück, E. Mix, V. Peters, and S.A. Basun. *Journal of Luminescence*, 87:973 – 975, 2000. 102

[73] R. Peters, C. Kraenkel, S.T. Fredrich-Thornton, K. Beil, K. Petermann, G. Huber, O.H. Heckl, C.R.E. Baer, C.J. Saraceno, T. Suedmeyer, and U. Keller. *Appl Phys B*, 102:509514, 2011. 33

[74] R. Peters, C. Kraenkel, K. Petermann, and G. Huber. *Journal of Crystal Growth*, 310:1934 – 1938, 2008. 104

[75] V. Petit, P. Camy, J.-L. Doualan, and R. Moncorge. *Appl. Phys. Lett.*, 88:051111, 2006. 33

[76] L.A. Riseberg and W.C. Holton. *Opt. Commun.*, 9:298–299, 1973. 30

[77] A. Rodenas, D. Jaque, J. Garcia Sole, A. Speghini, M. Bettinelli, and E. Cavalli. *Phys. Rev. B.*, 74:035106, 2006. 33

[78] J. J. Romero, D. Jaque, L. E. Baus, and E. Cavalli. *J. Appl. Phys.*, 95:1774, 2004. 29

[79] M. D. Rotter and B. Dane. *Opt. Commun.*, 198:155, 2001. 74

[80] J. R. Ryan and R. Beach. *J. Opt. Soc. Am. B*, 9:1883, 1992. 37

[81] K.L. Saenger. *Processing of Advanced Materials*, 2:1 – 24, 1993. 102

[82] K. Shimamura, M. Timoshechkin, T. Sasaki, K. Hoshikawa, and T. Fukuda. *J. Cryst. Growth*, 128:1021, 1993. 29, 30

[83] J. Siebenmorgen, T., K. Petermann, and G. Huber. *Optics Express*, 18:16035–16041, 2010. 114

[84] H. M. Smith and A. F. Turner. *Appl. Opt.*, 4:147, 1965. 101

[85] N. Sugimoto, Y. Ohishi, Y. Katoh, A. Tate, M. Shimokozono, and S. Sudo. *Appl. Phys. Lett.*, 67:582, 1995. 33

[86] D. Sun, Q. Zhang, Z. Wang, J. Su, C. Gu, A. Wang, and S. Yin. *Cryst. Res. Technol.*, 40:698, 2005. 36

[87] H. Tsuchida. *Opt.Lett.*, 24:641, 1999. 86

[88] I. Vergara, A. Monteil, G. Boulon, G. Madej, and J. Garcia Sole. *Materials Chemistry and Physics*, 26:181–191, 1990. 29

[89] D. Viechnicki and F. Schmid. *Journal of Crystal Growth*, 26:162 – 164, 1974. 104

[90] Y.K Voronko, A.A. Kaminskii, V.V. Osiko, and A.M. Prokhorov. *JETP lett.*, 1:3, 1965. 91

[91] B. M. Walsh, N. P. Barnes, R. L. Hutcheson, and R. W. Equall. *Advanced Solid State Lasers OSA Trends in Optics and Photonics Series*, 34:490, 2000. 74

[92] B. M. Walsh, N. P. Barnes, R. L. Hutcheson, and R. W. Equall. *IEEE J.Quant. Elec.*, 37:1203–1209, 2001. 30

[93] B. M. Walsh, N.P. Barnes, R.L. Hutcheson, R.W. Equall, and B. Di Bartolo. *J.Opt. Soc. Am. B*, 15:2794–2801, 1998. 30

[94] B. M. Walsh, G. W. Grew, and N. P. Barnes. *J. Phys.: Condens. Matter*, 17:7643 – 7665, 2005. 89, 93

[95] B.M. Walsh, N.P. Barnes, R.L. Hutcheson, and R.W. Equall. *OSA Trends Optics and Photonics Series, Optical Society of America, Washington*, 34:490–493, 2000. 58

[96] M. J. Weber. *Phys. Rev. B*, 4:3153, 1971. 43

[97] K. Yoshida, H. Yoshida, and Y. Kato. *IEEE J. Quantum Electron.*, 24:1188–1192, 1988. 31

[98] M. Yoshimoto, T. Maeda, T. Ohnishi, H. Koinuma, O. Ishiyama, M. Shinohara, M. Kubo, R. Miura, and A. Miyamoto. *Appl. Phys. Lett.*, 67:2615, 1995. 104